EPA-600/2-77-154
August 1977

Environmental Protection Technology Series

APPLICATION OF FABRY-PEROT INTERFEROMETRY TO REMOTE SENSING OF GASEOUS POLLUTANTS

Environmental Sciences Research Laboratory
Office of Research and Development
U.S. Environmental Protection Agency
Research Triangle Park, North Carolina 27711

RESEARCH REPORTING SERIES

Research reports of the Office of Research and Development, U S Environmental Protection Agency, have been grouped into nine series. These nine broad categories were established to facilitate further development and application of environmental technology Elimination of traditional grouping was consciously planned to foster technology transfer and a maximum interface in related fields The nine series are:

1 Environmental Health Effects Research
2 Environmental Protection Technology
3 Ecological Research
4 Environmental Monitoring
5 Socioeconomic Environmental Studies
6 Scientific and Technical Assessment Reports (STAR)
7 Interagency Energy-Environment Research and Development
8 "Special" Reports
9 Miscellaneous Reports

This report has been assigned to the ECOLOGICAL RESEARCH series This series describes research on the effects of pollution on humans, plant and animal species, and materials Problems are assessed for their long- and short-term influences Investigations include formation, transport, and pathway studies to determine the fate of pollutants and their effects This work provides the technical basis for setting standards to minimize undesirable changes in living organisms in the aquatic, terrestrial, and atmospheric environments

This document is available to the public through the National Technical Information Service, Springfield, Virginia 22161.

EPA-600/2-77-154
August 1977

APPLICATION OF A FABRY-PEROT INTERFEROMETRY TO REMOTE SENSING OF POLLUTANTS GASEOUS

by

Wm. Hayden Smith and Robert A. King
Princeton University Observatory
Princeton, New Jersey 08540

Contract No. 68-02-0327
Grant No. 800805

Project Officer

William F. Herget
Emissions Measurement and Characterization Division
Environmental Sciences Research Laboratory
Research Triangle Park, North Carolina 27707

ENVIRONMENTAL SCIENCES RESEARCH LABORATORY
OFFICE OR RESEARCH AND DEVELOPMENT
U.S. ENVIRONMENTAL PROTECTION AGENCY
RESEARCH TRIANGLE PARK, NORTH CAROLINA 27711

DISCLAIMER

This report has been reviewed by the Environmental Sciences Research Laboratory, U.S. Environmental Protection Agency, and approved for publication. Approval does not signify that the contents necessarily reflect the views and policies of the U.S. Environmental Protection Agency, nor does mention of trade names or commercial products constitute endorsement or recommendation for use.

ABSTRACT

A method for the remote sensing of molecular species via the rotational Raman effect was developed. The method uses the properties of a scanning Fabry-Perot interferometer to multiplex the spectra in a manner specific for a given species. Furthermore, the method allows the "in principle" sensitivity of remote pollutants to be increased by as much as 10^4 over the vibrational Raman effect. To achieve this goal, a scheme was developed for the rejection of the Raman spectra of the abundant background gases, N_2 and O_2. This was accomplished efficiently and with little loss of the Raman scattered light from the pollutant species. Laboratory measurements were conducted to demonstrate the method for a few specific cases; results were encouraging. In addition to the light rejection scheme actually used, a radically new technique utilizing the polarization properties of the Raman scattered light was also developed.

This report is submitted in fulfillment of Grant Number R-800805 and Contract Number 68-02-0327 by Princeton University under the sponsorship of the Environmental Protection Agency. Laboratory work was completed as of March 15, 1975.

CONTENTS

FIGURES

TABLES

SECTION 1

INTRODUCTION

1.1 Early Interferometry

In approaching spectroscopic instrumentation, the historical choice and concommitant agony has been that of the trade-off between resolution and throughput. Traditionally this has been viewed from the single line stance with subsequent thought being directed to criteria for the resolution of quasi-monochromatic lines and to single line or band transmission functions. Indeed, simultaneous transmission of several lines served only to confuse the interpretation of the spectrum and was considered a handicap rather than a useful effect. This parochial view was quite evident with regards the Fabry-Perot interferometer whose multiple order transmission function necessitated the use of 'order sorters' or blocking filters to remove radiation falling to either side of the order of interest, with the problem becoming especially acute at higher resolving powers and with grating spectrometers often used as prefilters because of their tunability. In their paper of 1897, Fabry and Perot[1] value their new instrument as useful in the determination of the spacing between two parallel surfaces, giving only brief mention to its value as a spectroscopic tool.

Additional, and perhaps more severe, problems plagued early Fabry-Perot interferometers. The high absorption silver coatings and poor surface figure of the etalons limited the transmission, resolution, and contrast of the instrument, while mechanical and thermal instabilities limited the patience of the experimenter. Grating spectrometers, although lacking the throughput of the Fabry-Perot, were generally reliable and displaced interferometric methods.

1.2 Current Interferometry

Advances in optics, including low-loss dielectric coatings, etalons with surface figures to $\lambda/200$ over a two-inch aperture, piezoelectric translators, and electronic temperature controllers eliminated many of the difficulties associated with earlier Fabry-Perot interferometers. Accompanying these technical advances were new conceptual techniques. In the infrared the Michelson interferometer was multiplexed as a Fourier transform spectrometer giving improved signal-to-noise ratios, while more recently, Barrett and Meyers[2] demonstrated in the laboratory that the Fabry-Perot interferometer could multiplex rotational Raman lines from linear molecules without the disadvantage of having to perform an inverse Fourier transform to extract the useful data in this case, the rotational constants of the molecule under study.

Used in the multiplexed mode, the Fabry-Perot interferometer passes simultaneously several spectral lines in which the observer is interested without transmitting the unwanted radiation which falls between the lines.

With its already high throughput and entendue enhanced by mutiplexing, the Fabry-Perot interferometer becomes a sensitive detector for a restricted class of applications where the spectra involved are periodic or near periodic in wavenumber. One of these, proposed recently by Smith,[3] is a method for the remote detection of gaseous atmospheric pollutants using laser excited backscattered rotational Raman light from the molecule of interest.

1.3 Multiplexed Fabry-Perot Interferometers

The following work will show, using mixtures of carbon dioxide in air, that the single passed Fabry-Perot interferometer is generally incapable of discriminating the minority component scattering from a gas mixture in those concentrations typical for atmospheric pollutants because of coincidences between the comb of the Fabry-Perot interferometer which has been set for a particular pollutant molecule, and certain rotational Raman lines of N_2 or another high concentration background gas that may be present. The degree of contamination will go roughly proportional to

$$\frac{1-R}{1+R}$$

where R is the reflectivity of the Fabry-Perot etalons and cannot be made arbitrarily small by increasing the reflectivity towards unity, because the accompanying loss of signal would require prohibitively long integration times.

Section IV will examine the complex interferogram produced by the atmospheric pollutant NO when multiplexed through the Fabry-Perot interferometer and demonstrate that the normal 4B and 2B resonances are not the optimum ones to be utilized when searching for the rotational Raman scattering from NO because of the blurring of the features of the interferogram by contamination from other rotational Raman lines of the NO molecule not in resonance with the comb of the Fabry-Perot interferometer. It will be shown that instead, an 8B/3 resonance should be used to sharpen the Raman peaks produced in the transmitted interferogram, thus forming a feature which is more visible than those at the 2B resonance due to higher photon count rates and a clearly defined position. This chapter will also examine how the rotational constants of the molecule under observation affect the width of the transmitted interferogram resonance and how data on NO implies that resonances with B values differing by 0.05 cm^{-1} (with B average 1.7 cm^{-1}) and contaminated by background scattering from $\Delta J = \pm 2$ $\pi_{1/2}$ and $\pi_{3/2}$ transitions can be distinguished if the approximate form of the resonance is known beforehand. Nitric oxide is a difficult case because of its doublet ground state. Other molecules not suffering the background resulting from the effects of this split state have observable hot bands at temperatures sufficiently high to give them significant populations.[4]

The results of this work give impetus to the study of multiplexed Fabry-Perot interferometers in the remote sampling of atmospheric pollutants, but the laboratory study of a two component gas system does not simulate field conditions closely enough to yet define

whether or not the remote sampling of NO (or another pollutant) is possible by this method. Certainly, the severe background contamination from N_2 and O_2 rotational Raman scattering and from Rayleigh scattering can be removed, and presumably those molecules with concentrations on the order of the pollutant to be detected will be attenuated by the mismatch of the periodicities of their spectra with the comb of the Fabry-Perot interferometer. How other background sources will affect the level of detection is not clear and remains to be demonstrated for particular situations in the field. A view of remote sampling techniques not including the multiplexed Fabry-Perot interferometer is given in the work by Kildal.[5]

In addition to use in the problem of pollution detection, the rejection techniques should prove useful in the analysis of spectra having - close lying B values (such as hot bands) and perhaps also in flame spectra where there are contaminating influences. Chapter 6 presents a different approach to the rejection of periodic spectra and background Raman scattering with the use of a crystal polarization filter. This may prove a more efficient and easily handled field technique than that of the rejection Fabry-Perot interferometer.

Apart from the remote sensing problem, a search was made using the multiplexed Fabry-Perot interferometer and the rejection inteferometer for the pure rotational Raman scattering from methane. Although this process is forbidden to first order because of symmetry, the zero point energy of the vibrational modes distorts this symmetry giving rise to a small pure rotational Raman scattering cross-section.

The Raman scattering was not observed, and the results show that the differential cross-section for Raman scattering with the scattered and incident polarizations parallel must be a factor 4×10^{-6} down from methane Rayleigh scattering for the same geometry, i.e.,

$$\sigma_{Ram}\,(\theta = 0) < 4 \times 10^{-6}\, \sigma_{Ray}\,(\theta = 0) \quad .$$

References

1. C. Fabry and A. Perot, Ann. Chim. et Phys. 12, 459 (1897).

2. J. J. Barrett and S. A. Meyers, J.O.S.A. 61, 1246 (1971).

3. W. H. Smith, Opto-electronics 4, 161 (1972).

4. J. J. Barrett and A. B. Harvey, J.O.S.A. 65, 392 (1975).

5. H. Kildal and R. L. Byer, Proc. IEEE 59, 1644 (1971).

SECTION 2

THE FABRY-PEROT INTERFEROMETER

2.1 An Introduction to the Fabry-Perot

In 1897, Fabry and Perot[1] developed an interferometer consisting of two plane parallel partially silvered mirrors with separation t. Monochromatic light incident upon their instrument is multiply reflected (figure 2.1) by the coatings and in interfering with itself gives rise to a transmitted intensity dependent upon the plate spacing, the reflectivity of the plates, and the incident wave-vector's angle to the mirror's normal. Born and Wolfe[2] show this to be the Airy Function A (x), where

$$A(x) = \frac{I_o T^2}{1+R^2-2R\cos\Phi} \qquad (2.1)$$

$\Phi = 4\pi\mu t \cos\theta$

θ = the angle of incidence

k = incident wavenumber

μ = index of refraction of the medium between the etalons

R = reflection coefficient

T = transmission coefficient

L = absorption coefficient = 1-R-T

I_0 = incident light intensity

This function is periodic with transmission maxima occuring when the phase satisfies

$$\Phi = 4\pi\mu kt \cos \theta = 2\pi n \qquad (2.2)$$

and transmission minima when

$$\Phi = 4\pi\mu kt \cos \theta = 2\pi(n+1/2) \qquad (2.3)$$

where n is an integer giving the order of the interferometer.

If the phase be changed by altering the plate separation, a series of fringes will be generated (figure 2.2) whose period is one half of the incident wavelength. Similarily for a fixed plate spacing, non-collimated light transmitted by the Fabry-Perot will form a series of circular fringes when brought into focus with a lens (figure 2.1) as the phase has an angular dependence through cos θ and the angle of incidence. Fringes represent successive orders of the interferometer, akin to orders of a spectrometer. It follows that light collimated within the spectral bandwidth of the interferometer gives a uniform illumination to the plates.

The Airy function description of the Fabry-Perot interferometer was developed assuming the ideal situation of mirrors with infinite extent, no absorption losses, perfect surface figure, and in parallel alignment. Fabry and Perot had some difficulty in approaching these ideals, but recent technical advances noted in the introduction have radically improved this situation. Deviations from predictions based on a simplified use of the Airy equation remain critical in certain applications which will be discussed in later chapters as the situation warrants.

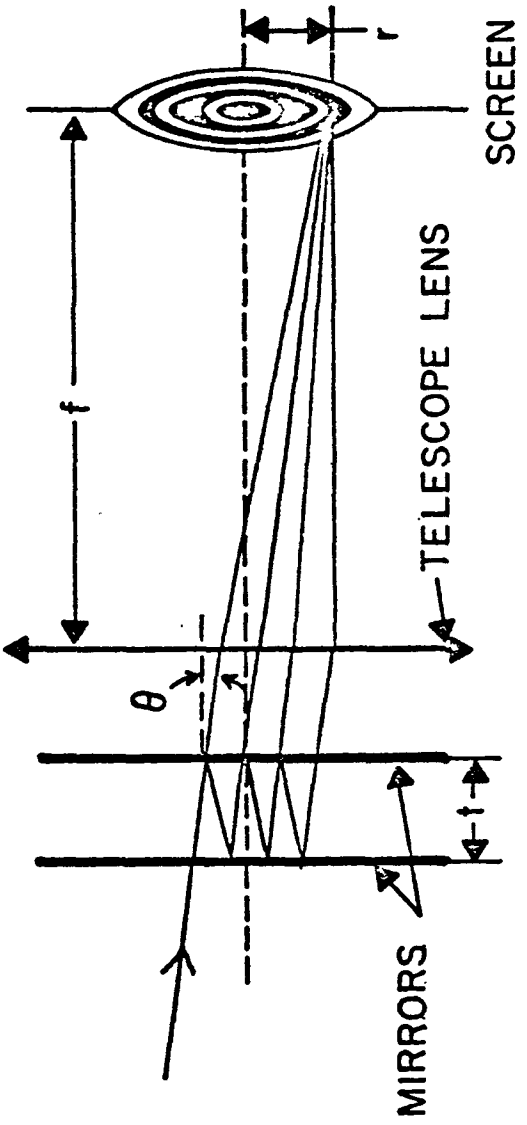

Figure 2.1. Fabry-Perot interferometer, ray tracing.

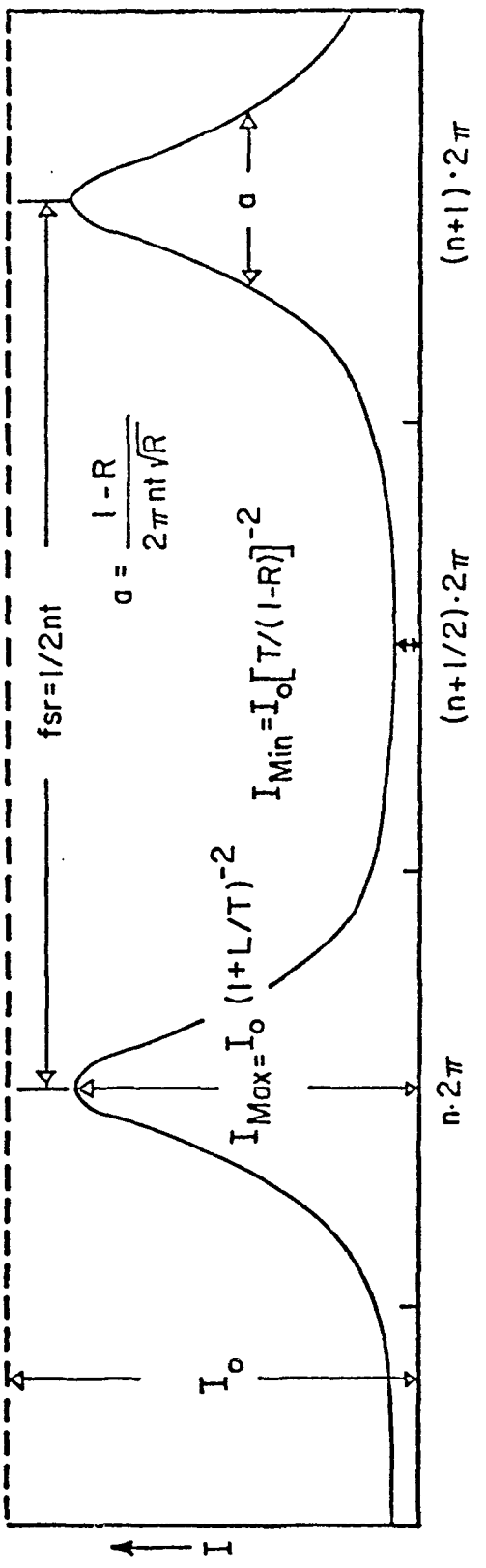

Figure 2.2 The Airy function.

2.2 Bandpass, Transmission, and Lineshapes

As noted in the introduction, a compromise must be made between resolution and throughput. A brief discussion is therefore given as to how parameters relating to the above problem were determined for the interferometer experiments.

Figure 2.3 illustrates one common experimental configuration for the Fabry-Perot, with a radiation source of small but finite extent, an input collimating lens L1, the Fabry-Perot, an out put lens L2, and an output pinhole which in this example is the limiting aperture of the system. If the pinhole subtends the angle 2α from the lens L2, then the wavenumber equivalent bandpass of this aperture is

$$\gamma_p = 1/2\ ka^2 cm^{-1}$$

$$K = 1/\lambda\ cm^{-1} \tag{2.4}$$

The transmission through the system of an arbitrary spectrum J (k) will be the convolution of this spectrum with the Airy function A (k) for the interferometer and the rectangular aperture profile given above.

$$T = A*P*J \tag{2.5}$$

The line-shape of A*P is close to Lorentzian because:

(a) the Airy function can be considered as the convolution of a Dirac comb with a Lorentzian profile and thus for finesses commonly used an individual order is nearly Lorentzian.

(b) the high count rates allowed a small pinhole with correspondingly small half width in comparison to that of the Fabry-Perot. (Typically a pinhole of radius 150 microns was used with a lens of focal length 15 cm. Applying equation 2.4

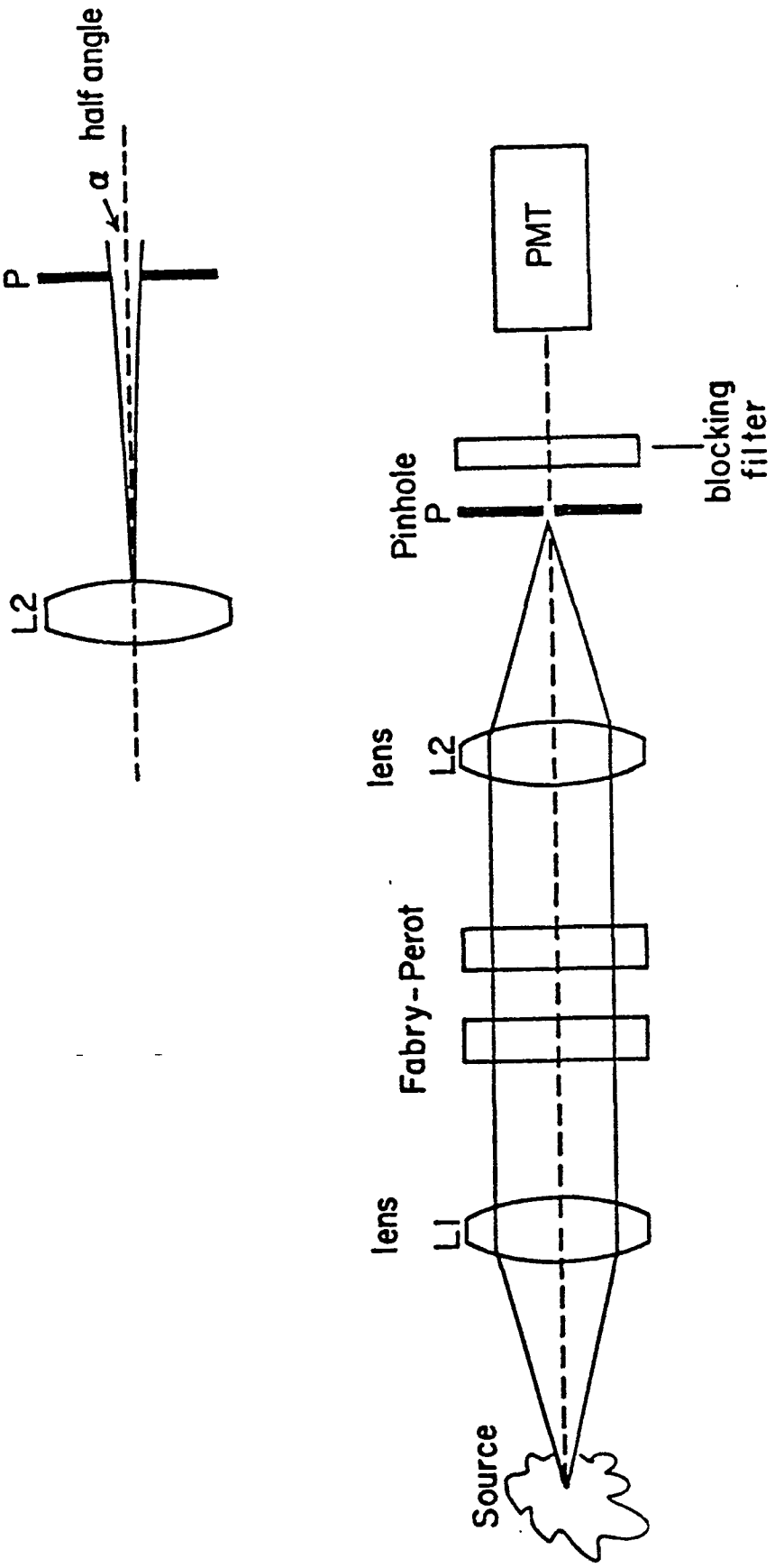

Figure 2.3. Single passed Fabry-Perot interferometer.

gives γ_p = 0.01 cm^{-1} for $\lambda \sim 5000$ Å, while γ_a was typically 0.2 cm^{-1} .)

γ_a = Airy half width

γ_p = Pinhole half width

γ_j = Spectrum half width

The resultant half width of A*P is

$$\left(\gamma_a^2 + \gamma_p^2\right)^{1/2} \tag{2.6}$$

The spectrum J (k) consists of rotational Raman lines whose shapes is dominated by the line shape of the laser used to provide the scattering photon flux. The laser profile was far from the Gaussian profile expected and had a width twice that of the norm for this type of Argon ion laser. Consequently the spectrum J (k) did not have a simple mathematical form. Chabbal[3] has calculated the half widths produced by the convolution of several functions including Gaussians with Lorentzians so that a crude estimate of the expected line width could be made in spite of the pathological shape of the laser line. Experimental measurements of the widths of J and A*P will be given in the following chapters.

Hirschberg and Wouters[4] show that the maximum transmission for a single line incident upon the Fabry-Perot can be written as

$$\frac{\varepsilon \pi I_o}{2tf\gamma} \quad (f \equiv \text{finesse}) \tag{2.7}$$

where ε is an overlap factor between .3 and .5 depending upon the exact form of the convolution integral, and γ is the line width generated by J*A.

2.3 The Practical Fabry-Perot Interferometer

Critical components of the Burleigh Fabry-Perot interferometer used in these experiments were constructed of invar to minimize thermal effects. These components included the etalon mounting rings as well as the spacers and differential screw assemblies. In addition, components were paired one against the other so that the net motion of the etalon spacing was differential as the temperature varied.

Fine adjustment of the etalons was provided by differential screws having a resolution of 10^{-3} inches per revolution, and final alignment was performed using piezoelectric translators. The PZT's (three spaced at intervals of 120° about the etalons) could be adjusted independently to align the mirrors and then with a common control moved simultaneously to scan the Fabry-Perot. The PZT's were provided with slope trims to compensate for varying rates of expansion with applied voltage. The maximum range of a PZT scan was 20-25 orders of 5145 Å light for the 10 micron stacks and approximately 3 orders for the 1 micron stacks.

A graph of applied voltage versus PZT expansion is shown in figure 2.4 for the 10 micron elements, with fiducial markings being provided by the 5145 Å Argon laser line. Although highly nonlinear when viewed over the entire range, a scan was reproducible provided that 2-3 minutes were allowed at the beginning of each expansion for the elements to relax after the rapid drop back from full extension. In addition, since fiducial markings were provided by the laser line, it was necessary to be concerned with nolinearity only within the range of a single order. The apparent change in spacing between successive orders near the center of the scan did not amount to more than 4%.

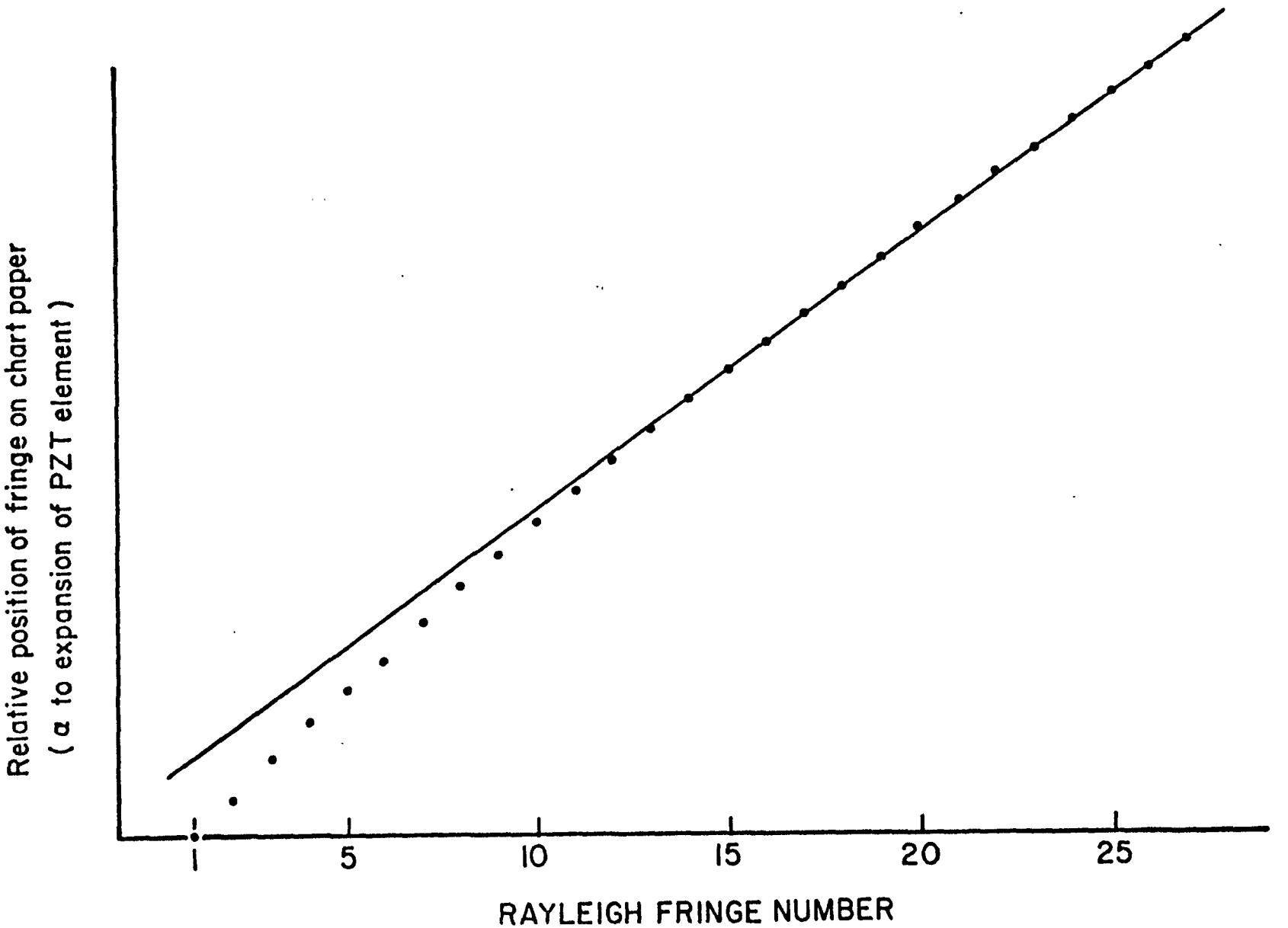

Figure 2.4. Scan of the 10 micron PZT stacks.

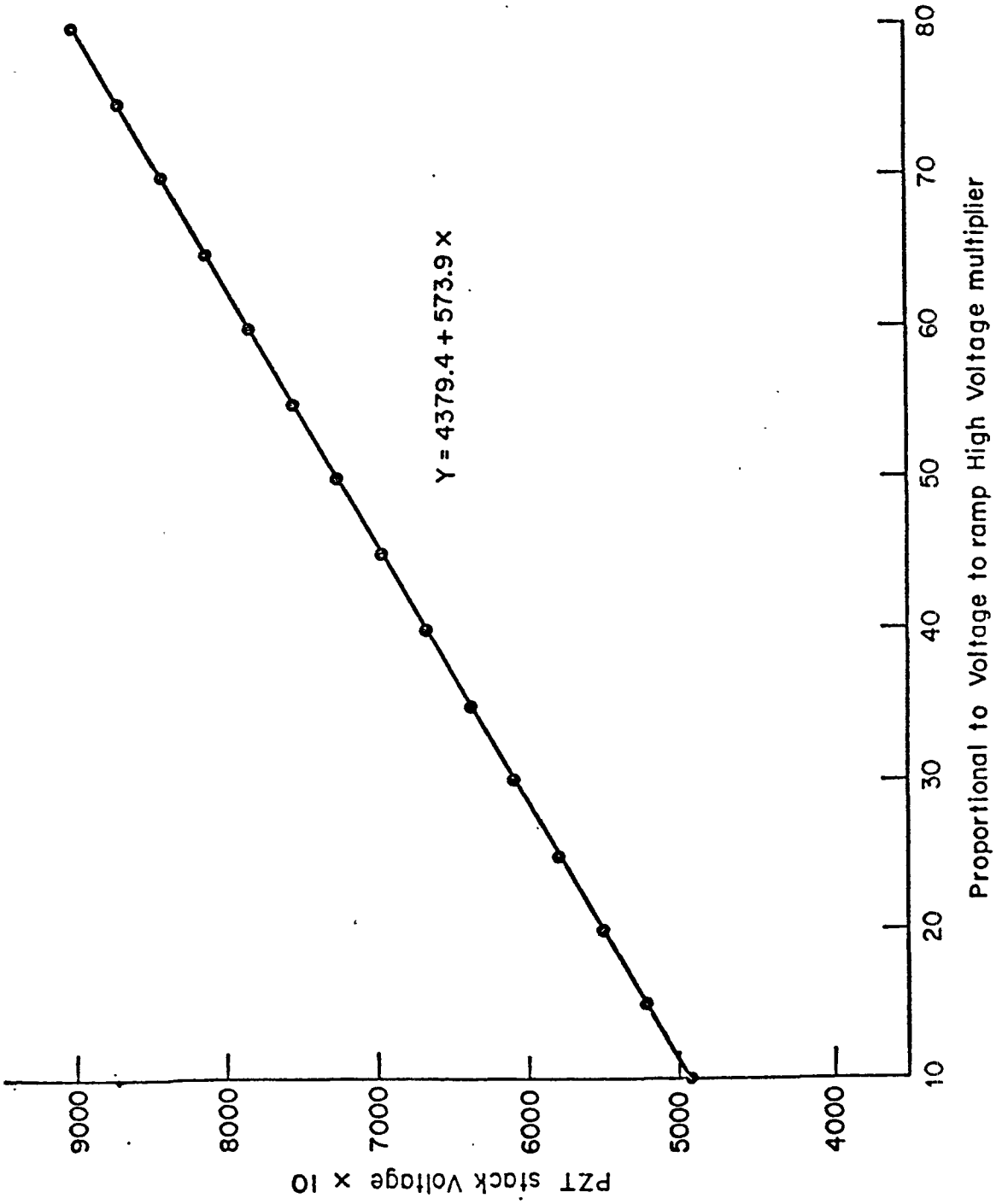

Figure 2.5. Linearity of the high voltage amplifier.

To see what fraction of the nonlinearity originated in the high voltage amplifier that drove the PZT's, a plot of the voltage applied to the PZT elements against the input ramp voltage to the amplifier was made. The graph is given in figure 2.5. Coefficients a_1 and a_0 determined from a least squares fit to a straight line are

$$a_0 = 4379.42 \pm 5.9 \text{ Volts}$$

$$a_1 = 573.91 \pm 1.2 \text{ Volts}$$

where the voltage to the PZT's = $(a_0 + a_1 n)/10$, and n is a number proportional to the input amplifier voltage. (The errors reflect the 95% confidence level). The maximum deviation from linear is less than 0.2% and the conclusion is that the nonlinearity in the scan of figure 2.4 is due to the PZT elements themselves.

The ceramic material from which the PZT elements were fabricated was additionally the source of most of the thermal drift in the interferometer. For work involving short sampling intervals, the temperature scanning was quite negligible with the electronics stepping through an order in 2-5 minutes while the Fabry-Perot would typically drift one order in 10-15 hours. For very long scans of 200-300 orders, fiducial markings provided by the Rayleigh scattered laser light from the gas sample proved a reliable method to account for absolute plate spacings. At any particular time, it was possible to give the absolute etalon separation to within 100 Å and better, depending upon the the finesse and resolution used, and in spite of temperature drifts and nonlinear effects.

2.4 Fabry-Perot Etalons and Coatings

The etalons used were 2 inches in diameter with surface figures of $\lambda/200$ in the visible. The surfaces facing away from the Fabry-Perot cavity were

wedged by 30 minutes of arc and antireflection coated to eliminate the effects of first surface contribution to scattered light into the photomultiplier tube. The etalons were mounted into invar rings by the manufacturer which were then set into the interferometer proper using nylon screws. The mounting procedure used was such as to not degrade the surface figure of the etalons whose r.m.s. deviation (for a matched pair) was on the order of 25 Å. The grinding process for the etalons resulted in a spherical defect (again less than 25 Å) which could be seen by illuminating the Fabry-Perot with collimated light. Any strains introduced in mounting the etalons were visible as a breakdown of this symmetry in the intensity of the transmitted light.

Multilayer dielectric coatings were used on the etalons with specifications given in the materials appendix. These coatings are discussed in detail in reference 2.5 and will not be mentioned further other than to note that they are low loss (absorption coefficient $\sim$ 0.05%) with low scatter and good surface figure. Soft coatings were used and care was required because they are hygroscopic to a slight degree and also sensitive to abrasion. No substantial deterioration was noted; however, over the period of a year.

References

1. C. Fabry and A. Perot, Ann. Chim. et Phys. 12, 459 (1897).

2. M. Born and E. Wolf, Principles of Optics (Pergamon Press, New York, 1959), p. 323-329.

3. R. Chabbal, Revue d'Optique 37, 49,336,501,608 (1958); R. Chabbal, J. des Rech. du C.N.R.S. 24, 138 (Paris, France, 1953).

4. J. G. Hirschberg and A. Wouters, MIAPHOOP-68.10 (Dept. of Physics, Univ. of Miami).

5. H. A. MacLeod, Thin Film Optical Filters (American-Elsevier Pub. Co., Inc., New York, 1969).

SECTION 3

THE EXPERIMENTAL CONFIGURATIONS

3.1 Introduction

A schematic view of a single passed Fabry-Perot is given in figure 3.1. A gas cell containing the mixture to be studied was placed at the intra-cavity focus of an Argon ion laser operating with approximately 40 watts of circulating power in the 5145 Å or 4880 Å line. An f/3 lens looking along the direction of the incident laser polarization to minimize Rayleigh scattered light (rottational Raman is completely depolarized with $p_{Ram} = 3/4$) collected the scattered radiation, collimated it, and directed it through the Fabry-Perot interferometer. The light transmitted by the interferometer was focused by an output lens onto a pinhole and from there to the photomultiplier tube. Photon counting techniques were used with maximum counting rates for Raman light being on the order of 100 kHz.

Details of the apparatus will now be discussed along with the gas purification system and the plate spacing determination procedure. When applicable, test data or calibration results will be presented.

3.2 Control Electronics

A drawing of the Fabry-Perot controller and data recording system is shown in figure 3.2 along with the associated waveform that it generates to drive the PZT elements. The control logic[1] has the flexibility of variable step size for the PZT's (ΔV), data integration time (τ), and upper and lower

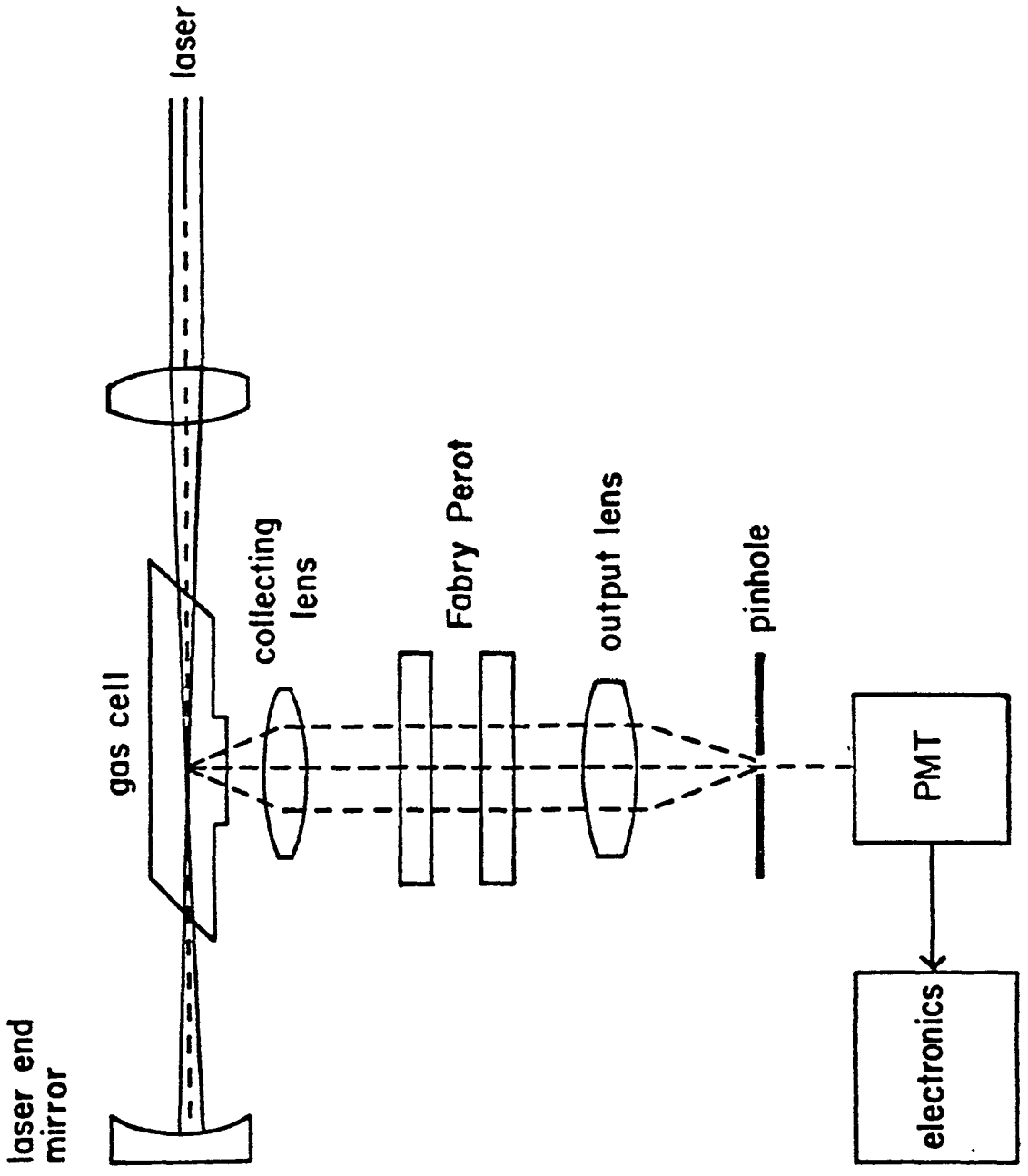

Figure 3.1. Overview of the apparatus.

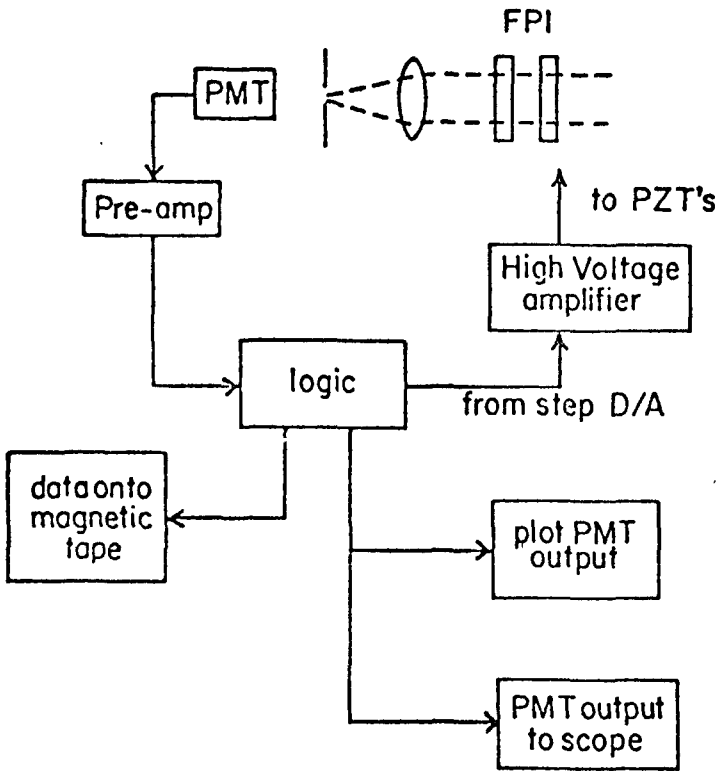

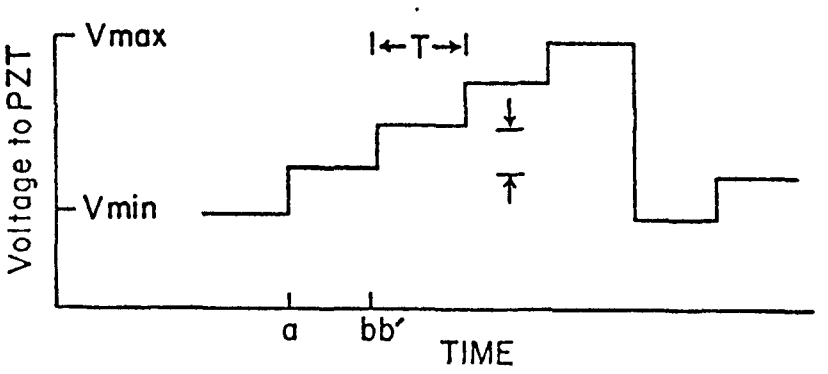

a: Change voltage to PZT's by ΔV

a – b: Take data for a time T

b: Write on scope, plotter, and mag. tape

b': Change voltage to PZT's by ΔV

Figure 3.2. Electronics.

limits V_{max} and V_{min} to the voltage on the driving stacks. The output voltage from the D/A in the controller was multiplied by a factor 100 with a high voltage amplifier and was used to drive the PZT elements in common to scan the interferometer.

Having stepped the Fabry-Perot with a voltage increment Δv, the logic would enable the gate from the PMT preamplifier to the digital counting circuits where photon counting was performed. After a time τ, the gate was disabled, and the information from the scalar along with a number proportional to the voltage on the PZT stacks was written onto magnetic tape. The process was repeated until the upper limit of the ramp was reached at which time the cycle repeated or terminated depending upon the settings on the controller.

As well as writing onto magnetic tape, the controller could simultaneously plot the data on a chart recorder with a digitally stepped x-axis, or could display it on an oscilloscope. This latter function (with τ set to 0.01 sec.) and the ramp set to scan over one free spectral range was useful for dynamic alignment of the Fabry-Perot interferometer since the effects of altering the various parameters of the system became visible in real time in terms of an alteration in the finesse of the Fabry-Perot fringes being displayed. With dynamic alignment, it was also possible to count fringes moving by on the oscilloscope screen as the fine differential screws were adjusted by hand. In this fashion, by piecing together a number of 10-20 order scans done by the PZT elements with each successive scan beginning where the former finished (the difference being set by turning the fine adjustment screws), it was possible to scan over a few hundred orders without losing track of the absolute plate separation.

The pre-amplifier cable from the PMT was kept as short as possible to minimize transmission problems with the low level PMT pulses. The pre-amplifier[2] had a rectangular wave-form with a full width of 250 nanoseconds, and count rates being less than 200 kHz avoided any saturation problems.

3.3 The Photomultiplier Tube

A Centronic bialkali photomultiplier tube was used because of its high sensitivity and extremely low dark current. When count rate was plotted versus PMT voltage for a white light source of constant illumination, a plateau was reached in the neighborhood of 1.2 KV. This is the region of greatest stability. Operation at lower voltage gave abnormally low count rates for low incident light intensities in comparison to normally expected count rates at higher light levels. This had the effect of making the Fabry-Perot fringes appear to have a much higher contrast than would normally be expected. An explanation is that the weaker pulses in the pulse height distribution from the PMT were not being sufficiently amplified by the low gain of the tube to reach the threshold set by the discriminator on the pre-amplifier. Lowering the discriminator setting had the effect of sending the pre-amplifier into oscillation, and consequently the tube and discriminator were not operated in this low voltage region.

Plotting the PMT voltage as a function of the ratio ε, defined by

$$\varepsilon = \sigma/\sqrt{N}$$

where

σ = experimentally determined standard deviation for N

N = the number of photons/sec. counted by the system for a given PMT voltage.

yielded statistics approaching what would be considered normal fluxuations at

those voltages (1.2 KV) corresponding to the plateau discussed in the above paragraph. Higher or lower voltages give increasingly poor statistics. Fluxuations or drift in the intensity of the source account for ϵ not approaching unity, with ϵ_{min} being on the order of 1.1-1.2.

Figure 3.3 gives a plot of the number of dark counts per second (sample time was 50 seconds) against discriminator setting on the pre-amplifier. At settings greater than 2 (gain equal to $\sim 3 \times 10^6$), there is an extremely slow decrease in count rate with increased level of discrimination, and with the PMT shut off, this rate drops to zero. It was unlikely that any of these counts were generated in the PMT dynode string as cleaning in an ultrasonic bath removed any residue which might have contributed to leakage current and noise pulses. The cathode was held at ground to avoid envelope generated noise in the anode grounded situation,[3] and the tube was kept in its housing at all times to prevent exposure to room light and the resulting higher dark count rates. Characteristics of the tube can be found in the materials index.

The above considerations give the optimum operating voltage for the tube as 1.1-1.2 kV with the discriminator set to two. The PMT dark count rate under these circumstances was approximately 6 per second.

3.4 The Laser

An Argon ion laser was modified so as to run in the intra-cavity mode (figure 3.4). To this end, the output coupling mirror was removed and replaced with a dielectric mirror M1, of reflectivity 99.99% at 4880 Å and a radius of curvature equal to 25 cm. A lens L1, of focal length 12 cm, was placed between this mirror and the plasma tube such that its focal point fell approximately at the center of curvature of the mirror M1. Laser resonator

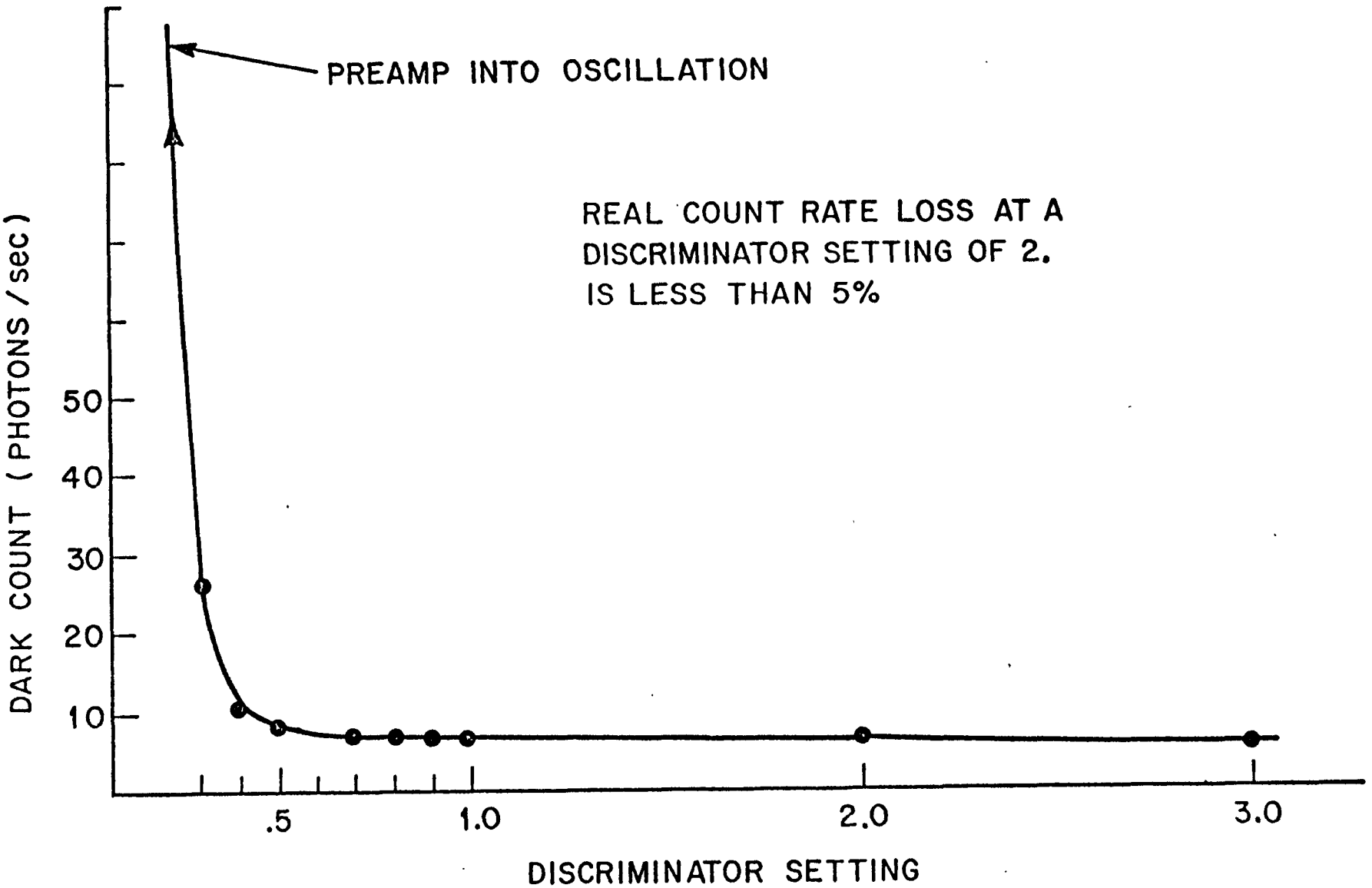

Figure 3.3. Photomultiplier tube dark count rate.

theory [4,5] gives that this configuration will be stable and that the diameter of the beam at any point in the cavity can be found from:

$$\omega_o^2 = \omega^2\left[1 + \left(\frac{\pi\omega^2}{\lambda R}\right)^2\right]^{-1} \tag{3.1}$$

$$1/2b = \frac{\sqrt{d(R_1-d)(R_2-d)(R_1+R_2-d)}}{|R_1+R_2-2d|} \tag{3.2}$$

$$1/2b = \pi\omega_o^2/\lambda \tag{3.3}$$

where

R_1 is the radius of curvature of mirror M1 (25 cm)

R_2 is twice the focal length of the lens (2x12 cm)

d is the separation between the lens and the mirror ($\sim$37 cm)

W_0 is the radius of the beam at its waist

W is the radius of the beam at a distance R from the waist.

The parameters given above for this experiment yield a beam waist of 130 microns and a beam diameter at the mirror M1 of .3 mm.

The circulating power in the cavity was estimated by using the fact that with the 5% output coupling mirror in place; the laser gave 2 watts of power at 5145 Å and at 4880 Å. This implies that power levels in the cavity will be on the order of 40 watts, assuming that losses with the extended cavity do not exceed 5%. The losses due to the lens are minimized by having it ground from laser quality material (low loss, low scatter, and good surface figure) and then having anti-reflection coatings with R less than .25% deposited on the surfaces. In addition, a single element lens rather than a cemented

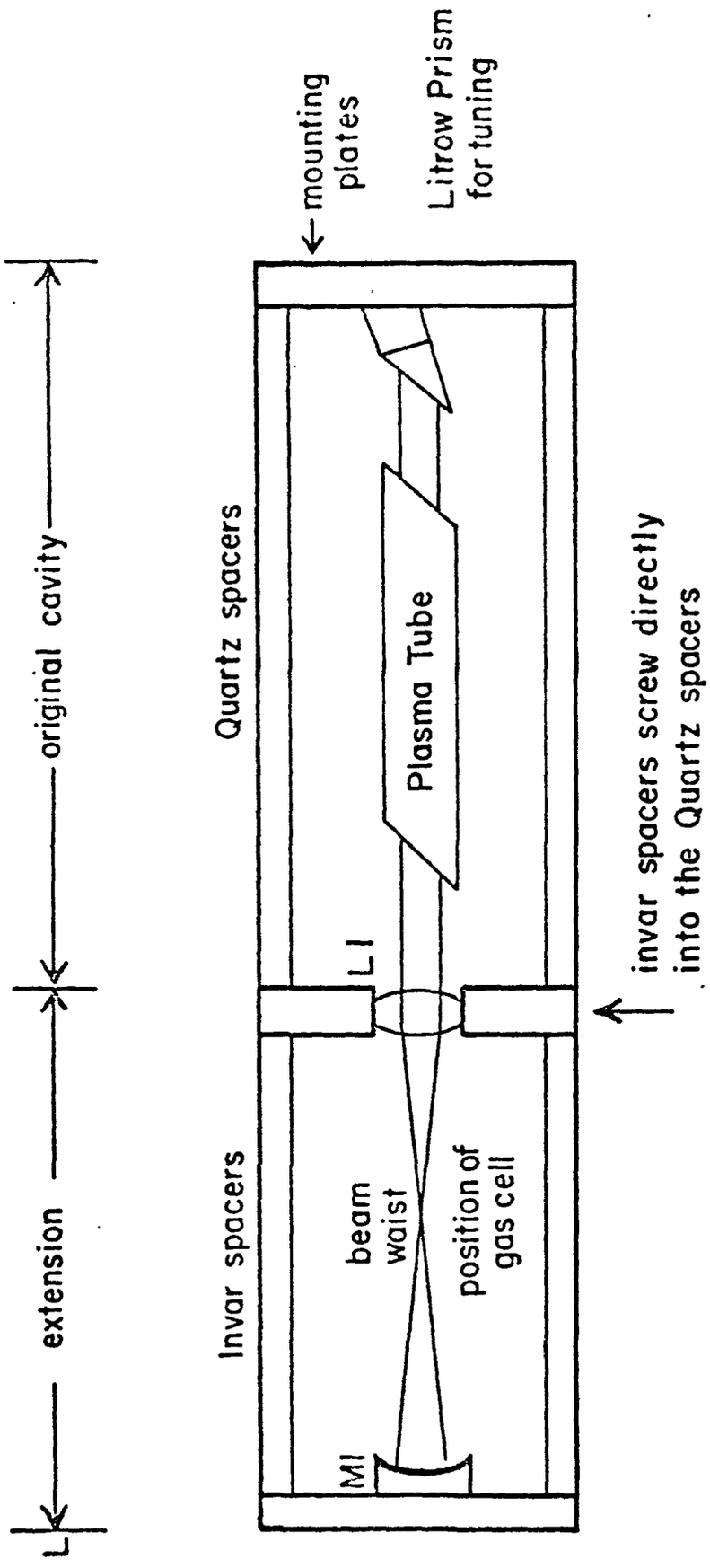

Figure 3.4. Laser cavity extension.

achromat was used to avoid absorption in the bonding material with the change in focus with different laser lines compensated for by an adjustment of the Fabry-Perot input lens on an x-y translation stage. The cavity was so stable as to lase over a wide range of positions for the lens L1.

The losses at the gas cell inserted into the cavity at the position of the beam waist were minimized by using entrance ports of laser quality material set at Brewster's angle to the incident radiation. For small angular variations about Brewster's angle, the reflection coefficient varies by less than 0.1 percent (for $\Delta\theta \sim 3^{\circ}$) and as a consequence, slight misalignments of the cell were not critical. Because the windows were at Brewster's angle, they did not have the effect of single-moding the laser.

The only other losses in the cavity were the end mirror with R =0.9999 as stated previously, and scattering and absorption from dust and gas in the path of the beam. When dust became a problem, the system could be enclosed in a plexiglass cover.

It's not unreasonable to assume therefore that the losses in the cavity were less than 4-5% and circulating powers of 30-40 watts likely.

The lens L1 was adjustable along the length of the cavity so that its focus could be made approximately coincident with the center of curvature of the mirror, while the mirror itself was mounted in an orientation stage to provide angular alignment. The cavity could be tuned by rotating either mirror M1 or else the Littrow prism, and was stable at the wavelengths listed in table 3.1 listed below.

Table 3.1. LASER LINES AND LINE STRENGTHS

Wavelength (Å)	Relative Power Levels
5145.319	4.0
5017.160	0.5
4965.073	1.2
4879.860	3.2
4764.862	1.0
4579.346	0.3

The wavelengths were taken from sources 3.6 and 3.7 and the power levels from the Spectra Physics handbook. As scattering has a ν^4 dependence and the PMT is more sensitive in the blue, the 4880 Å line was used in preference over the 5145 Å line.

The laser linewidth was measured using a Coherent Radiation spectrum analyzer with the beam profile (in wave-numbers) shown in figure 3.5 and its full width at half maximum being 0.25 cm^{-1}. Since the light used to perform this measurement was scattered from an etalon inserted into the cavity at Brewster's angle, line was not narrowed due to single-moding effects.

The broad line width of the laser used for these experiments caused severe problems in some measurements. These will be discussed in later chapters.

3.5 The Gas Cell

The gas cell is diagrammed in figure 3.6. Brewster's angle windows minimized light loss through reflection and were given a non-parallel orientation relative to one another so that the net spatial displacement of the beam in traversing the cell would be zero. The Wood's horn arrangement effectively trapped back-scattered light by dissipating its energy in successive reflections from the blackened interior. The baffling on the input and output arms for the laser eliminated light scattered from the Brewster angle windows on the gas cell and on the plasma tube, and also glow from the laser cathode and plasma discharge that was not confined to the beam axis. The set of baffles on the viewing window removed scattered and diffracted light from the baffles on the arms. All windows were of laser quality so as not to distort the wave-fronts, and in addition had low scratch and dig specifications to minimize scattering. A final extension or baffle covered the distance from the viewing port to the Fabry-Perot collecting lens to shield the system from outside radiation.

The gas cell was filled through a Hoke valve with a Swagelok coupling that mated either a 1/4" diameter glass tube from the vacuum distillation system or a 1/4" diameter piece of stainless steel tubing when samples were taken directly from the gas bottle without distillation. (The gas sample was in either case pre-filtered with a millipore filter to remove particulate matter that might contribute to Mie scattering). Figure 3.7 shows the gas fill system for the case of direct filling from the bottle. Pressures were measured using a Bourdon guage in which the gas is not exposed to face plates or other contaminating surfaces. The guage could be read to 0.5 Torr of pressure.

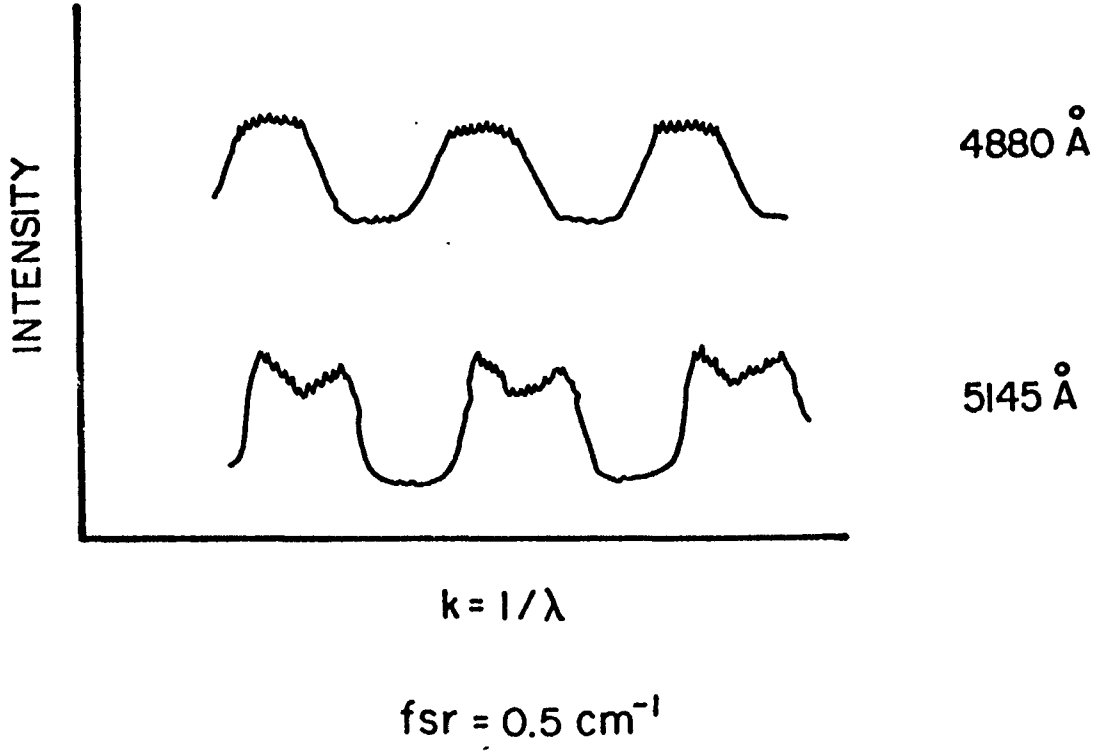

Figure 3.5. Laser line profiles.

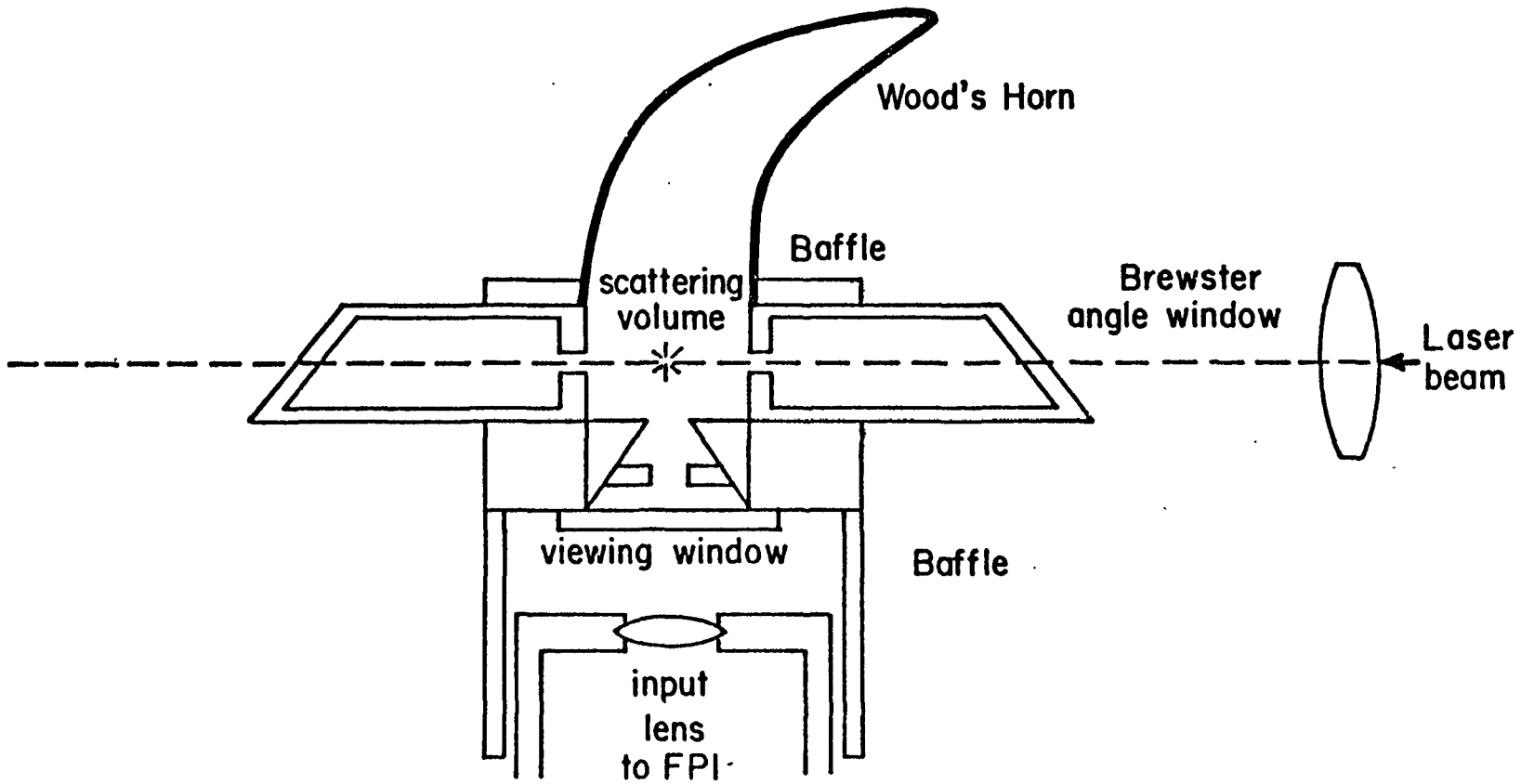

Figure 3.6. The gas cell.

When filling the cell, the entire system including the regulator on the gas bottle was evacuated and filled with the sample. This was repeated two or three times to flush out the apparatus before the final fill was done. During this procedure, the valve on the gas cell was opened and closed several times to free any pockets of air that may have been trapped in the mechanism of the valve. This was particularly important when dealing with nitric oxide. Pressures in the cell were kept at a few Torr above atmosphere so that gases on the outside could not be drawn in through a slow leak. (No leaks could be found upon testing with the He leak detector. Out-gassing was minimal).

3.6 Preparation of Nitric Oxide

Being highly reactive, NO will quickly getter oxygen from the air or surface of the container in which it is being held to form an equilibrium system with its other oxides including N_2O, NO_2, N_2O_4, and N_2O_3. The properties of these compounds are briefly outlined in table 3.2 below.[8]

Table 3.2 MELTING AND BOILING POINTS OF THE OXIDES OF NITROGEN

Name	Symbol	Melting Point	Freezing Point	Colour
Nitric Oxide	NO	-151.7 °C	-163.6 °C	pale blue
Nitrogen Dioxide	NO_2	21.15 °C	-11.3 °C	brown
Dimer of NO_2	N_2O_4	21.15 °C	-11.3 °C	brown
Nitrogen Trioxide	N_2O_3	3.5 °C	-102.6 °C	brown, green, blue
Nitrous Oxide	N_2O	-89.5 °C	-102.4 °C	colourless

Because all of these compounds with the exception of NO will freeze out at temperatures below -102.6 °C, it is possible to separate the nitric oxide from the remainder of the oxides by standard vacuum distillation techniques.[9]

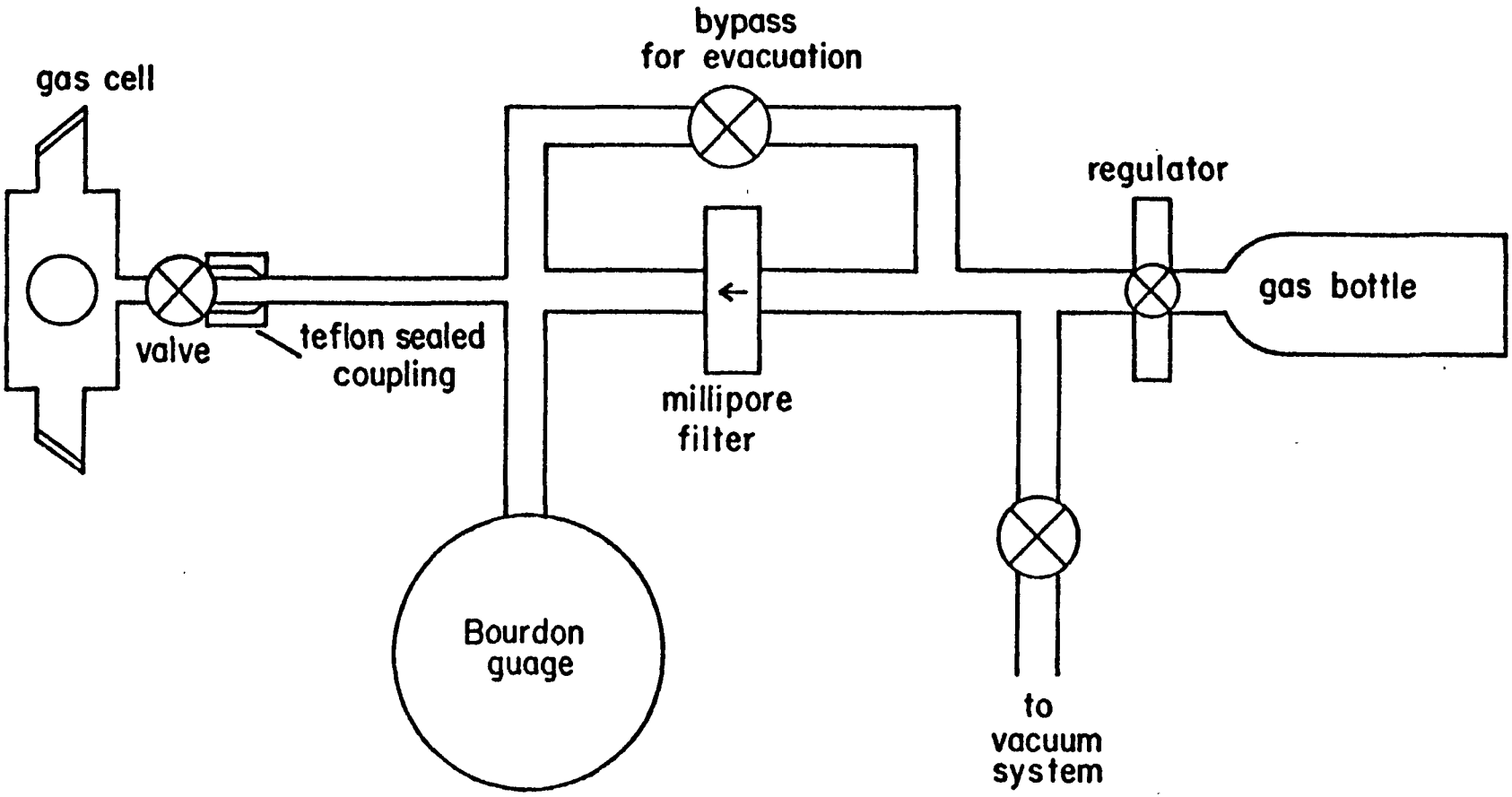

Figure 3.7. Gas fill system.

To this end a solution of cyclohexane having a freezing point of -126° C was prepared and was used to force the separation.

A schematic diagram of the vacuum distillation system is shown in figure 3.8. The apparatus is initially evacuated up to the high pressure valve on the gas bottle and then a sample of NO to be purified is passed in through the millipore filter and the P_2O_5 water vapour trap. The method used to isolate a sample of NO is the standard one of transferring the sample back and forth through a bath sufficiently cold to trap out the impurities but not the sample. The NO is forced through the bath by the application of liquid nitrogen to the traps on either side. Care was taken to remove non-condensables that would hinder the movement of the sample back and forth under the action of the liquid nitrogen and which also might be trapped in a matrix of the sample.

Two passes through the trap were sufficient to remove enough of the unwanted oxides that their presence was not detectable. (NO's large absorption cross section at visible wavelengths would halt intra-cavity action or become visible as an orange flourescence if it were present in the sample). The purified sample was then passed into the gas cell through a Swage-lok coupling between the system and the cell. The cell and vacuum apparatus had previously been seasoned overnight with NO to prevent oxygen adsorbed on the wall from reacting with NO in the cell after a sample had been purified and isolated. The cell was sufficiently leak proof that the samples of NO could be contained for three weeks with no apparent degradation and may have held longer but for lack of patience with the experimenter.

3.7 Plate Spacing Measurements

Accurate plate spacing determinations (and hence free spectral ranges) were made using the method of fractional orders.[10] In this procedure, a scan

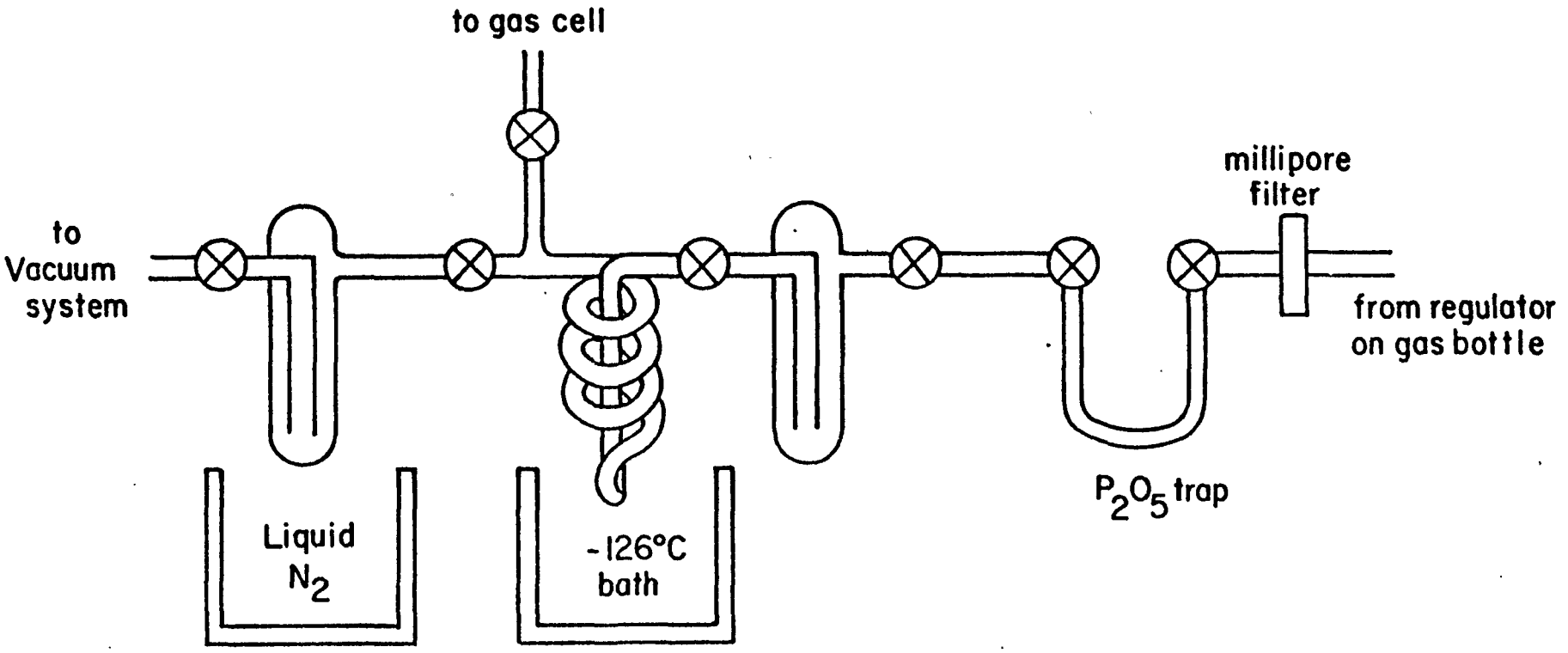

Figure 3.8. Vacuum distillation system.

of a free spectral range was made using several different laser wavelengths (section 3.3 gives the precise wavelengths used) and the relative phase shifts between them were then measured. See figure 3.9. From equation 2.2 we have

that $$2k_i\ t = n + \varepsilon_i$$

where

k_i = the i^{th} wavelength

n = an integer, the order of the interferometer

and $0 < \varepsilon_i < 1$ is the fractional amount that the spacing t is off from being an exact order.

Inverting this, if one knows k_i and measures ε_i, a series of spacings $\{t_n\} = \frac{1}{2k_i}(n+\varepsilon_i)$ can be generated, each of which will have the required phase shift. These sets are then compared to find those values of t held in common and this will be the required spacing. For this method to give a unique answer, the plate spacing must be known to lie within a reasonably small region of values. When four wavelengths from the Argon ion laser were used, this range amounted to 280 orders or approximately 3 thousandths of an inch. Consequently the etalons were set to within a few thousandths of the expected value using feeler guages. This was not a difficult procedure.

The above calculations were computerized with account being taken of the limited accuracy to which a phase shift could be measured. That is, correspondences between plate spacing estimates given by different wavelengths were considered equal if they fell to within the accuracy set by the measurement of a phase shift, typically $\pm$ 5% of an order. In addition. the light used to perform the measurements came from the same scattering volume as the light used in the actual experimental runs. Thus, any angular effects due to

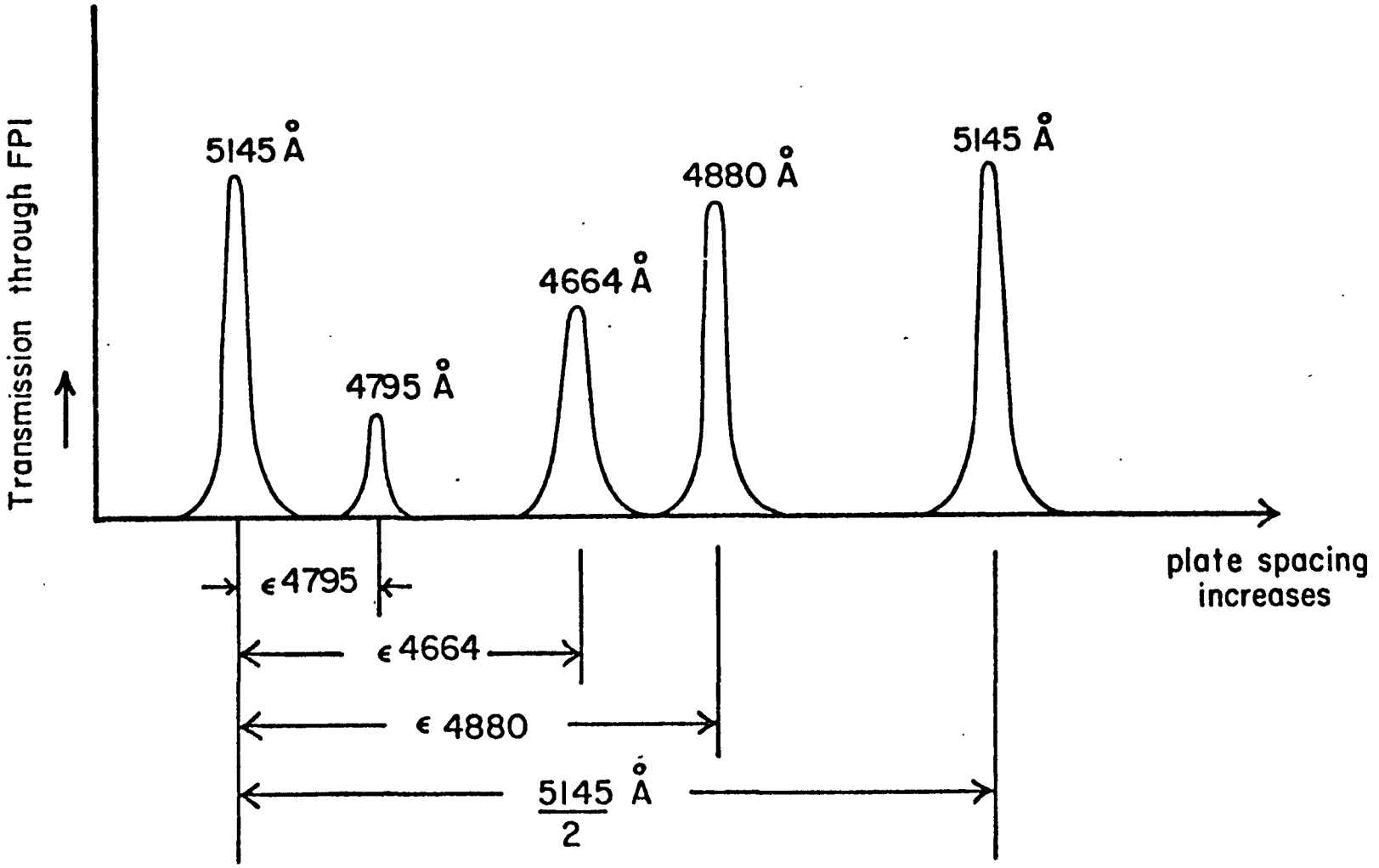

Figure 3.9. Plate spacing measurements.

the $\cos \theta$ term in the phase were removed.

Phase shifts incurred at the dielectric coatings on the mirrors do not cause difficulties as these shifts are approximately the same for all wavelengths and can be incorporated into the equations in such a fashion that the true plate spacing is augmented by an amount $\Delta' t$ (a constant depending upon the phase shifts). But, this new spacing $t + \Delta t$ is used in all calculations and is measured in all experiments so that its effects are never noticed (at least in the quantities measured here).

The accuracy to which the spacing can be measured is equal to the full width of a fringe at half maximum and this amounted to approximately 50 Å for the wavelengths and finesses commonly used in these experiments.

References

1. J. Born, Dept. of Astrophysical Sciences, Princeton Univ.

2. D. L. Mickey, P. Zucchino, and W. H. Smith, Rev. Sci. Inst., 41, 276 (1970).

3. R.C.A. Photomultiplier Tube Manual, Technical Series PT-61 (1970).

4. H. Kogelnik, The Bell System Tech. Journal, March (1965), p. 445.

5. H. Kogelnik and T. Li, Applied Optics 5, 1550 (1966).

6. Atomic Transition Probabilities Volume II, National Bureau of Standards NSRDS-NBS 22 (1969), W. L. Wiese, M. W. Smith, and B. M. Miles.

7. Tables of Spectral Lines of Neutral and Ionized Atoms, Atomic Spec. Lab. I. V. Kurchatov Institute of Atomic Energy (1968), IFI/Plenum New York, A. R. Striganov and N. S. Sventitskii.

8. Matheson Gas Data Book, Fourth Edition.

9. Denny, Techniques and Methods in Organic and Organometallic Chemistry (M. Deker, New York, 1969), p. 33.

10. M. Born and E. Wolf, Principles of Optics, (Pergamon Press, New York, 1959), pp. 338-340.

SECTION 4

MULTIPLEXING ROTATIONAL RAMAN

A brief discussion of the pure rotational Raman effect will be given, leading to the multiplexing of molecular rotational Raman spectra through a Fabry-Perot interferometer and to an estimate of the width of the transmitted interferograms. The apparatus is first tested at the 4_B and 8_B resonances of carbon dioxide, the accuracy of the procedure determined, and then nitric oxide, a more complex system and atmospheric pollutant, is studied to give an indication of the resolving power of the technique. Finally, a search is made for the pure rotational Raman spectrum of methane.

4.1 The Rotational Raman Effect

Raman scattering[1] is the inelastic scattering of light from a quantum mechanical system with the energy change in the light reflecting the energy transitions in the scatterer. Because the cross-section for the rotational Raman process depends upon the system having a time dependent polarizability, Raman studies give information about systems unable to radiate by normal dipole transitions.

In the case of rotational Raman, the energy levels of the system correspond to the rotational energy levels of a molecule and for a simple diatomic molecule are given by[2]:

$$E_J = BJ(J+1) - DJ^2 (J+1)^2 \qquad (4.1)$$

$$J = 0,1,2,3,\ldots$$

where

J = the rotational quantum number

B = $h/8\pi cI_o$, the rotational constant for the ground state level

I_o = the moment of inertia

D = the centrifugual distortion constant.

At room temperature with vibrational energies on the order of 2500 cm^{-1}, only the ground state will have a significant population.

The selection rules[3] for rotational Raman in the case of a singlet ground state are $\Delta J = 0, \pm 2$ yielding a rotational Raman spectrum that consists of elastic scattering ($\Delta J = 0$) forming one component of Rayleigh scattering, and two side bands Stokes ($\Delta J = 2$) and anti-Stokes ($\Delta J = -2$). The displacements of the Raman lines from the exciting line will be:

$$|\Delta E| = (4B-6D)(J+3/2) - 8D(J+3/2)^3 \qquad (4.2)$$

$$J = 0,1,2,\ldots$$

Values of the molecular constants B and D for gases used in the experiments are given in table 4.1 below, along with cross-sections and depolarization ratios when available or appropriate. For comparison, the N_2 Raman Q branch at 2331 cm^{-1}, a vibrational mode, has a cross-section of $5.4 \times 10^{-31} cm^2$.

The intensity of the Rayleigh light viewed along a given direction and having a polarization vector making an angle θ to the incident polarization vector will be [12]

Table 4.1. MOLECULAR DATA

Reference	Gas	$B_o(cm^{-1})$	$D \times 10^6 (cm^{-1})$	$\sigma_{Ram} \times 10^{29} cm^2/ster$	$\sigma_{Ray} \times 10^{28} cm^2/ster$	ρ_{Ray}
4.4	CO_2	.39027	.129	17.38*	4.81†	.02
4.5	O_2	1.437682	4.85	4.28*	1.82†	.014
4.6	N_2	1.98950	5.48	1.64*	2.12	.012
4.7	Xe				11.55	1.55×10^{-4}
4.8	CH_4	5.24059	108.55		4.56	1.27×10^{-4}
4.9	NO $\pi 1/2$	1.671854	.34		2.2†	
	NO $\pi 3/2$	1.720178	10.24		2.2†	

* differential backscattered cross-section summed over scattered polarization at 4880 Å

† calculated using index of refraction data

Total Rayleigh cross sections are at 6943 Å.

$$I_{Ray}(\theta) = I_{Ray}(o)\ [p + (1-p)\cos^2\theta]. \qquad (4.3)$$

A similar expression can be written for rotational Raman scattering with p = 3/4. That is, completely depolarized.

$$I_{Ram}(\theta) = I_{Ram}(o)\ [3/4 + 1/4\ \cos^2\theta]. \qquad (4.4)$$

The total intensity I* (Φ) scattered at an angle Φ to the incident polarization vector is

$$I^*\ (\Phi) = I\ (o)\ [2p + (1-p)\sin^2\Phi]. \qquad (4.5)$$

with the appropriate p and I (o) being substituted for Rayleigh or Raman scattering. The ratio β of Raman to Rayleigh scattering is maximized for the situation illustrated below where the scattering is observed in a direction parallel to the incident polarization.

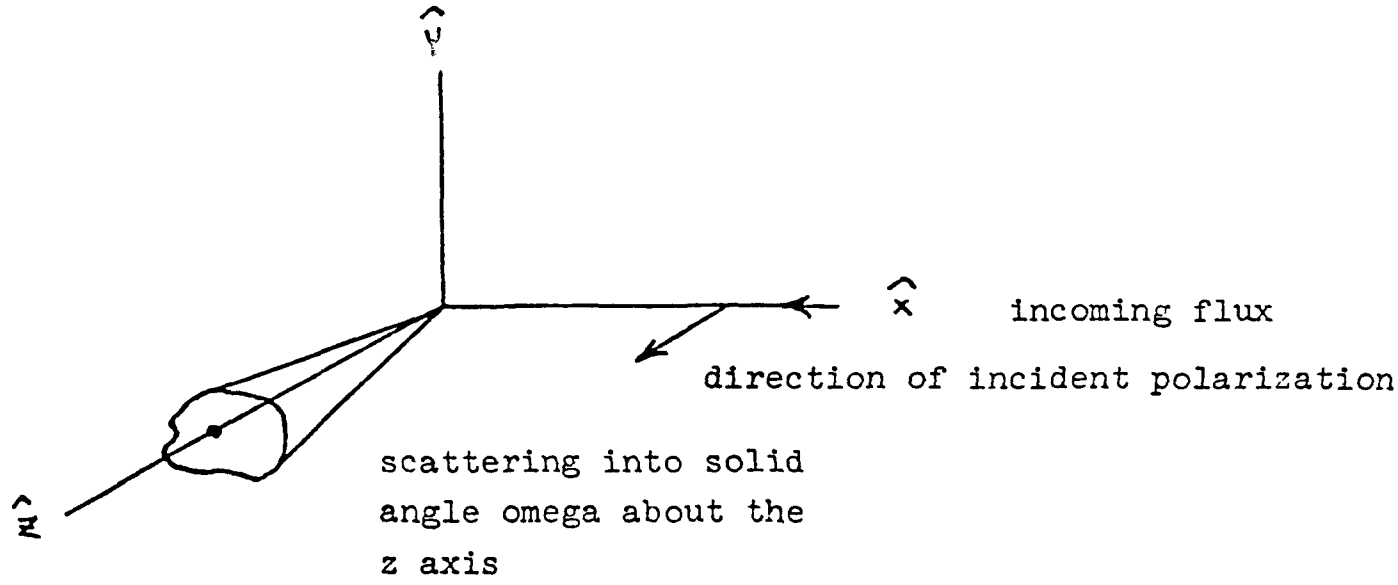

For a small viewing angle Ω, this may be approximated by

$$\beta = \frac{\sigma_{Ram}^{(o)}}{\sigma_{Ray}^{(o)}} \cdot \frac{[1/4\ \Omega + 3\pi]}{[(1-p)\ \Omega + 4\pi\rho]} \tag{4.6}$$

Since Ω must be kept large enough to obtain reasonable photon counting rates, β cannot be optimized to $\frac{3\sigma_{Ram}}{4\sigma_{Ray}\rho_{Ray}}$. In practice, with an f/3 collecting lens, β was about unity, and Raman count rates were up to 100 kHz.

The intensity distribution of both the Stokes and anti-Stokes scattering as a function of energy for rotational Raman scattering is primarily Boltzman with additional factors from the matrix elements as well as nuclear spin statistics influencing these intensities. Placzek and Teller[10] have calculated in detail the line strengths and these are given in appendix A along with the line strengths for the case of a degenerate ground state. As with Rayleigh scattering there is an ν^{14} dependence on the scattered frequency.

The selection rules for NO are modified because it has a doublet ground state. Equation 4.2 becomes[11]

$$\Delta J = 0, \pm 2$$

with $$|\Delta E| = (4B-6D)\ (J+J_{min}+ 3/2) - 8D(J+J_{min}+ 3/2)^3 \tag{4.7}$$

for $$|\Delta J| = 2$$

and $$|\Delta E| = 2B(J+J_{min}+ 1) - 4D(J+J_{min}+ 1)^3 \tag{4.8}$$

for

$$|\Delta J| = 1$$

where

J_{min} = 1/2 for the π 1/2 state of NO

J_{min} = 3/2 for the π 3/2 state of NO.

Figure 4.1 gives the pure rotational Raman stick spectra of two imaginary molecules with the same B value so that comparisons of the different expected Raman spectra may be made. Part a shows line separations for a non-degenerate ground state (say CO_2 negelecting nuclear statistics), the first line falling a distance 6B from the Rayleigh line with successive lines separated by 4B.

Parts b and c show the structure for the $\Delta J = 1$ and $\Delta J = 2$ transitions of a molecule with a doublet ground state (NO). Only the spectra for the state with $J_{min} = 3/2$ are shown, but there will also be another with $J_{min} = 1/2$ and a slightly different B value. Again the important point to note is the separation of the first line in the series from the Rayleigh line as compared with the separations between successive lines of the Raman spectra itself. This fact will make it possible to pass the Raman spectra for certain Raman states through the Fabry-Perot while rejecting the Rayleigh line.

7.2 The Multiplexed Fabry-Perot Interferometer (Spin Zero Ground State)

For a rigid rotor (D = 0), the interval between rotational Raman lines, 4B, is a constant in wavenumber. Since the Fabry-Perot can be set to arbitrary values by altering the plate spacing, it is possible to match the rotational spectrum to the Fabry-Perot bandpass in such a fashion that all the Raman light is transmitted through the Fabry-Perot, but the Rayleigh line is not.

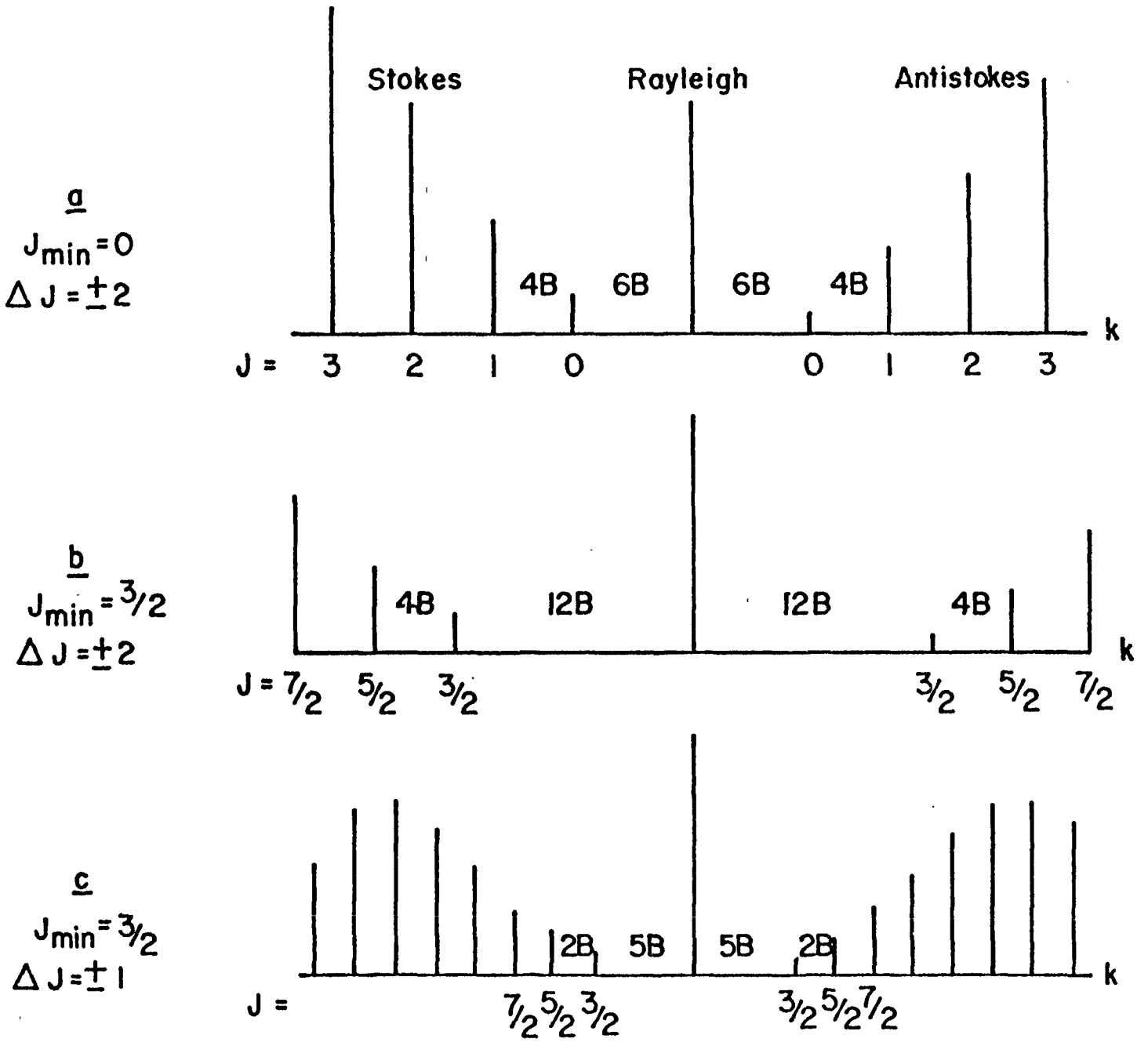

Figure 4.1. Rotational Raman stick spectra.

This is shown in Figure 4.2a, with sufficient conditions to be satisfied being:

$$\text{free spectral range} = \frac{1}{2t} = 4B \qquad (4.9)$$

$$= \frac{1}{8B}$$

and the Raman spectra be offset from the Rayleigh line by an amount not an integer multiple of 4B. This was first observed by Barrett and Meyers.[13]

It is clear that other free spectral ranges will pass many of the Raman lines and not the Rayleigh. However, the above is the only one to pass all of the Raman and exclude the Rayleigh. Other resonances are given by:

$$t = \frac{S}{8B} \qquad (4.10)$$

where s is a rational number. Two such resonances are shown in figure 4.2b,c.

As the Fabry-Perot is scanned, it is possible to imagine that the markings representing the Fabry-Perot fringes in figure 4.2 have been drawn on a strip of rubber that is being stretched so, not only is the free spectral range slowly increasing, but fringes are also moving past the lines of the spectrum. If a plot is made of plate spacing against intensity of light transmitted by the Fabry-Perot, the results will be figures 4.2a',b',c'. The intensity of the Raman light between the Rayleigh fringes will decrease slowly in amplitude as the free spectral range moves away from resonance because the periodicities of the Raman and Fabry-Perot combs no longer match precisely.

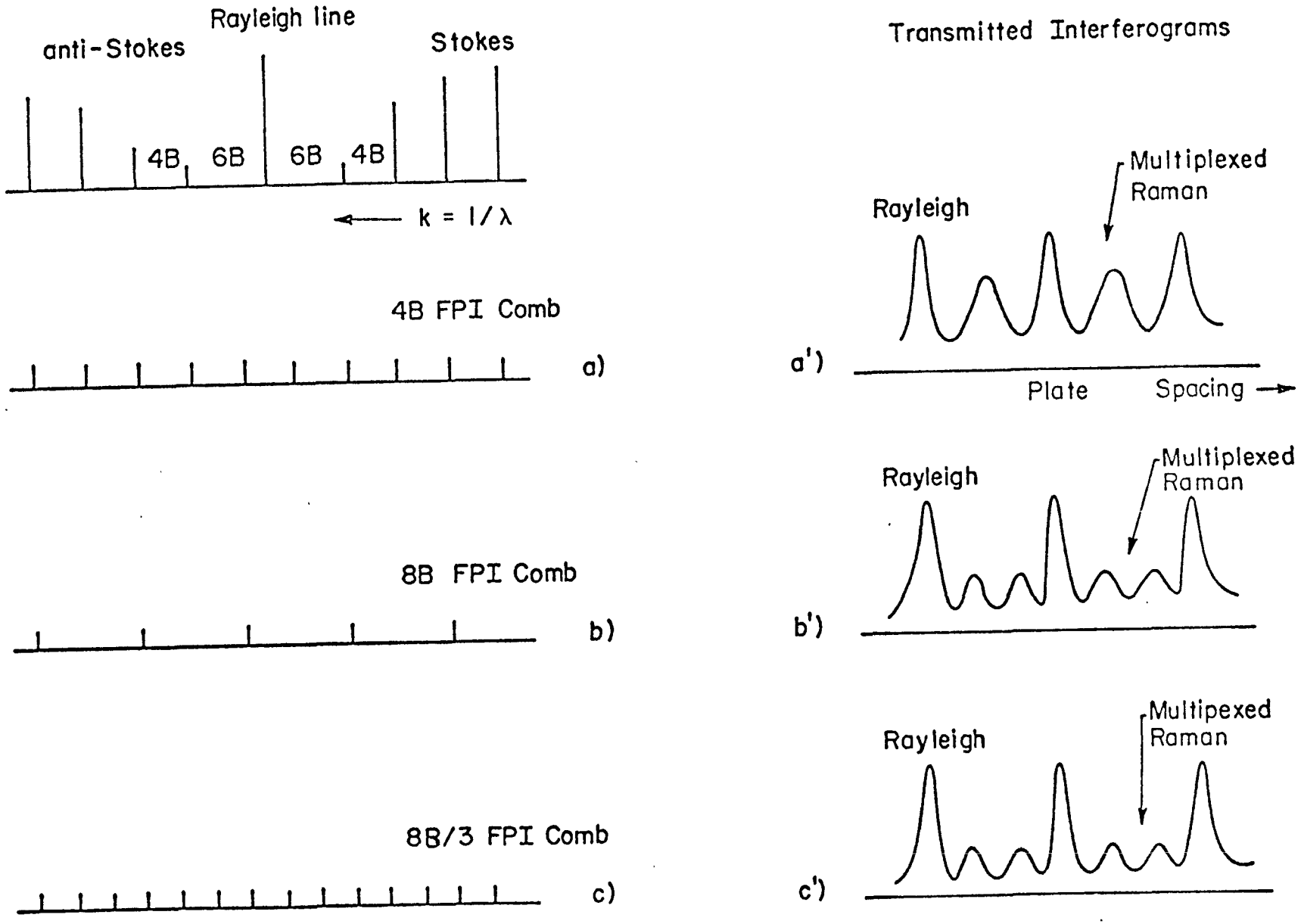

Figure 4.2. Fabry-Perot resonances.

In practice a number of additional factors must be taken into account. Finite widths of both the Raman lines and Fabry-Perot fringes cause the pattern to smear out and become smoother than that generated by the stick spectra of figure 4.1. In addition, real molecules have D values differing from zero and although on the order of 10^{-5}-10^{-6}B, they have the effect of broadening the resonance and moving it's position towards smaller free spectral ranges (fsr). This shift was estimated by Barrett and Meyers[13] for N_2O by arguing that the portion of the spectrum contributing most strongly to the transmitted pattern is near the peak of the Boltzman distribution. The distribution is:

$$\sim(2J+1)e^{-BJ(J+1)hc/kT}$$

with the peak at

$$(2J_{max}+1)^2 = \frac{2kT}{Bhc}$$

The line positions are given by equation 4.2 and so the fsr at $J = J_{max}$ is

$$E_{J_{max}+1} - E_{J_{max}} = 4B - 8D(3J^2+12J+13). \qquad (4.11)$$

The correction to the B value being

$$2D(3J^2_{max}+12J_{max}+13). \qquad (4.12)$$

Typical values at room temperature for a 4B fsr are given in table 4.2 below.

Table 4.2. RESONANCE DISPLACEMENTS DUE TO DISTORTION EFFECTS

Gas	$B(cm^{-1})$	$Dx10^{6}(cm^{-1})$	$\sim J_{max}$	$\Delta B(cm^{-1})$	change in plate spacing
CO_2	.39027	.135	16.4	$2.7x10^{-4}$	∿8.9 orders
O_2	1.437682	4.85	8.3	$3.09x10^{-3}$	∿7.5 orders
N_2	1.98950	5.48	7.0	$2.7x10^{-3}$	∿3.4 orders
NO $\pi 3/2$	1.720178	10.24	7.6	$5.68x10^{-3}$	∿9.6 orders
NO $\pi 1/2$	1.671854	.34	7.7	$1.92x10^{-4}$	∿3.4 orders

Because the position of the Boltzman peak is temperature dependent, it should be possible in principle to measure the fsr at which a resonance occurs for two different temperatures of the sample and from this calculate D. In practice, line broadening, statistics, and impurity scattering make the absolute shift of the peak difficult to measure for temperature changes less than several hundred degrees.

A measure of how the rotational constant B of the molecule affects the width of the resonance (the number of orders across the transmitted interferorgram at half maximum) is important in that distinguishing resonances from simultaneous scattering from two different B value states will be more difficult if their respective resonances are so broad as to overlap. An estimate can be made as follows.

The J value which the Boltzman distribution falls to some chosen fraction of its peak will go roughly as $B^{-1/2}$ and correspondingly, the number J value across the Stokes-anti-Stokes distribution will be approximately proportional

to $B^{-1/2}$. For the intensity of the transmitted interferogram to fall to half of its peak value, the FPI (Fabry-Peort interferometer) lines that correspond to the J values at the 'edges' of the Stokes-anti-Stokes distribution at resonance, must move off their positions by some amount ε, and we may write

$$\varepsilon \propto \Delta\sigma \times \{\#\text{ of J values across the distribution}\} \qquad (4.13)$$
$$\propto \Delta\sigma\ B^{-1/2}$$

where $\Delta\sigma$ is the change in fsr that moves one to the half peak intensity position of the transmitted interferogram. But, ε must go as the line width (proportional to B since the finesse is constant and fsr = 4B)

$$B \propto \Delta\sigma\ B^{-1/2}$$

and using

$$\frac{\Delta t}{t} = -\frac{\Delta\sigma}{\sigma} = -\frac{\Delta B}{B} \qquad (4.14)$$

find

$$\Delta t \propto B^{-1/2} \qquad (4.15)$$

That is, the width of the transmitted interferogram will go approximately as $1/\sqrt{B}$ (assuming FPI width >> laser line width).

If the lines are broadened beyond the Airy width, the transmitted interferogram will be even wider and will change more rapidly than $B^{-1/2}$ for small Airy widths compared to the line widths. Half widths or resonances obtained by computer calculations neglecting the effects of line width, may be in error, but the general structure can be found without time consuming integrations over these line widths.

Very recent computer simulations in the literature suggest that two closely lying resonances may be resolved,[14] but data presented in this thesis on NO with four effective scattering states demonstrates that this spectrum is difficult to interpret without prior knowledge of the approximate form of the transmitted interferogram. The hot bands of certain molecules may be observable if the temperature is sufficiently high as to populate them well with respect to the ground state and if their resonances are narrow enough so as not to overlap in a destructive fashion.

The procedure to follow when measuring an unknown B value is to set up the apparatus as in figure 3.1, and scan the Fabry-Perot until the peak of the resonance is found. The plate spacing can then be measured as described in section 3.7 and the effective B value calculated from equation 4.9. In general, the effects of distortion are not precisely known, and the error in the measurement of the peak position can be on the order of the values given in table 4.2 above. Since these errors are so large, it is not necessary to account for the change with pressure of the index of refraction of air between the FPI etalons. This creates an error of approximately .1 orders for a change of 50 Torr.

4.3 Analysis of CO_2 8B Resonance

The etalons used for this portion of the experiment were of reflectivity 0.86. This, coupled with the broad laser line width and small B value of carbon dioxide make the 8B resonance more suitable than the 4B resonance for a measurement of the rotational constants because its features are less washed out by the effects of broad line width. A single large Raman peak is not formed between the Rayleigh fringes at this fsr (see figure 4.2b) and the method of maximizing the Raman signal to define the resonance position is not applicable.

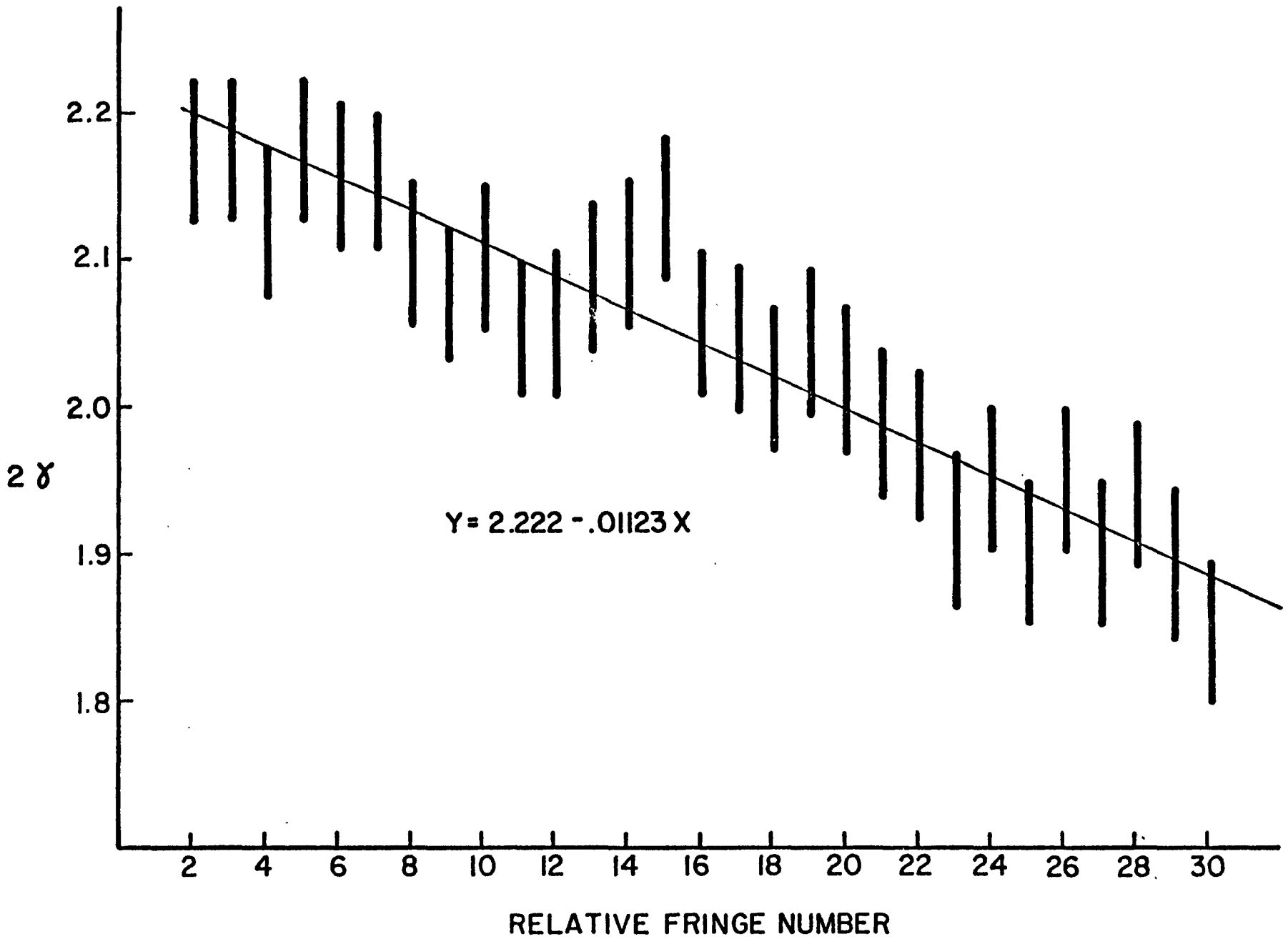

Figure 4.3. Plot of normalized stokes-antistokes fringe separation versus the relative order of the interferometer.

Consideration of figure 4.2b for the case of CO_2 with odd rotational lines absent indicates that at an 8B resonance, the distance between Stokes and anti-Stokes peaks is half the distance between the Rayleigh peaks to either side, while at fsr's smaller than the resonance, the peaks move closer to the Rayleigh lines and vice-versa for larger fsr's. Figure 4.3 shows a plot of γ versus relative order number with

$$\gamma = \frac{\text{distance between Rayleigh fringes}}{\text{distance between Raman peaks}}$$

and the FPI scanned over several orders in the neighborhood of the resonance.

Gamma was found equal to 2.0 at relative order number 19.75 ± 1.38 where the data was fitted to a straight line using the least squares method and the errors determined by requiring a confidence of 95%. The relevant figures are given below.

$$\gamma = -.01123n + 2.222$$

$$N = 29 = \text{number of data points}$$

$$s = 0.0399 = \sqrt{\frac{\Sigma\ (\text{residuals squared})}{N-2}}$$

$$t_{0.05}^{(N-2)} = 2.05 = \text{Student's distribution}$$

A plate spacing determination was done at relative order number 10, with the wavelengths and fractional orders for this measurement given in table 4.3 below.

Table 4.3.
FRACTIONAL ORDERS FOR CO_2 8B PLATE SPACING MEASUREMENT

Wavelength (Å)	Fractional shift (Å)	
	measured	calculated
5145.319	0.	0.
4879.860	1379.	1432.
4965.070	391.	389.
4764.862	659.	658.

A plate spacing t = .16004514 cm ± 50 Å gives the phase shifts of column 3 in table 4.3. Therefore the resonance occured at

$$t = 0.1602960 \text{ cm} \pm 1.38 \text{ orders}$$

giving an effective B value of

$$B_{eff} = 0.389903 \pm 0.000086 \text{ cm}^{-1}.$$

The literature value is 0.39027 cm^{-1}. B_{eff} is too small by 0.000366 cm^{-1}, which corresponds to a plate spacing error of $\Delta t \sim 6 \pm 1.4$ orders at an 8B fsr or $\sim 12 \pm 2.8$ orders at a fsr of 4B.

The expected shift due to distortion effects at the 4B resonance is given in table 4.2 as approximately 9 orders. The agreement is reasonable and it is clear that is the rotational constants B and D of a pollutant molecule are known, it will be possible to set the Fabry-Perot to pass the spectra of that molecule.

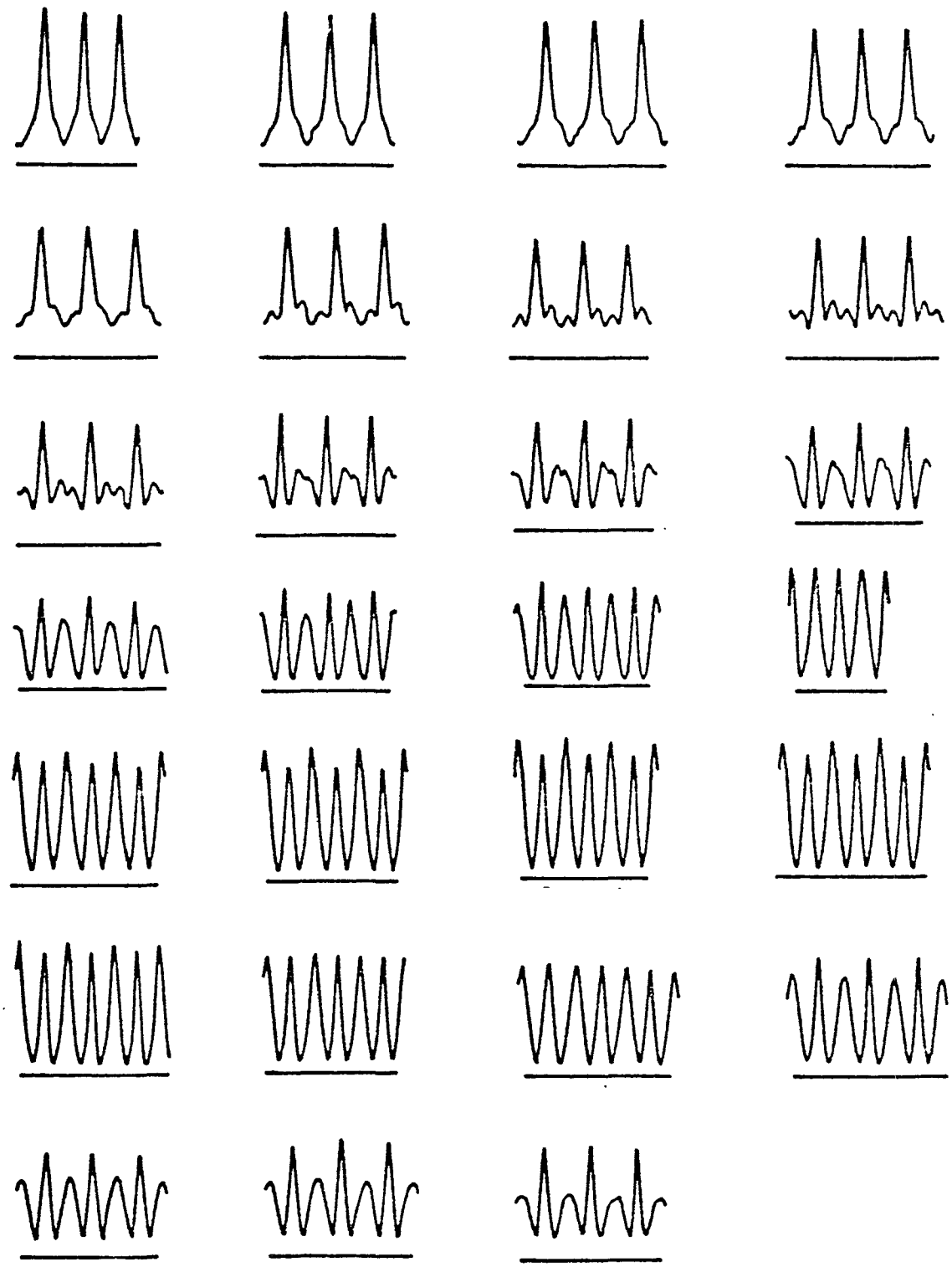

Figure 4.4. Carbon dioxide 4B resonance.

4.4 Analysis of CO_2 4B Resonance

The etalons available for this experiment were of reflectivity R = 0.94. The improved finesse over that of the reflectivity R = 0.86 etalons made possible an attempt at a fsr of 4B rather than 8B as was tested in section 4.3. The 4B resonance is a more favorable one to use when searching for weak signals such as might be expected from atmospheric pollutants because it sums all the Raman light into a single peak.

The gas cell was filled with slightly over one atmosphere of carbon dioxide and a scan done over the region of the expected resonance. The resultant data is given in figure 4.4. The Raman light can be seen to emerge from the wings of the Rayleigh lines (the larger peak is due to Stokes scattering and the smaller anti-Stokes) and coalesce in the center forming a single peak. Its intensity exceeds that of the Rayleigh lines at resonance and the process then reverses itself as the scan continues past the peak of the interferogram.

The Raman intensity was normalized by Rayleigh intensity and a plot made versus the relative order number. As the interferogram approaches the resonance position, the Raman peaks increase in height and the Rayleigh lines decrease because of the Raman light which was previously scattered throughout the order merging in the center. The normalization procedure enhances this peaking effect while additionally providing scaling against laser intensity fluxuations.

A least squares fit to a parabola was attempted with the coefficients found to be

$$a_o = 0.4694 \pm 0.0389$$

$$a_1 = 0.1923 \pm 0.0119$$

$$a_2 = 0.01338 \pm 0.000773$$

where

$$\frac{\text{Raman}}{\text{Rayleigh}} = a_o + a_1 p + a_2 p^2$$

and the relative order number n is given by

$$n = 111.0 + 10.0\ p.$$

The peak occurs at

$$-\frac{a_1}{2a_2} = 7.186 \pm 0.609$$

which corresponds to order number

$$n = 182.8 \pm 6.1.$$

The errors reflect the one σ limit and have been calculated using

$$s = \sqrt{\frac{\Sigma(\text{residuals squared})}{N-3}} = 0.042$$

and

$$\sigma_{a_i} = s\sqrt{c_{ii}} = \text{standard deviation of the } a_i \text{ coefficient}$$

where the c_{ii} are the matrix elements of the inverse normal equations' matrix (see Experimental Statistics, NBS handbook 91, M. Natrella).

Plate spacing determinations were carried out at relative order numbers 141 and 261. The fractional orders and wave lengths for these measurements are given in table 4.4 below.

Table 4.4. FRACTIONAL ORDERS FOR CO_2 4B PLATE SPACING MEASUREMENT

Wavelength	shifts fringe #141		shifts fringe #261	
	measured	calculated	measured	calculated
4879.860	0	0	0	0
5145.319	1533	1609	1213	1251
4965.070	240	183	158	78
4764.862	160	179	2237	2255

The plate spacing determined for fringe number 141 is

$$t = 0.3214119 \text{ cm} \pm 50 \text{ Å}$$

with fractional orders given in column 3 of table 4.4. The plate spacing determined for fringe number 261 is

$$t = 0.3185084 \text{ cm} \pm 50 \text{ Å}$$

with the fractional orders given in column 5 of table 4.4.

The two measured distances are 119 rather than 120 orders apart because of a fringe counting error as the Fabry-Perot was adjusted by hand to extend the range of the PZT stacks.

Since the peak was found to occur at relative order number 182.8, the plate spacing at which the resonance occurred was

$$t = 0.3204042 \text{ cm} \pm 6.6 \text{ orders}$$

where the error now includes the effect of the miscounted fringe as well as the degree of the curve fit. The effective B value calculated from this is

$$B_{eff} = \frac{1}{8t} = 0.39013 \pm 0.0002 \text{ cm}^{-1}$$

and when the correction for the distortion shift of ± 8.5 orders is accounted for, this becomes

$$B = 0.39030 \pm 0.0002 \text{ cm}^{-1}.$$

The literature value is B = 0.39027 cm^{-1}, giving a disagreement of 0.00003 cm^{-1} or $\sim$ 1 order. The agreement is better than that for the 8B resonance but, is probably a chance coincidence, the large error bars reflecting the effects of the broad line widths and small fsr washing out the peak position.

4.5 Analysis of Nitric Oxide Data

As noted in section 4.1, the selection rules for NO rotational Raman are $|\Delta J| = 0,1,2$. Since these arise as a result of a doublet ground state, it is as if there were four separate molecular species contributing to the Raman scattering, with the resultant transmission of the spectrum through the FPI expected to be complex. The half integer spin of the NO ground states ($J_{min} = 1/2,3/2$) gives the rotational Raman spectra a displacement from the Rayleigh line of 8B and 12B respectively for these states. The conditions for an interferogram that rejects the Rayleigh line and sums all of the Raman lines are violated for $\Delta J = \pm 2$ and the 4B pattern are of no value in searching for NO Raman. The $\Delta J = \pm 1$ rotational Raman spectra was therefore observed (a 2B pattern) although its intensity is weaker than that of the scattering with $\Delta J = \pm 2$.

The presence of NO as an atmospheric pollutant gives impetus to the study of its rotational Raman spectrum. In the temperatures found in a smokestack plume, the NO does not react with O_2 to establish a significantly high equili-

brium population of its other oxides and thus alone becomes the candidate for observation. This is somewhat unfortunate, because of its complex spectrum. Although the 2B resonance might be expected to provide the optimum summation of Raman light and rejection of Rayleigh, this will be shown to be incorrect and that other resonances of NO should be utilized for its detection.

The difficulties of preparing and containing a sample of NO have been previously discussed in section 3.6 while the B and D values for the $\pi_{1/2}$ and $\pi_{3/2}$ states can be found in table 4.1. The gas cell contained slightly over one atmosphere of NO and was positioned at the intra-cavity focus of the laser. Because the $\pi_{1/2}$ and $\pi_{3/2}$ states are so close in B value, a double passed arrangement of the FPI was used to give improved finesse and contrast. Sandercock[15] has shown that for such an arrangement, the finesse and contrast will be given by

$$f_{\text{double}} = \sqrt{2}\, f_{\text{single passed}}$$

$$C_{\text{double}} = C^2_{\text{single passed}}$$

yielding expected values for this apparatus of

$$f = 29$$

$$C = 3 \times 10^4$$

The measured values were f = 21 and 6×10^3, with the discrepancy a result of the laser linewidth.

The double passed arrangement is diagrammed in figure 4.5. The scattered light from the gas cell is collimated, and then reflected by the 45° mirror through the Fabry-Perot. A corner cube reflector returns the light along the

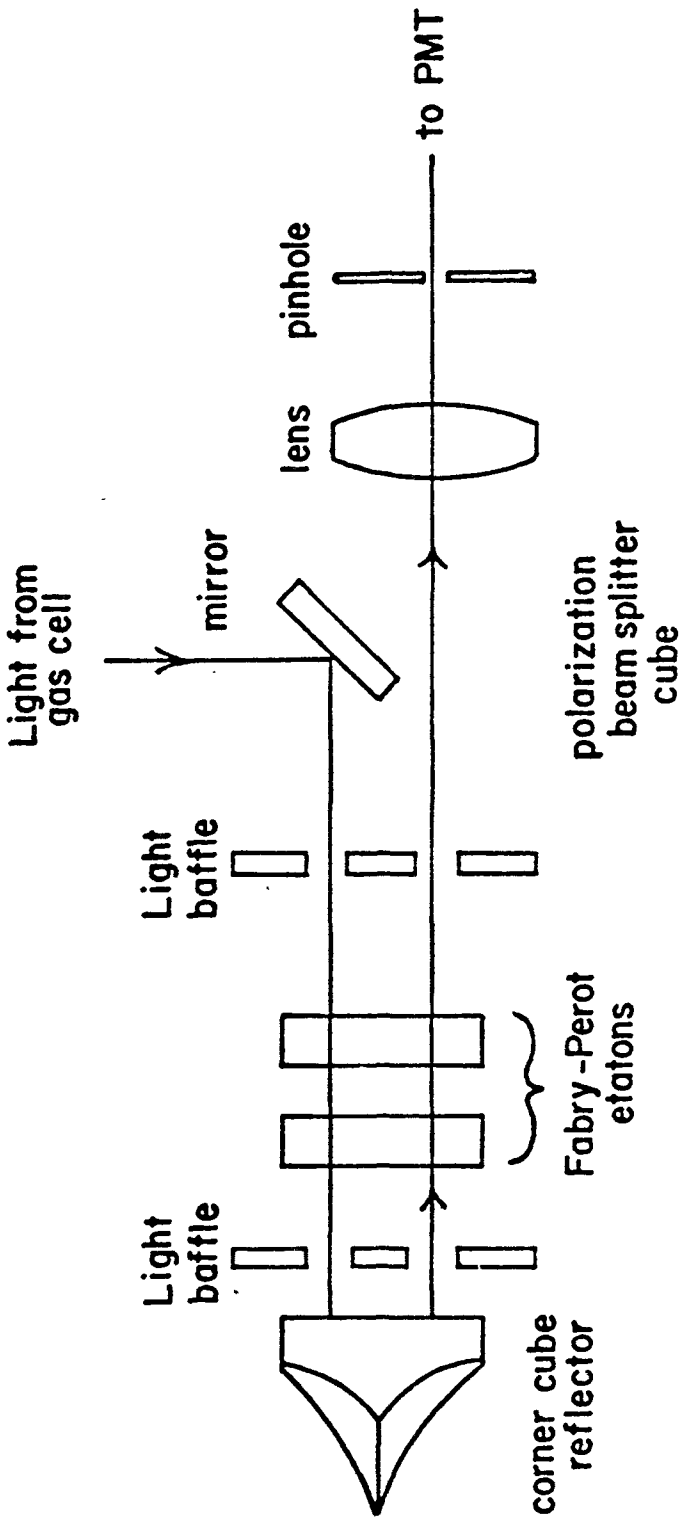

Figure 4.5. Double passed Fabry-Perot interferometer.

angle of incidence, but shifted spatially to pass through the Fabry-Perot a second time after which it is focused onto a pinhole and the photomultiplier tube. This arrangement is equivalent to the tandem passage of two Fabry-Perot but without the alignment and fsr matching problems encountered in the latter case. Care was taken to avoid front surface reflections and other sources of stray light which could have decreased the contrast.

The general features of the transmitted intensity can be estimated from figure 4.1 showing the NO spectrum set against a Fabry-Perot combe near the 2B resonance. At the $\pi_{1/2}$ resonance, the $\Delta J = \pm 2$ $\pi_{1/2}$ scattering will form a peak in between the Rayleigh fringes just as the $J = 2$ did for CO_2 at its 4B resonance (figure 4.4), while the $\Delta J = \pm 1$ $\pi_{1/2}$ scattering will accumulate behind the Rayleigh fringes because of its offset of 8B from the Rayleigh line. The transitions originating from the $\pi_{3/2}$ state will be slightly out of resonance and w'll tend to wash out the visibility of the $\pi_{1/2}$ fringes. At the $_{3/2}$ resonance, the same description will hold with the $\pi_{3/2}$ and $\pi_{1/2}$ states exchanging roles. Although the $\pi_{3/2}$ state loses intensity over the $\pi_{1/2}$ state because of the Boltzman factor, this is more than offset by the factors arising from the matrix elements, and as a result the $\pi_{3/2}$ resonance will be more intense than that of the $\pi_{1/2}$.

Using euqations 4.7, 4.8, A7, A8, A9, and A10, the spectrum of NO was calculated and a computer simulation done of its transmission through a Fabry-Peort. These results are presented in figure 4.6 along with experimental data sampled at various plate spacings through the resonance. The upper diagrams in each set are the calculations without the Rayleigh lines superimposed, the vertical bars above these diagrams the positions the Rayleigh lines would occupy, and the numbers the order numbers of the Fabry-Perot $\lambda = 5145.319$ Å.

The lower diagrams are the experimental data with the numbers above the Rayleigh lines this time representing the experimentally measured values using the method of fractional orders. The experimental data given below each calculation represents that data whose order number was closest to where the calculation was done. As the pattern does not change appreciably over 4-5 orders, this represents no serious problem where a qualitative comparison such as the above is made.

Quantitative data on B values and resonance positions was not easily obtained, because the blurring of the features of the resonances by the scattered light not in resonance caused them to have no clear cut maximum although some build up of intensity was obvious. The $\pi_{3/2}$ resonance was for example, ill defined over 25 orders, and without the aid of a model calculation, its identification would have been tenuous at best.

The $B^{-1/2}$ rule for interferogram widths is easily generalized to include $\Delta J = \pm 1$ as well as $\Delta J = \pm 2$ transitions, the effects of laser line width, and resonances other than the 4B resonance. The result is

$$\text{Width} = [1/2]g \frac{[(\sigma/f)^2+\gamma^2]^{1/2}}{\sigma B^{1/2}} \qquad (4.16)$$

where σ and f are the fsr and finesse of the FPI, g is a constant, γ is the incident line width, and the factor 1/2 is to be included for $\Delta J = \pm 2$ transitions only. Taking CO_2 4B resonance (figure 4.4) width as $\sim$ 160 orders with an incident line width of .25 cm^{-1} gives $g \sim 1295$ orders. Thus, an estimate of the NO 2B resonance widths for the $\pi_{1/2}$ and $\pi_{3/2}$ states is $\sim$ 80 orders. Since the separation between these two resonances is on the order of 150 orders, and there exists background scattering from the $\Delta J = \pm 2$ transitions, it is clear why the measurement of the peak positions for these resonances is difficult.

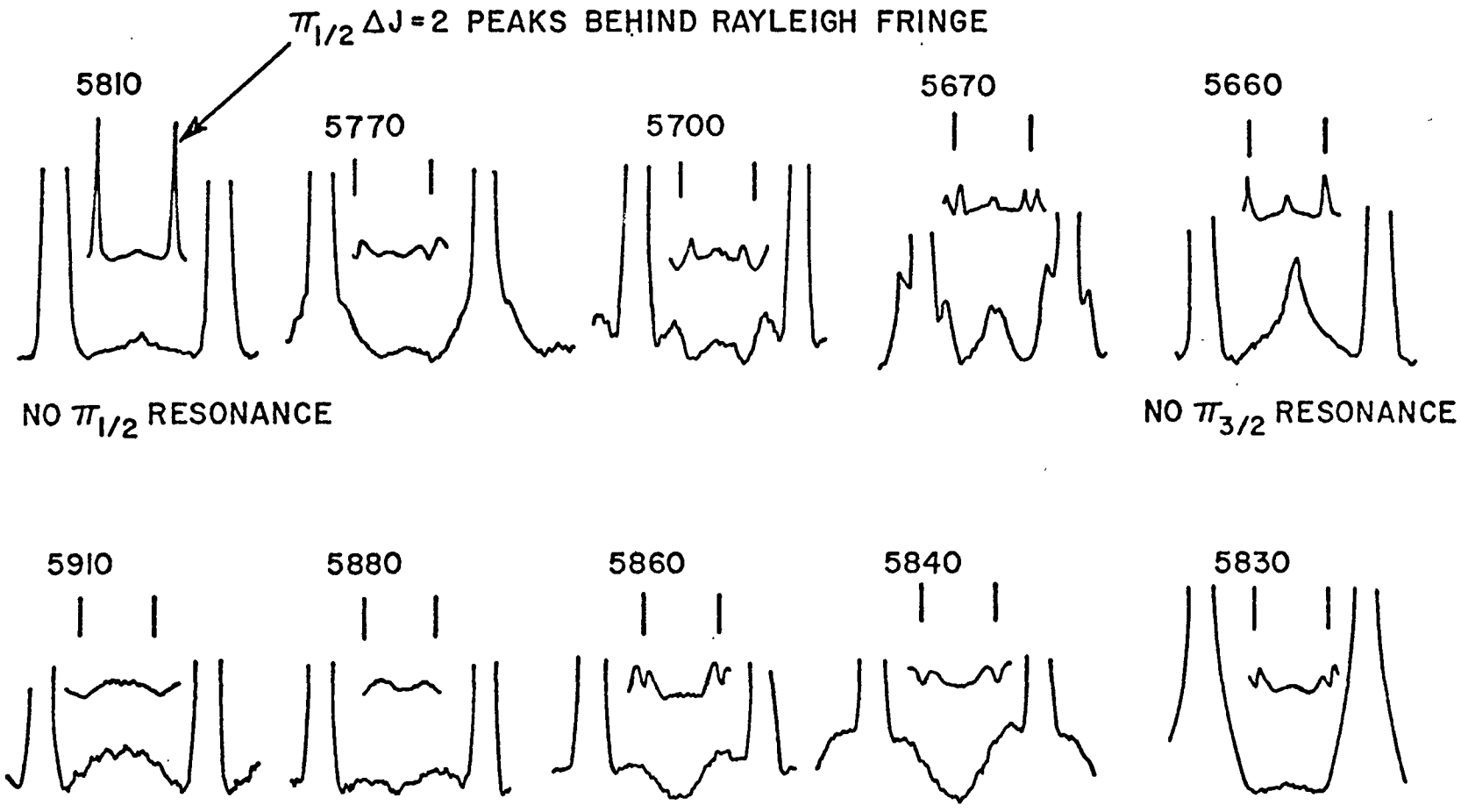

Figure 4.6. Nitric oxide 2B resonance.

4.6 The 8B/3 NO Resonance

The detection of rotational Raman from an inpurity molecular species with the multiplexed Fabry-Perot interferometer requires not only that the scattering have a sufficient cross-section, but also that its transmission profile be sufficiently well defined as to distinguish it from other resonances and from the background. The 2B resonance of NO with its intensity spread over $\sim$ 160 orders and reaching a peak value of only 1/28 that of the Rayleigh line did not satisfy these conditions.

Figure 4.7 shows a scan of the NO sample done at a fsr of 8B/3. Because of the offsets of the $J = \pm 1\pi_{1/2}$ and $\pi_{3/2}$ spectra from the Rayleigh line (figure 4.1), the peak formed at this resonance cannot be generated by scattering from these transitions and is in fact due to $\Delta J = \pm 2$ Raman. For the $\pi_{1/2}$ resonance in figure 4.10, only the odd lines contribute to the Raman peak with the even lines falling behind the Rayleigh fringe. The opposite holds true for the $\pi_{3/2}$ state which is just beginning to form into a resonance towards the end of the sequence shown. The single (as opposed to double) Raman peak between Rayleigh fringes produced at this 8B/3 resonance is a direct result of the non-zero spin of the ground rotational states which causes the Raman spectra to be shifted away from the Rayleigh line by 8B (for π 1/2) and 12B (for π 3/2) instead of the normal 6B shift found for the spin zero ground state. Computer simulations of these resonances confirm the results.

Using the generalized rule for interferogram widths derived in the previous section with g = 1295 as determined from the CO_2 4B resonance gives an expected width for the 8B/3 resonance as $\sim$ 29 orders, while the measured

width is approximately 25 orders. The agreement is good. If incident line widths had not been considered and the width was assumed to go as $B^{-1/2}$, the predicted width would have been 160x $\sqrt{\frac{.4}{1.7}} \sim 78$ orders, the error being substantial. Clearly the 8B/3 resonance is superior to the 2B resonance in terms of having a well defined and more intense peak to be detected (4.5 times the 2B resonance maximum) and should be chosen in preference to the other when it is required to ascertain whether or not NO is present in some mixture of gasses without regard to which process generated the Raman light being observed. It is not clear, however, that this is an optimal resonance to maximize intensity and Smith [16] has indicated the usefulness of long scans using an air bearing interferometer or some equivalent system to determine other resonance that may exist within detectibiltiy limits set by the line width of the laser.

4.7 A Search for Methane Pure Rotational Raman

The spherical degeneracy of methane's polarizability ellipsoid is removed by the zero point vibrational motions of the molecule leading to a slight probability for pure rotational Raman scattering. Estimates of this intensity place it anywhere from 10^{-4} to 10^{-7} down from the ordinary rotational Raman cross-sections. Since the Fabry-Perot has a large entendue enhanced by multiplexing and a strong exciting source was available in the form of an intra-cavity operated laser, a search was made for this scattering.

With the cross-section for methane pure rotational Raman scattering expected to be so small, care was exercised in minimizing extraneous light from the Rayleigh line, scattering from impurities in the sample, and dark current. The rejection method to be described in chapter 5 (figure 5.2) was used to

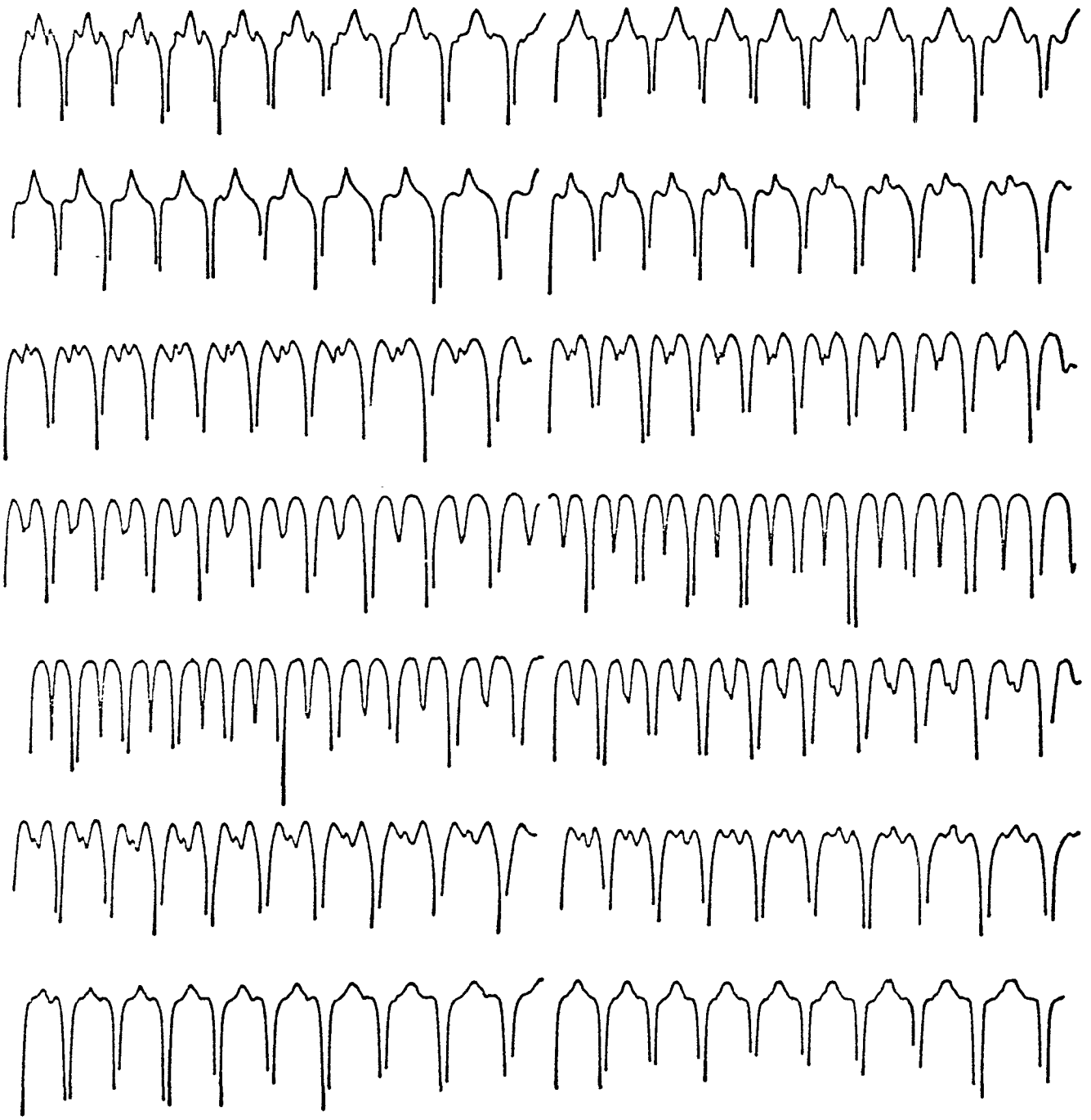

Figure 4.7. Nitric oxide 8B/3 resonance.

remove a large fraction of the Rayleigh light, and care was taken to assure the baffling of the optical elements from stray and internally scattered light. (The rejection method being more efficient in this respect than the double passed Fabry-Perot interferometer because it removes light at the entrance of the system thus eliminating the possibility of scattering from surface imperfections or scattering centers further down the optical path).

Ultra high purity methane (0.9997 purity) was passed into the gas cell through the vacuum distillation system after both had been outgassed for two days at 10^{-5} Torr. Slightly over one atmosphere pressure of methane was used with the other precautions mentioned in the section on vacuum distillation followed. As the abundance of CH_3D in CH_4 is on the order of 5 parts in 10^4, this sets a limit to the purity that may be obtained at resonable cost.

To eliminate the effects of contaminant scattering, scans were taken at two plate spacings separated by 280 orders. If the impurity scattering comes from many sources with varied B values, their expected contribution is approximately constant over many orders while the methane Raman should pak at resonance and be absent in the second scan done at the off resonance position. A chance peak could be produced by a resonance with one of the impurities at the 4B position of methane, but as no peak was observed at the resonance, this does not become consideration.

Figures 4.8 and 4.9 are the interferograms taken on-resonance (corrected for distortion shift) and off-resonance respectively, with each being the average of 10 scans and the gentle slope in the base line a result of interferometer temperature scanning coupling in slightly more Rayleigh intensity to one side than to the other. The dark count rate was 6 Hz with an estimate of the Rayleigh contribution in the Lorentzian wings being approximately 5 Hz.

The data does not permit the identification of a Raman peak, but an upper limit on the cross section for pure rotational Raman scattering can be placed by assuming that the entire count rate between the Rayleigh peaks after subtraction of the two differently spaced interferograms is due to methane. The analysis is given below.

(a) Using the generalized rule for interferogram widths with the constant g evaluated from both the NO and CO_2 data gives an expected width of 6-7 orders at half maximum for the CH_4 resonance. The CO_2 4B and 8B resonance measurements demonstrated that the peak position could be accurately predicted to within a few orders and the FPI set at that position. The expected transmittance of the CH_4 rotational Raman spectrum should therefore be in excess of 1/2.

After the subtraction of figures 4.8 and 4.9, the count rate between the Rayleigh peaks had an average value of 2 Hz. With the assumption that this is entirely due to CH_4 pure rotational Raman scattering, the Raman count rates before entering the analyzing Fabry-Perot interferometer must be where

$$\delta x2 \quad \text{Hz} \tag{4.17}$$

δ^{-1} is the single line transmission efficiency of the Fabry-Perot interferometer, its optics, the output pinhole, and photomultiplier tube. The loss of CH_4 Raman from the rejection Fabry-Perot interferometer is $\left(\frac{1-R}{1+R}\right)$ (see chapter 5) and so the Raman intensity leaving the beam splitter cube is

$$\left(\frac{1+R}{2R}\right) \delta x2 \quad \text{Hz}. \tag{4.18}$$

Equation 4.5 gives the intensity of scattered light as

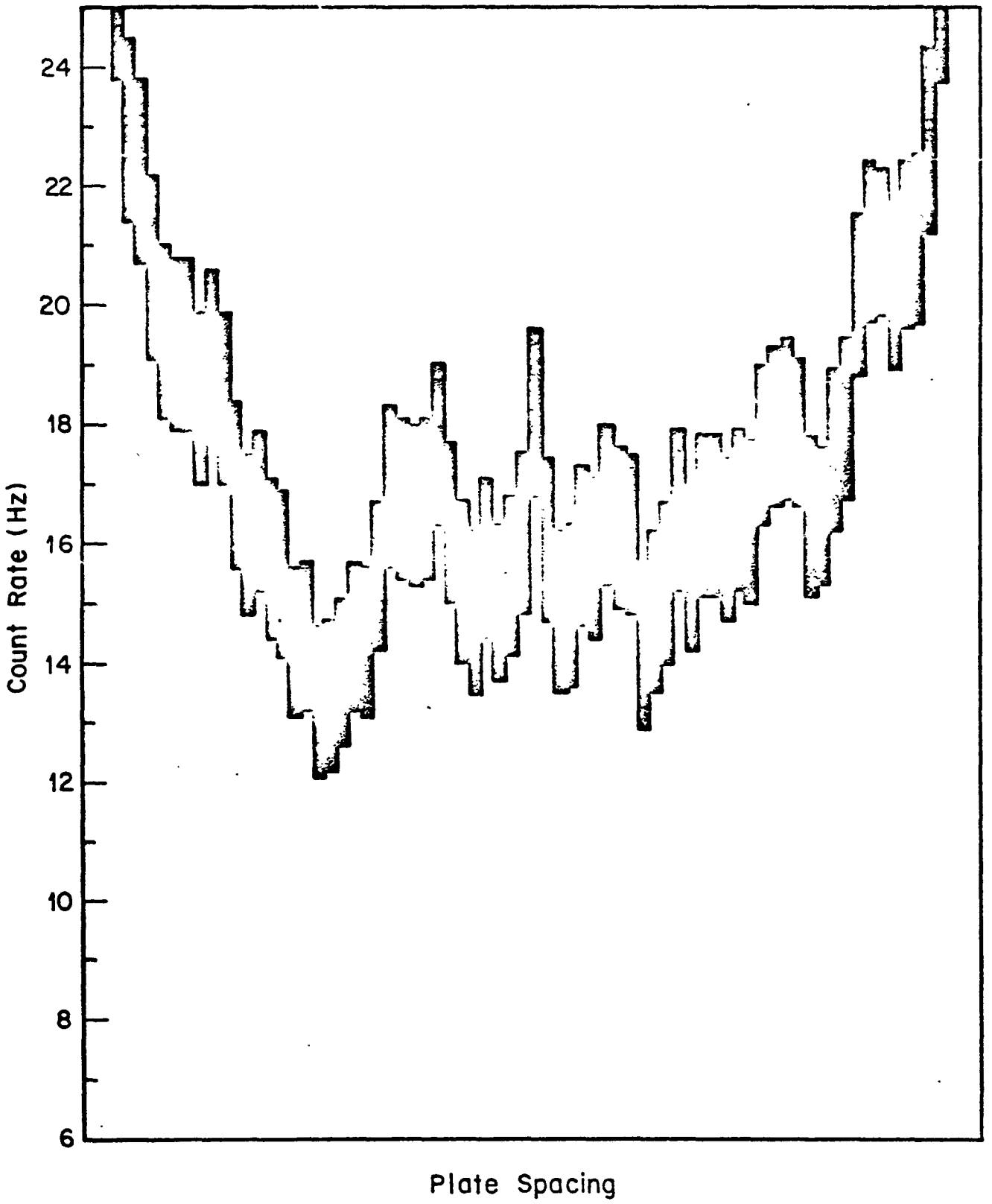

Figure 4.8. Methane at the 4B resonance.

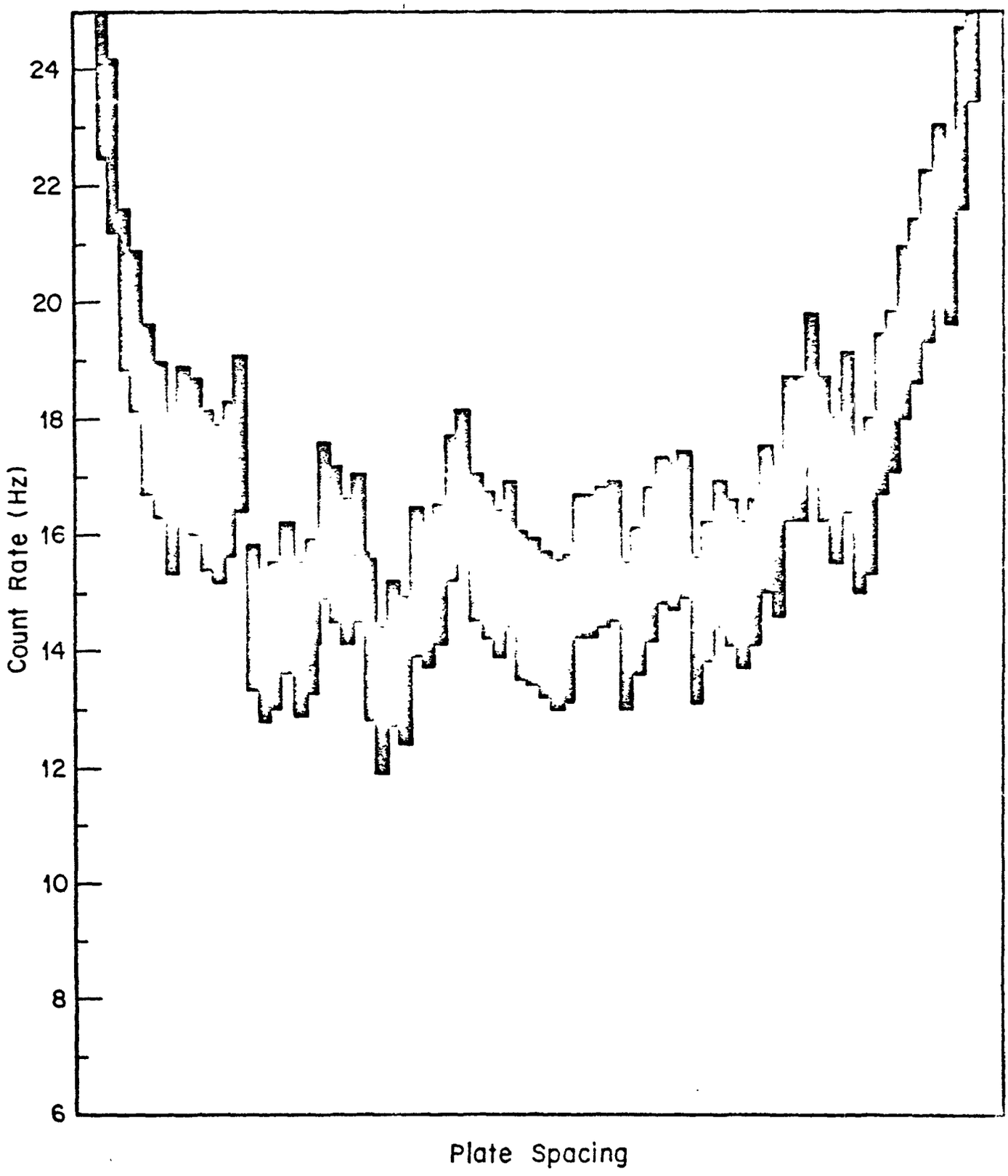

Figure 4.9. Methane off the 4B resonance.

$$I(\theta) = I_o \left[\rho_o + (1-\rho_o) \cos^2\theta \right] \qquad (4.19)$$

The scattering geometry is shown below with the incident beam along the x axis and polarized in the z direction with a viewing lens centered along the y axis. The polarization beam splitter after the lens selects the vertical component along the y axis.

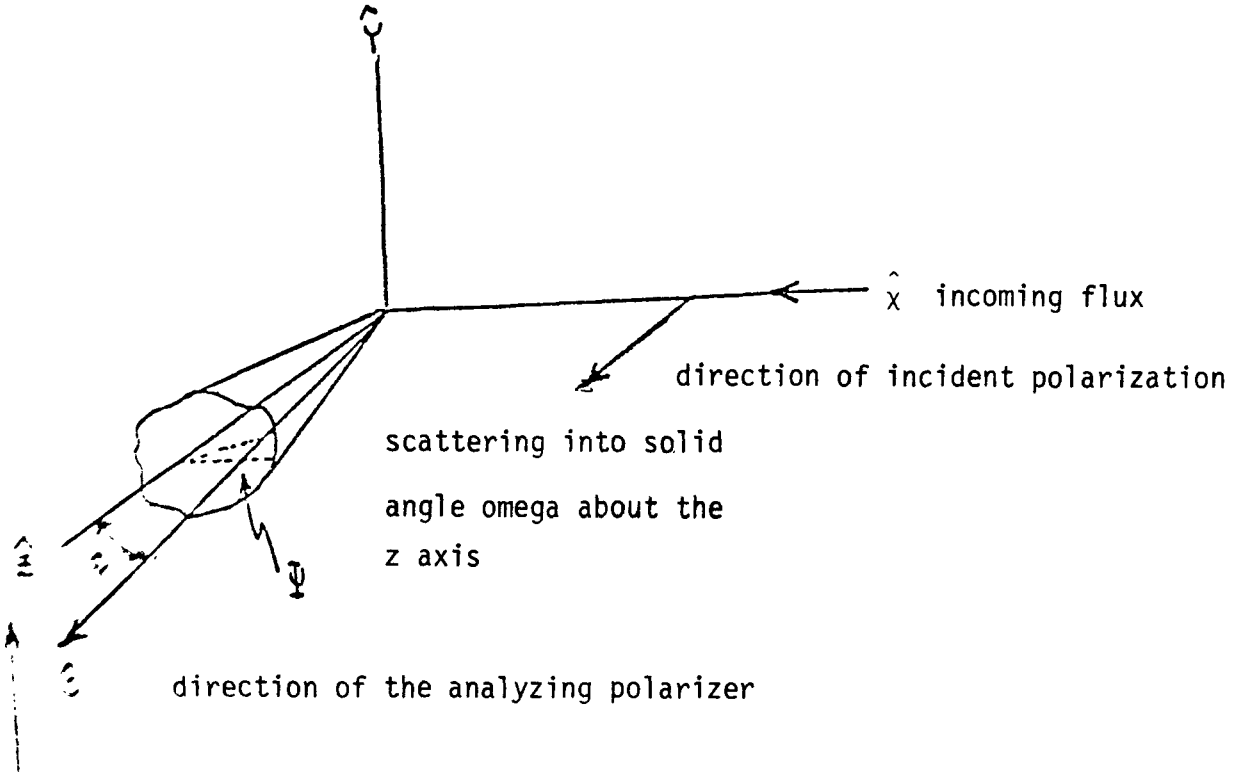

$\hat{s}$ direction of scattered light

θ angle between $\hat{s}$ and $\hat{z}$

Ψ rotation angle of $\hat{s}$ about $\hat{z}$ with $\Psi = 0$ placing $\hat{s}$ in the xz plane.

From the geometry for the polarization selected

$$\cos \theta = \sin \Psi \quad \sin \Phi \tag{4.20}$$

and equation 4.19 becomes

$$I(\Psi,\Phi) = I(o,o)\ [\rho_o + (1-\rho_o)\sin^2\Phi \quad \sin^2\Psi]. \tag{4.21}$$

Collecting the scattered radiation over a solid angle Ω yields for the total intensity of light leaving the beam splitter cube

$$I(o,o)\int[\rho_o + (1-\rho_o)\sin^2\Phi \quad \sin^2\Psi]\ d\Omega.$$

For the experimental geometry used here with an f/4 lens, this reduces to

$$I_{Ram}(o,o)\ [3.7\times10^{-2}]$$

using $\rho_o = 3/4$ for rotational Raman. Equating this with equation 4.18 yields

$$3.7\times10^{-2}\ I_{Ram}(o,o) = \frac{1+R}{2R}\ \delta x 2 \quad Hz. \tag{4.22}$$

(b) A similar expression for the intensity of the Rayleigh scattered light leaving the polarization beam splitter can be written using $\rho_{Ray} = 1.27\times10^{-4}$

$$I_{Ray}\ (o,o)\ [1.98x10^{-4}]. \qquad (4.23)$$

The intensity of the Rayleigh peak without rejection, but with the rejection interferometer in position was 30 kHz. A factor C^{-1} (see chapter 5) is lost at the rejection interferometer when the Rayleigh line lies between rejection peaks, and so the intensity of the Rayleigh line leaving the beam splitter cube is

$$\frac{C}{C-1}\ \delta\ 30\ kHz. \qquad (4.24)$$

Equating this with equation 4.23 yields

$$\frac{C}{C-1}\ \delta\ 30\ kHz = I_{Ray}\ (o,o)\ [1.98x10^{-4}].$$

Taking the ratio of this with equation 4.22 gives

$$\sigma_{Ram}(o) = \sigma_{Ray}(o)\ \frac{1+R}{2R}\ \frac{C-1}{C}\ \frac{2\ Hz}{30\ kHz}\ \frac{1.98x10^{-4}}{3.7x10^{-2}} \qquad (4.25)$$

where $\sigma_{Ram}(o)$ and $\sigma_{Ray}\ (o)$ are differential cross-sections for Raman and Rayleigh scattering respectively, when the scattered and incident polarization vectors are parallel. Using R = 0.4 for this experiment gives

$$\sigma_{Ram}(o) = \sigma_{Ray}\ (o)\ [5.2x10^{-7}].$$

The uncertainty in the measured B value (table 4.1) gives rise to plate spacing error of $\sim$ 0.2 orders while the uncertainty due to shifts, because of distortion effects will be on the order of 2-3 orders as was measured for the 4B and 8B resonances of CO_2.

(An estimated correction of 5-6 orders has been applied for distortion effects using the D value given in table 4.1). Because of this, uncertainty in the peak position coupled with the narrow width of the transmitted interferogram, a factor 0.25 will be allowed for intensity loss due to possible plate spacing errors.

The results of Chapter 5, and calibration measurements, give confidence that the calculations involving light loss at the rejection FPI and fluxes scattered into the collecting solid angle are good to a factor 2. The final estimate therefore, for an upper limit to pure rotational Raman scattering in CH_4 is

$$\sigma_{Ram}(o) < 4.2 \times 10^{-6} \sigma_{Ray}(o)$$

where the cross-sections are as previously defined.

References

1. G. Placzek, The Rayleigh and Raman Scattering (translated from Handbunch der Radiologie, Leipzeig, UCRL Trans. No. 526 (U. 1959).

2. G. Hertzberg, Infrared and Raman Spectra of Polyatomic Molecules, (Van Nostrand Reinhold, New York, 1945) p. 14.

3. Ibid., p. 20.

4. (a) Ibid., p. 396.

   (b) Alfons Weber, Sergio P.S. Posto, Leonard E. Chessman, and Joseph J. Barrett, J.O.S.A. 57, 19 (1967).

   (c) C.M. Penney, R.L. St. Peters, and M. Lapp, J.O.S.A. 64, 712 (1974).

   (d) C.M. Penney, J.O.S.A. 59, 34 (1969).

   (e) J.J. Barrett and Alfons Weber, J.O.S.A. 60, 70 (1970).

5. (a) G. Hertzberg, Spectra of Diatomic Molecules, (Van Nostrand Reinhold, New York, 1950).

   (b) R.J. Butches, D.V. Willetts, and W.J. Jones, Proc. Roy. Soc. London, A 324, 231 (1971).

   (c) reference 4b, 4c.

6. References 4b, 4c, 5a, 5b, 7.

7. Ralph R. Rudder and David R. Bach, J.O.S.A. 58, 1260 (1968).

8. A. Rosenberg, I. Ozier, and A.K. Kudian, J. Chem. Phys. (Lett. Ed.) 27, 568 (1973)

9. Richard T. Hall and Jerome M. Dowling, J. Chem. Phys. 45, 1899 (1966).

10. G. Placzek and E. Teller, Z. Physik 81, 209 (1933).

11. Reference 5, p. 121.

12. C.M. Penney, R.L. St. Peters, and M. Lapp, J.O.S.A. 64, 712 (1974).

13. Reference 2, chapter 1.

14. P.J. Hargis, Jr. and R.A. Hill, J.O.S.A 65, 219 (1975).

15. J.R. Sandercock, New Experimental Methods, p. 9, R.C.A. Laboratories, Zurich, Switerland.

16. W.H. Smith, private communication.

SECTION 5

FABRY-PEROT INTERFEROMETERS IN REFLECTION

5.1 The Feasibility of a Single Passed Fabry-Perot Interferometer as a Remote Pollution Monitor

In a remote detection scheme using the rotational Raman effect, the backscattered Raman light from a laser directed onto the plume of a smoke-stack is collected by a telescope and analyzed for impurities in the effluent. (See the review article by Kildal[1] for a description of the various remote detection proposals). The Fabry-Perot constitutes the analyzing part of the scheme and is set at a resonance pattern for the pollutant molecule under study. A large number of pollutant gases have Raman spectra that are periodic or near periodic and are thus capable of being multiplexed by the Fabry-Perot. Smith[2] has pointed out that for certain J values even asymmetric rotors will approach a prolate or oblate form having a near periodic spectrum. Smith[3] has also argued that the use of multiplexed rotational Raman instead of vibrational Raman, gives an increase in sensitivity of several thousands as a result of the increased cross-section, the greater entendue of the Fabry-Perot over a slit spectrograph, and the effect of multiplexing the rotational Raman spectrum.

Consider first the simplified case of a two component mixture, with CO_2 an impurity against an N_2 background. If impurities to concentrations of 100 ppm are to be detectable using a multiplexed interferometer, the Fabry-Perot must have a contrast of 10,000 in its ability to reject a background

rotational Raman line for a signal to noise ratio of unity to be achieved. Coincidences between some of the N_2 lines and the FPI fringes set to pass CO_2 (illustrated in table 5.1 below) make this difficult to obtain in a straightforward manner.

Table 5.1. COINCIDENCES BETWEEN N_2 RAMAN LINES AND CO_2

N_2 J Value	Coincidence with FPI Fringe to within_____cm^{-1}
18,19	0.025 cm^{-1}
8,20	0.150 cm^{-1}
7,9,10	0.275 cm^{-1}

Even with a single moded laser, atmospheric pressure broadening will give line widths of 0.05-0.1 cm^{-1}. This combined with the fact that the FPI fringes are Lorentzian with broad wings, implies that the transmission of N_2 Raman will be high. If the reflectivity of the etalons is increased to give finesse and a narrower Fabry-Perot linewidth in the hope of avoiding a coincidence, the transmission of the CO_2 rotational Raman scattering will fall drastically.

Calculations involving the multiplexing of CO_2 and N_2 spectra through a FPI indicate that concentrations of CO_2 on the order of 1-2% are the lowest that one can hope to observe under the conditions of a remote field measurement. These calculations are confirmed by laboratory experimental data taken on gas mixtures having high concentrations of CO_2 and then extrapolating to much lower percentages. The results are presented in figure 5.1 with the numbers against the curves giving the ratio of nitrogen to carbon dioxide by volume. The double peaks between the Rayleigh lines are due to the Raman scattering from CO_2 and N_2. At the higher CO_2 concentrations, the peaks

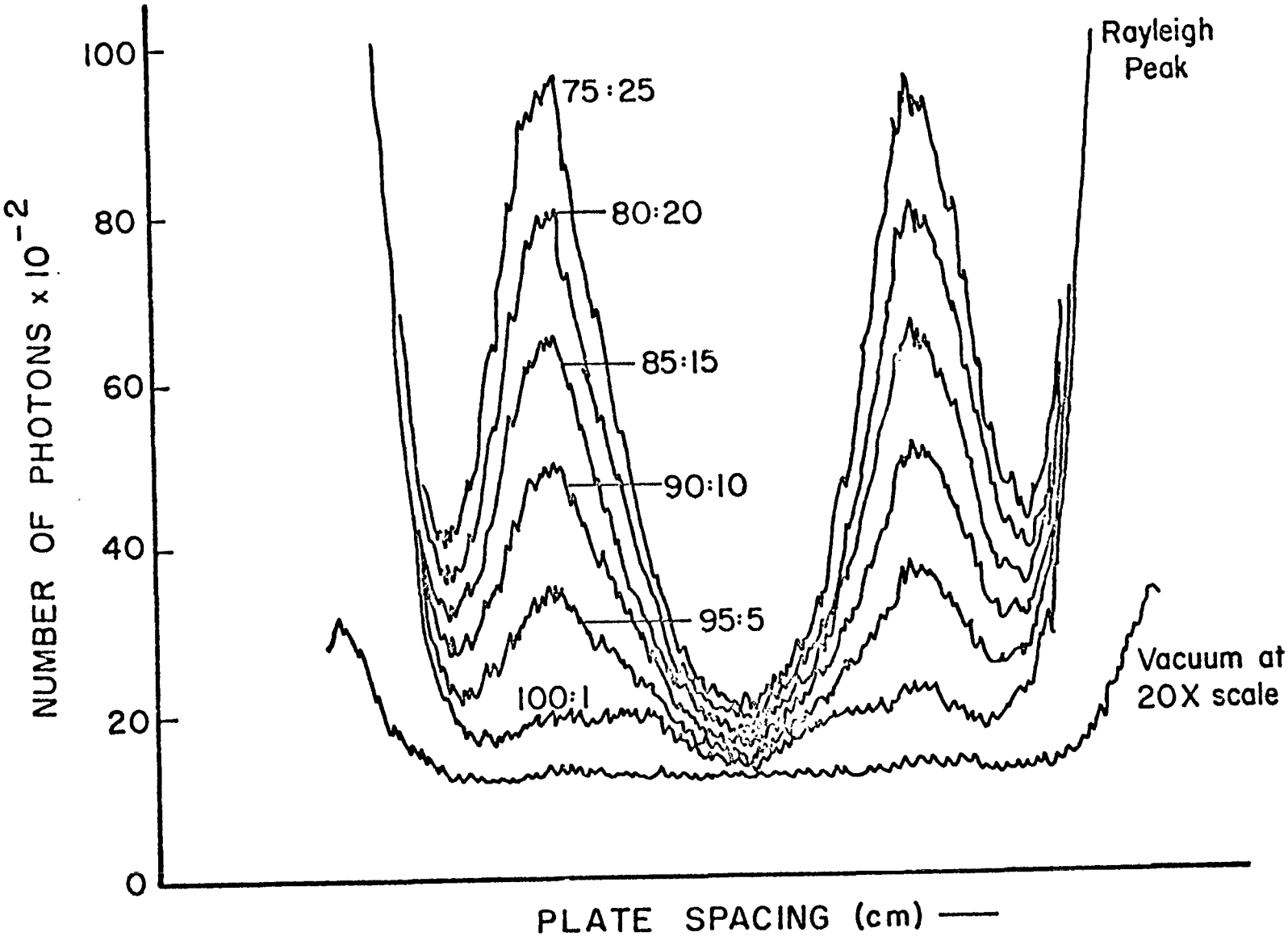

Figure 5.1. Mixtures of CO_2 and nitrogen.

can be seen to decrease in proportion to the decreased percentage of CO_2, indicating that the scattering is due mainly to CO_2 Raman. At the lower concentrations, however, the scattering is due mainly to N_2 and without subtraction of the N_2 Raman, the CO_2 peaks are difficult to observe. Chopping against the N_2 background should permit the detection of CO_2 down to a fraction of a percent, but this will be difficult in a remote measurement where one cannot be certain that the concentration of N_2 in smokestack plume will be the same as that in the nearby region used as a background reference. Double passing was attempted with no significant improvement. A factor 10 or so better could probably be obtained with extended integration times and a single moded laser not having the broad line width of the laser available for these experiments, but a field measurement would still be extremely difficult. To overcome these difficulties, a prefilter must be inserted to remove the background Raman and Rayleigh scattered light. One method of doing so is presented in the following section, and a second proposed in Chapter 6.

5.2 The Fabry-Perot as a Rejection Filter

For the remote detection of atmospheric pollutants with multiplexed Fabry-Perot interferometers it will be necessary to prefilter and remove contaminating light from three major sources:

(1) Rayleigh and Mie scattering

(2) N_2 rotational Raman

(3) O_2 rotational Raman.

Other molecular contaminating species will have concentrations on the order of the pollutant to be detected and their contribution will be reduced by the comb of the analyzing FPI, or will have their lines in know positions

(such as CO_2) and can be calibrated out in part, or if necessary, prefiltered as are N_2 and O_2 with another rejection filter.

The following discussion will show that a method of using FPI's in reflection can provide the necessary prefiltering action with the pure rotational Raman spectrum of N_2 used as the spectrum to be rejected for two reasons. Firstly, N_2 comprises 80% of the atmosphere and its rotational Raman scattering must be removed in any scheme of remote detection using the multiplexed rotational Raman effect. Secondly - as will be shown in a later section - the ability to reject light by this method is a strong function of the line width of the line to be rejected divided by the fsr of the rejection FPI. This ratio is more favorable for N_2 than for O_2 because of its larger B value. This will not prove a fundamental limitation in a situation where a single moded laser can be used to narrow the lines until the limit of pressure broadening is reached, and sample scans done with O_2 even under the poor conditions of broad line width and small free spectral range indicate that the method is applicable.

The reflected spectrum of the Fabry-Perot interferometer is the compliment of the transmitted spectrum (neglecting absorption losses; $a \sim 0.05$). Calculations indicate that if the Raman light from two distinct molecular species is incident upon the FPI, it is possible to transmit the light from one while reflecting nearly all the light from the second. To this end, etalons of low reflectivity and high surface quality are required. With the interferometer set to the periodicity corresponding to one of the molecules, the transmission of light from the other is slowly increasing with reflectivity while the transmission of the component in resonance with the FPI periodicity increases much more rapidly. Experiments show that the rejection of the

unwanted component can be as large as 135 with the non-resonant light suffering a loss of approximately 40%. Rayleigh and Mie scattering can be rejected in the same fashion as the Raman except there are no considerations as to the periodicity of the spectrum.

The experimental configuration is diagrammed in figure 5.2 with the Raman scattering derived from the same intracavity gas cell used for the single and double passed interferometers, collimated by the collecting lens, and directed to a polarization beam splitter. One polarization component was lost while the other was converted to circular polarization by the $\lambda/4$ plate before entering the rejection Fabry-Perot. This Fabry-Perot was set to pass either a Rayleigh fringe or the Raman light from a specific molecule such as N_2. The remainder of the incident spectrum was reflected back through the $\lambda/4$ plate which restored the light to linear polarization, but with the plane of polarization rotated by 90° so that it now passed through the polarization beam splitter to enter the analyzing Fabry-Perot interferometer where the impurity CO_2 was detected. The remainder of the system is the same as for the other FPI configurations.

5.3 Optimizing the Rejection Mechanism

Several factors must be considered in order to achieve a good rejection of unwanted light.

(1) Optical components should be of laser quality material with good scratch and dig ratings, few bulk scattering centers, good anti-reflection coatings, and in case of the etalons, wedged to eliminate first surface scattering.

(2) Effects due to misalignment and surface figure of the Fabry-Perot etalons in the rejection interferometer are critical and have been estimated using the formulae[4]:

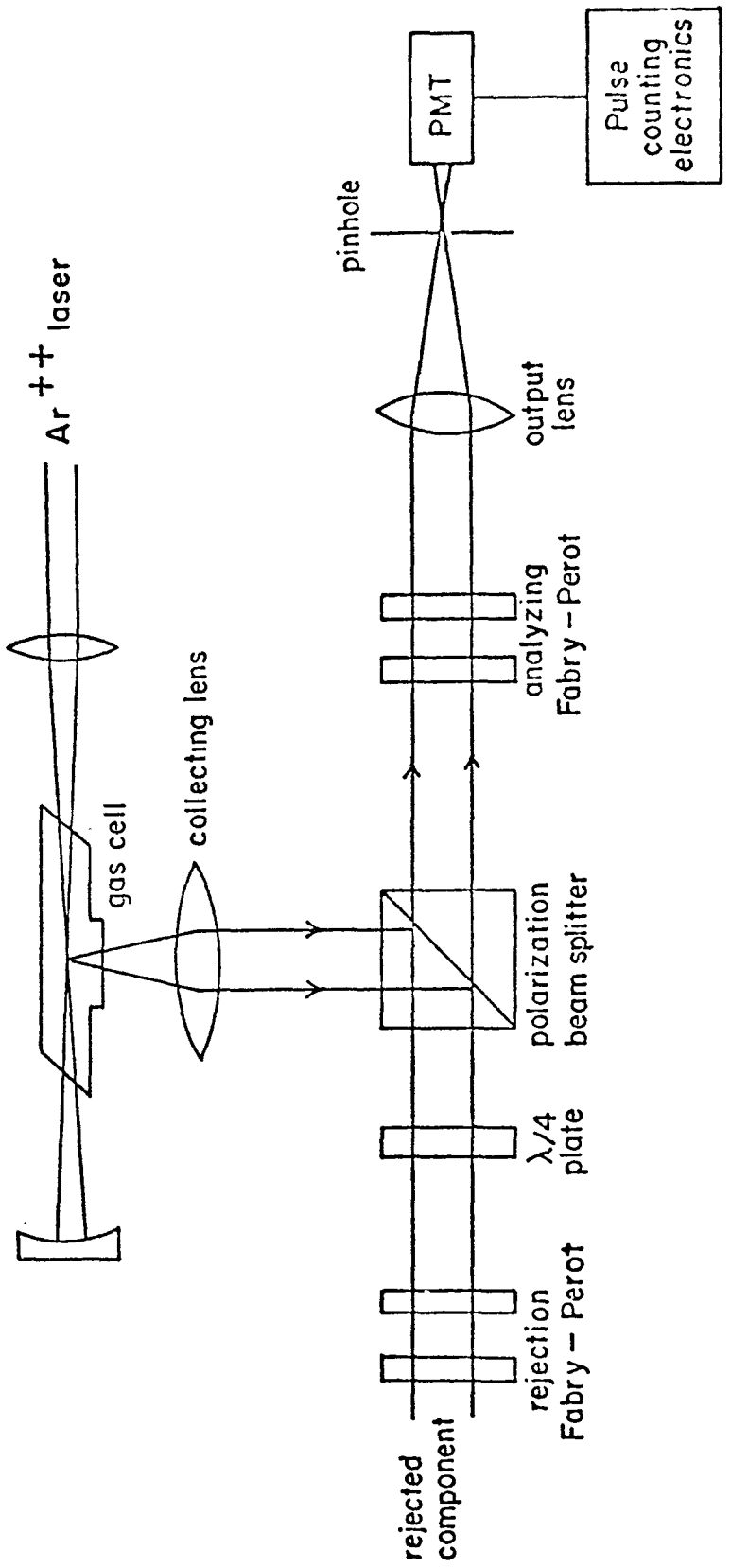

Figure 5.2. The rejection apparatus.

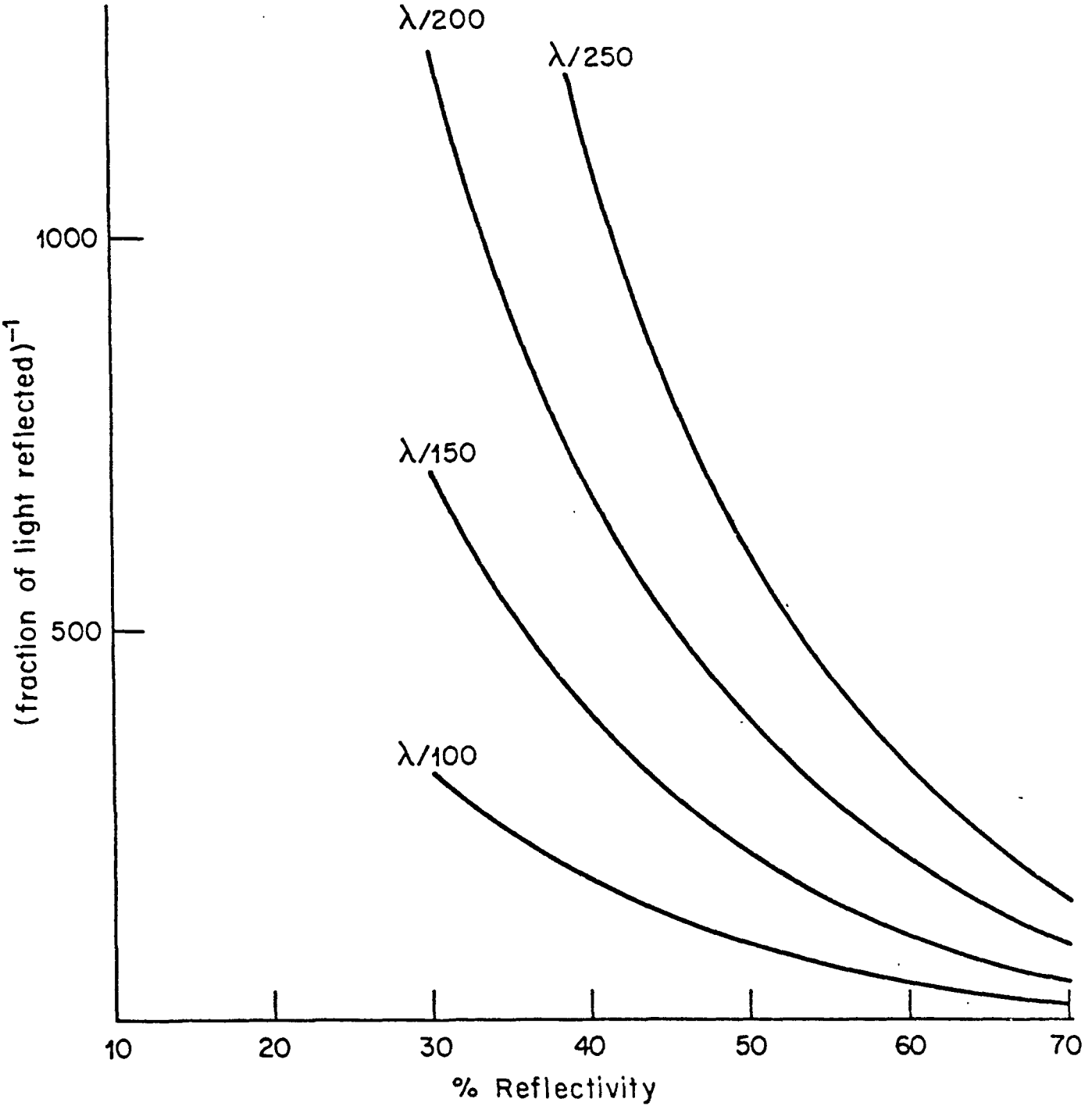

Figure 5.3. Fraction of reflected light vs. degree of alignment.

$$I/I_o = \frac{1}{(1+F)^{1/2}} \left\{ \arctan \left[(1+F)^{1/2} \tan \frac{1}{2} (\Phi+\Delta\Phi) \right] - \arctan \left[(1+F)^{1/2} \tan \frac{1}{2} (\Phi-\Delta\Phi) \right] \right\} \quad (5.1)$$

where

I/I_o is the ratio of transmitted to incident light

$\Phi, \Delta\Phi$ the phase and change in phase across the etalon due to misalignment

F is $4R/(1-R)^2$.

Figure 5.3 shows the fraction of radiation reflected for a given reflectivity and degree of misalignment with the phase converted to a distance expressed as λ/n using the relation $\Delta\Phi = 4\pi k \Delta t = 4\pi k(\lambda/n)$. The fraction of reflected light increases rapidly with misalignment at the higher reflectivities.

The effects due to finite line width and surface imperfections (both assumed to be Gaussian for the sake of an estimate)

$$I/I_o = \frac{1-R}{1+R} \left\{ 1 + 2 \sum_{p=1}^{\infty} R^p \cos k\theta \exp(-P^2/4\gamma^2) \right\} \quad (5.2)$$

where I/I_o, R, and θ are as above, and

$\gamma = \frac{\sqrt{2}\, n}{4\pi}$ for a Gaussian distribution of surface error with standard deviation $\sigma = \lambda/n$

$\gamma = \left(\frac{fsr}{\sigma}\right) \frac{1}{2\sqrt{2}\,\pi}$ for a Gaussian line incident with standard deviation σ

Figure 5.4 shows a plot of the fraction of radiation reflected for a given reflectivity R and ratio γ where

γ	incident line half width at fsr = 8 cm^{-1}	λ/n for surface defects
9	0.1 cm^{-1}	n = 80
12	0.075	107
18	0.05	160
25	0.036	225

Again the reflected intensity increases rapidly for increasing values of γ and R (increasing linewidth, surface defects, and reflectivity, for a fixed free spectral range).

The way to increase transmission of the unwanted light is to decrease the reflectivity of the etalons. Since the amount of CO_2 Raman lost will also increase, the reflectivity cannot be made arbitrarily small. If the assumption is made that the CO_2 lines fall at random on the N_2 rejection comb, the fractional loss of CO_2 Raman will be proportional to the area under one order of the Airy function.

$$CO_2 \text{ loss} \approx \frac{1-R}{1+R} . \qquad (5.3)$$

Some rough calculations using these ideas are outlined in table 5.2 below. The figures are only estimates because it is difficult to know what precisely is meant by the surface figure of an etalon, what the incident line shape will be, and how to account for imperfections in the multilayer dielectric coatings. The trends however are apparent.

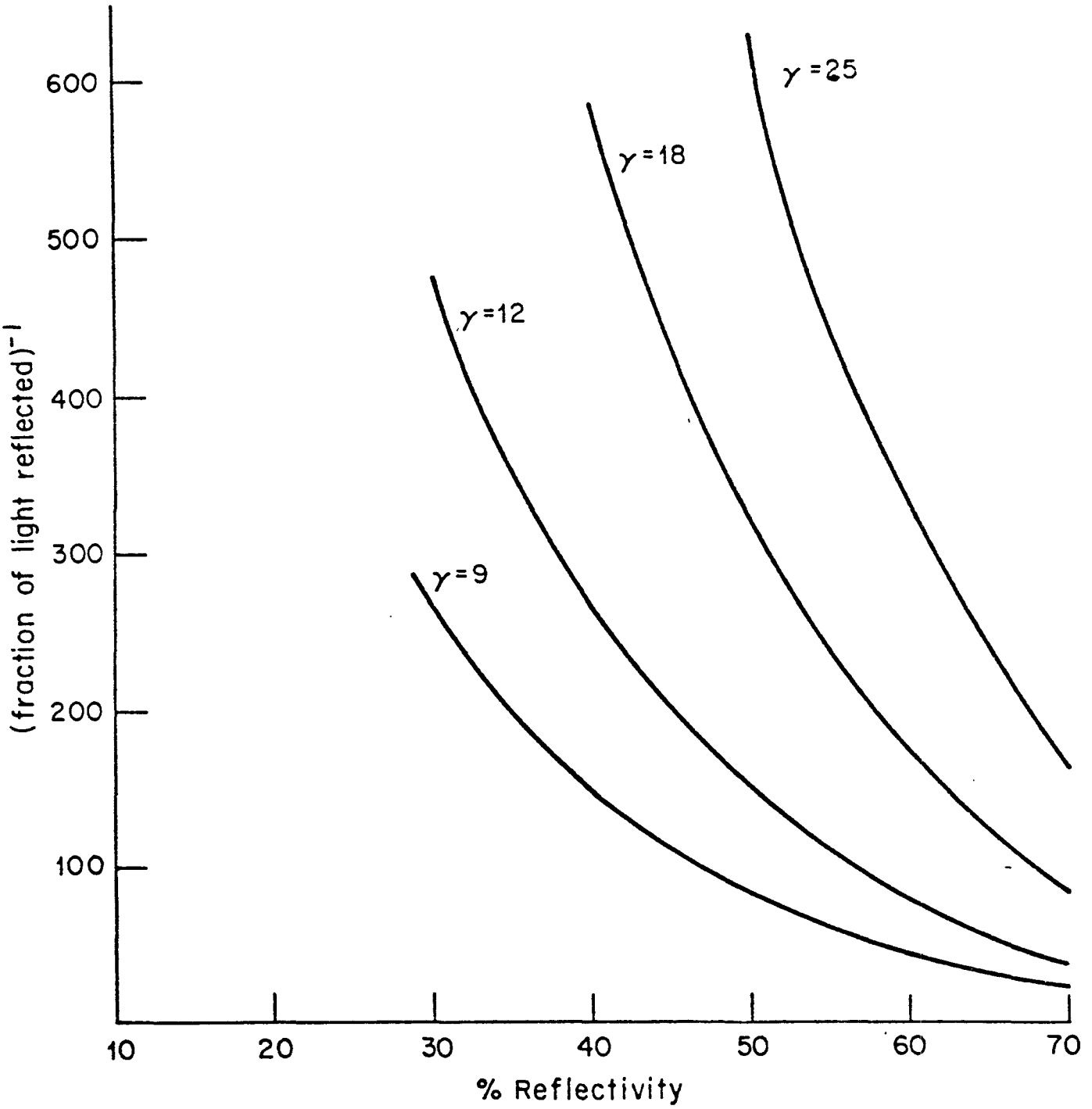

Figure 5.4. Fraction of reflected light versus etalon surface figure versus incident line width.

equation 4.2 and as a consequence will not perfectly match the comb of the rejection FPI (RFPI). This effect can be lessened for small R because the Fabry-Perot line widths become so broad as to accept the small shift in the N_2 lines.

The non-periodicity sets a limit to how closely the RFPI must be to resonance to behave as good rejection filter. Equation 4.9 yields.

$$\Delta t = - \frac{\Delta B}{8B^2} \tag{5.4}$$

A change in free spectral range of 4 ΔB will cause the J = 13 line to shift by 13 $(4\Delta B)cm^{-1}$. At the 4B resonance for N_2, the ratio of laser line width to fsr is $\sim$140 (ratio of incident to reflected intensity for the rejection Fabry-Perot) can be expected at this fsr and line width. A tolerance on the width of the rejection resonance can be estimated by requiring that the J = 13 line be shifted away from its optimum position by not more than half the incident line width or $\sim$ 0.1 cm^{-1}.

$$13(4\Delta B) \sim 0.1$$

For nitrogen with B $\sim$ 2 cm^{-1} this gives the severe limit of

$$|\Delta t| \sim 2\text{-}3 \text{ orders.}$$

The choice of J = 13 in the above can be justified by requiring that the shift in line position due to distortion effects also be no more than 0.1 cm^{-1} for some line J_{max}

$$8D\ (J_{max}+3/2)^3 \sim 0.1.$$

Using the D value for N_2 gives $J_{max} \sim 13$.

In practice the optimum rejection resonance is shifted to slightly smaller fsr's by distortion effects in exactly the same fashion as the CO_2 resonances were shifted in chapter 4, and a range of J values from J = 0 to approximately $J = 2J_{max}$ will be covered by the rejection comb when at this optimum position. The total intensity in the lines beyond J = 26 will be down by at least a factor 10^3 from the intensity in the region of the rejection comb and should not contribute significantly to the signal. Distortion effects, while deleterious and imposing limitations to the rejection ability, should not pose serious problems.

In summary therefore, the non-periodicity of the spectrum to be rejected will limit rejection ratios to the single line rejection ratio of ~140 for a line width of 0.25 cm^{-1} and the N_2 resonance fsr, the tolerance on the plate spacing to achieve the above ratio is $\pm$ 2 orders for N_2 (a worst case because of the large B value), and low reflectivity etalons of high surface quality are required with extreme care in alignment to be expected.

5.4.0 Experimental Data

A calibration scan of the apparatus diagrammed in figure 5.2 is given in figure 5.5 where the plate spacing of the RFPI is plotted against the reflected light for a single laser line incident and the analyzing Fabry-Perot interferometer (AFPI) removed. The rejection ratio (the ratio of the maximum to minimum light received by the detector) is

$$238 \pm 2.5\%$$

with the error primarily due to the $\sqrt{N}$ noise on the I_{min} measurement (for the curve shown in figure 5.5).

Since the Rayleigh and Raman scattered light will have line widths in excess of the laser line widths due to pressure broadening, the above ratios are an upper limit for the rejection in this system at this fsr (but not necessarily one, as mentioned previously, that has a single moded laser). Although requiring delicate alignment of the RFPI, the measurements were reproducible from day to day to within 10%. Because, the etalons had such a low reflectivity and finesse, the method of fractional orders could not be used to give an accurate measure of the plate spacings, but feeler guage measurements placed it on the order of a few thousandths of an inch.

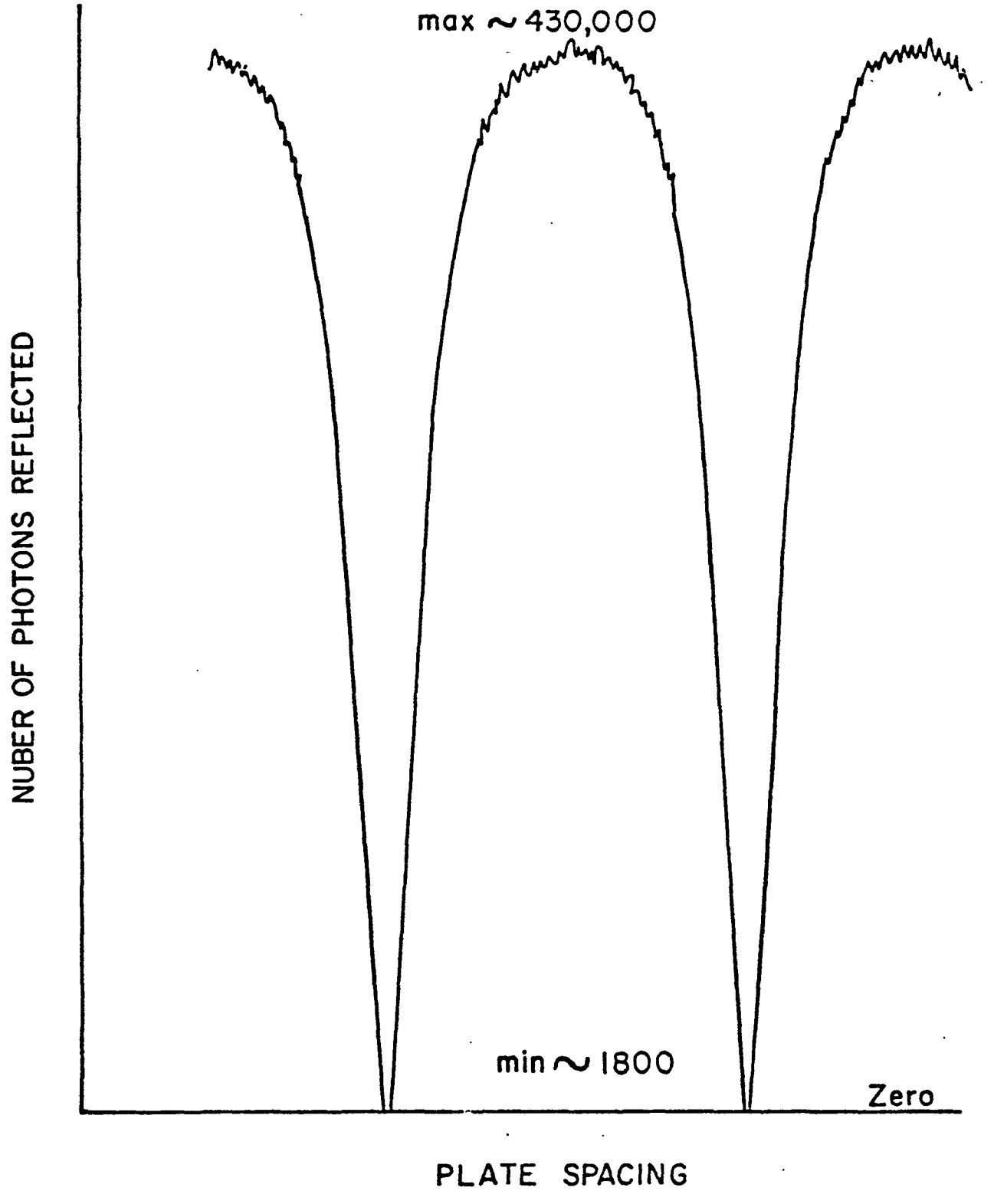

Figure 5.5. Calibration scan of FPI in reflection.

If the ratio of incident intensity upon the interferometer to the minimum intensity received by the detector is required, then the above rejection ratio must be multiplied by the correction factor.

$$\frac{C}{C-1}$$

C = contrast of this interferometer.

This takes account of the fact that due to the finite contrast of the rejection interferometer, the maximum of the curves given in figure 5.5 is slightly less than the intensity incident upon the interferometer.

At the large fsr ($>50cm^{-1}$) used for this measurement, the rejection ratio is limited by surface figure and alignment and not by line width considerations. From figures 5.3 and 5.4, the limiting ratio expected is on the order of 300-400 assuming $\lambda/200$ across the aperture. The measured value corrected for the contrast of the FPI was 290. The disagreement is not unreasonable considering the number of unknowns involved, and reflects the expeceted variation in parameters from etalon to etalon or with type and degree of complexity of surface coatings and figure.

5.4.1 Rejection of Rayleigh Scattered Light

A test was made of the ability of the apparatus to remove Rayleigh light in the presence of CO_2 Raman. To this end the AFPI was set to the carbon dioxide 8B resonance while the RFPI was given a small plate spacing to maximize its free spectral range. The respective free spectral ranges did not divide evenly.

Figure 5.6a shows a scan of the AFPI with the RFPI set so that the Rayleigh line fell between the rejection fringes. The peaks in the center are the CO_2 Raman. Figures 5.6b, c show scattering from the same gas cell sample (pure CO_2 at slightly over one atmosphere), but this time with the rejection FPI on a rejection fringe. Figure 5.6b has an essentially constant base line when viewed at the same scale as the previous scan without rejection, while figure 5.6c shows tiny Rayleigh peaks in the center as a result of a slight misalignment of the RFPI etalons. The integrated intensity of the CO_2 Raman in arbitrary units with and without the rejection FPI set to a rejection peak is the same, as should be expected (figure 5.6a 48 ± 5%; figure 5.6b 50 ± 5%). The Rayleigh rejection ration, or the ratio of the Rayleigh intensity to the base line noise or residual peak intensity after rejection, when multiplied by the correction factor C/C-1 is greater than 240. (Original graphs more easily read than the reproductions in figure 5.6, with the ratio probably underestimated by 30%). This ratio gives an upper limit to the expected Raman rejection ratio as the non-periodicity of the Raman spectrum due to distortion effects precludes its complete removal. That this ratio is smaller than the previous one using a laser line directly upon the Fabry-Perot is reasonable because of the increased line width upon scattering from the gas sample.

The same experiment was repeated with N_2 in the gas cell and both the rejection and analyzing Fabry-Perots near the N_2 4B resonance. Figure 5.7a shows the Rayleigh peaks on a 1x scale with the Raman suppressed while figure 5.7b the same sample with the Rayleigh light rejected. The scale is now 10x. From the areas under the curves, the Rayleigh rejection ratio is found

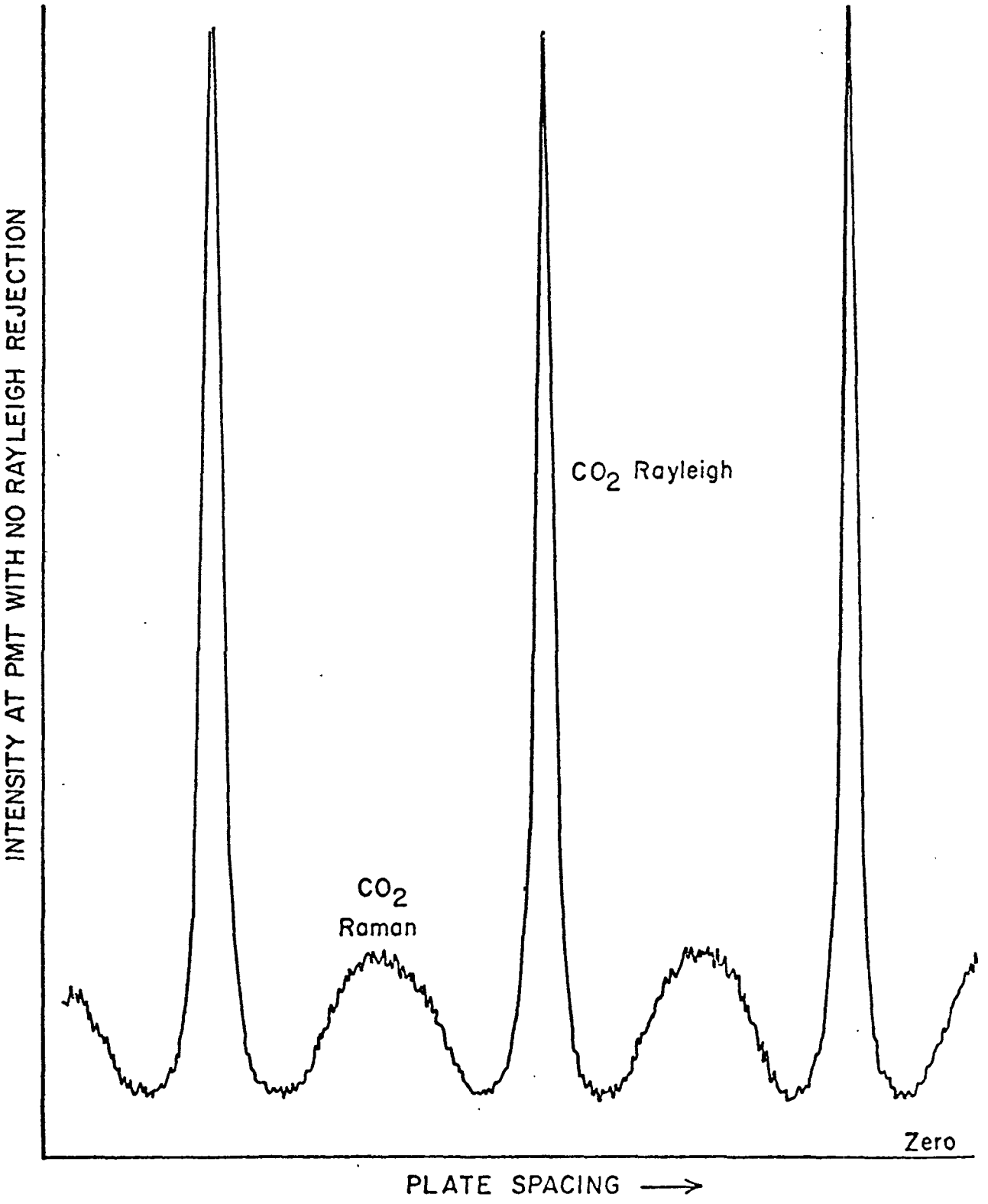

Figure 5.6a. Rejection of CO_2 Rayleigh light.

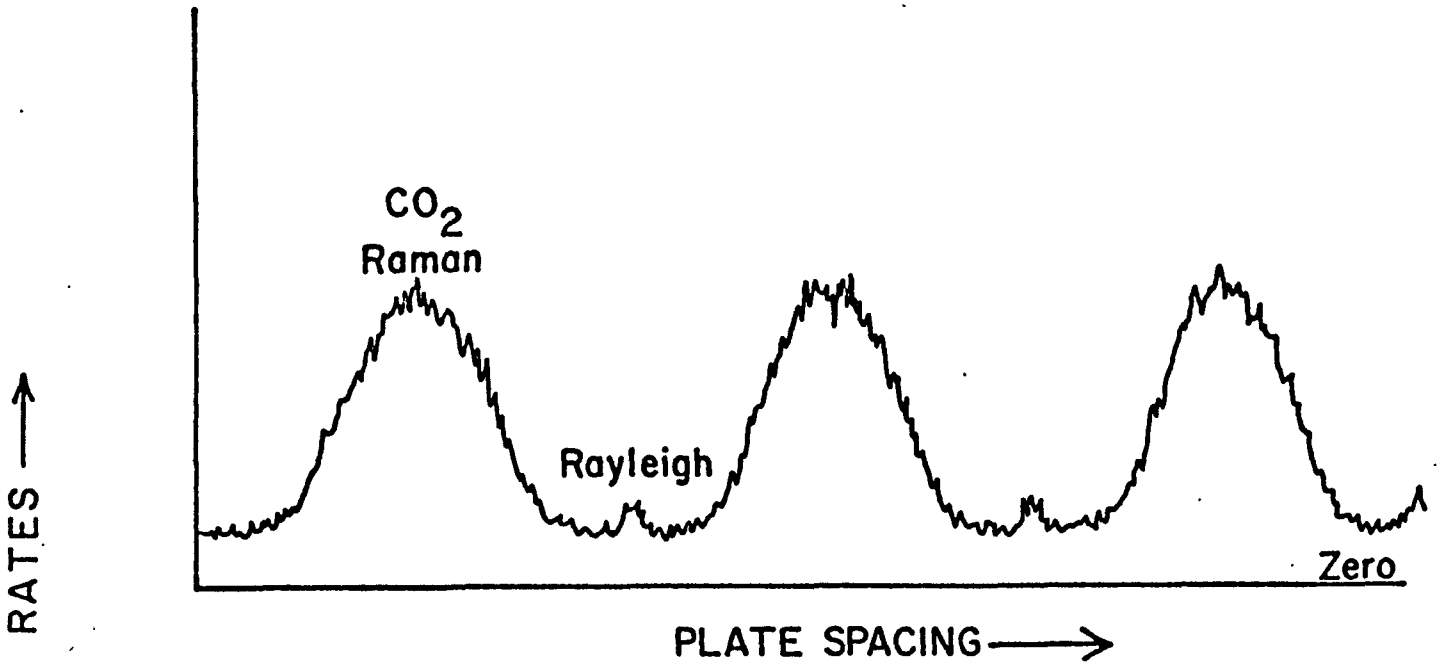

Figure 5.6b. Rejection of CO_2 Rayleigh light.

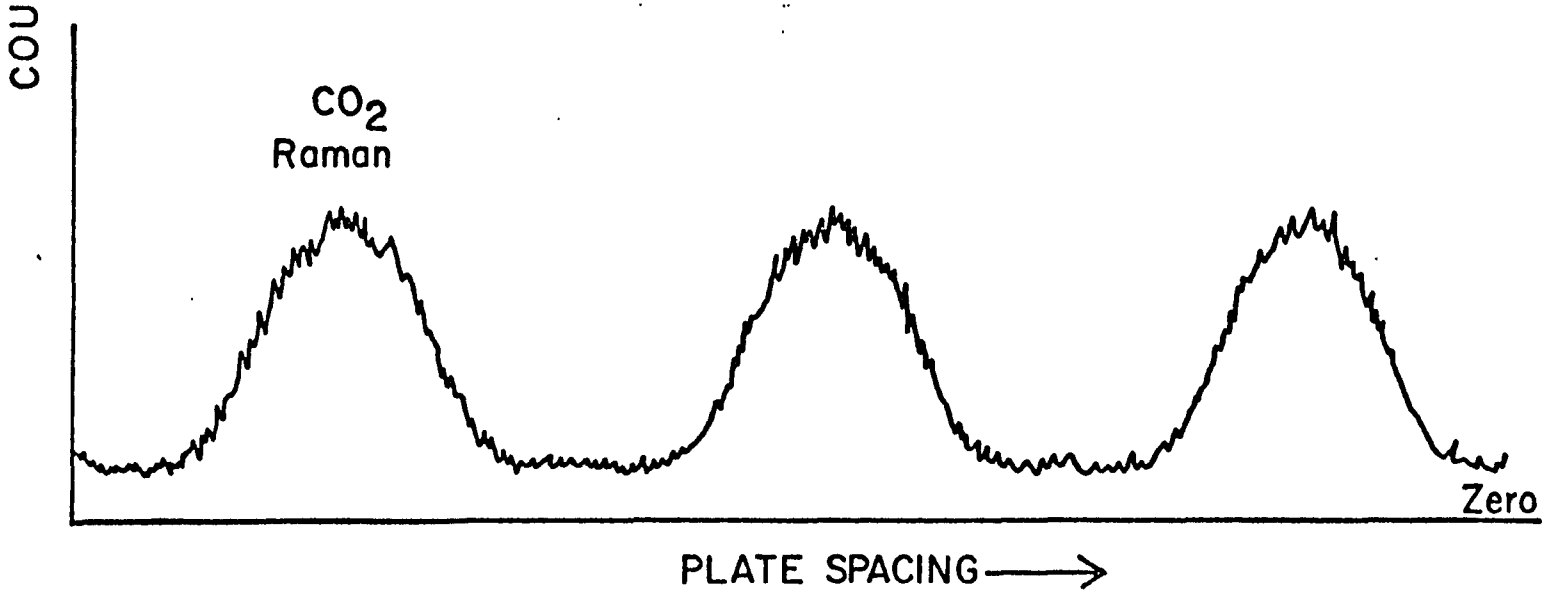

Figure 5.6c. Rejection of CO_2 Rayleigh light.

to be 125 ± 5% (expected value from table 5.1 is ∿ is 140). That this is lower than the measurement for CO_2 is reasonable because of the smaller free spectral range used in this measurement. It is difficult to say quantitatively whether the ratio has decreased in the proper fraction because of different line widths and shapes in each measurement as well as the problem in measuring the absolute free spectral range of the RFPI due to its low finesse.

5.4.2 Rejection of Raman Scattered Light

The rejection of Rayleigh light is not sufficient to enable the observation of low level impurities - the background Raman must also be eliminated. To test the effectiveness of the rejection scheme in removing N_2 Raman, both the rejection and analyzing Fabry-Perots were set at the N_2 4B resonance. The gas cell was filled with an atmosphere of pure N_2 and the follwoing scans performed.

figure 5.7a N_2 Raman rejected, scale 1x

figure 5.7b N_2 Rayleigh rejected, scale 10x

figure 5.8 N_2 Raman rejected, scale 2.5x.

A measurement of the areas under the curves gives a Raman rejection ratio of 135 ± 5%. The flat background was assumed to be Rayleigh scattering in the Lorentzian wings which would give a contrast of 160 to the AFPI. This is consistent with previous experiments.

Although the scans will not be shown here, other measurements of the Raman rejection ratio were made at plate spacings near to the one described above. The results are tabulated below.

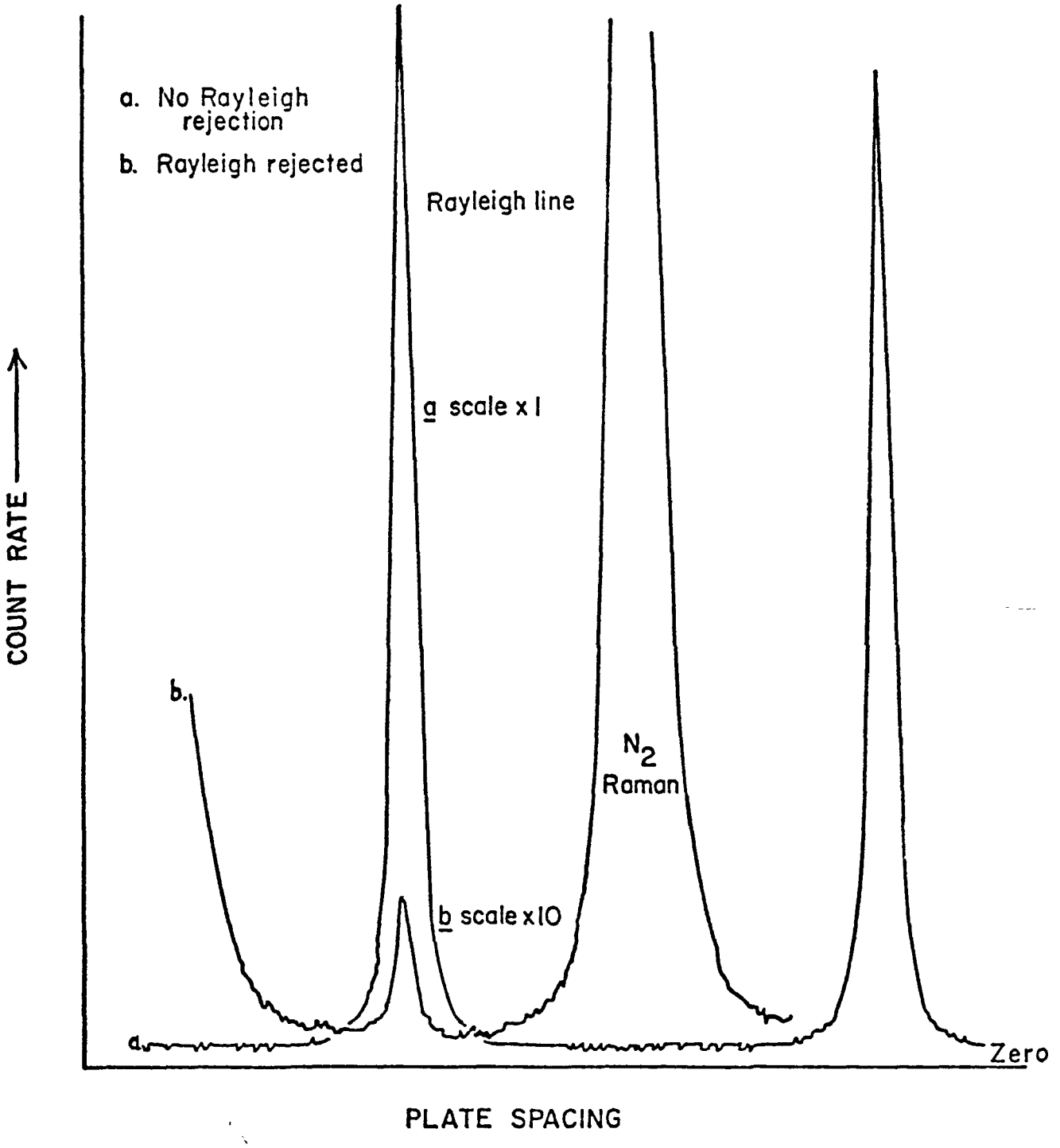

Figure 5.7. Illustration of Rayleigh rejection of N_2.

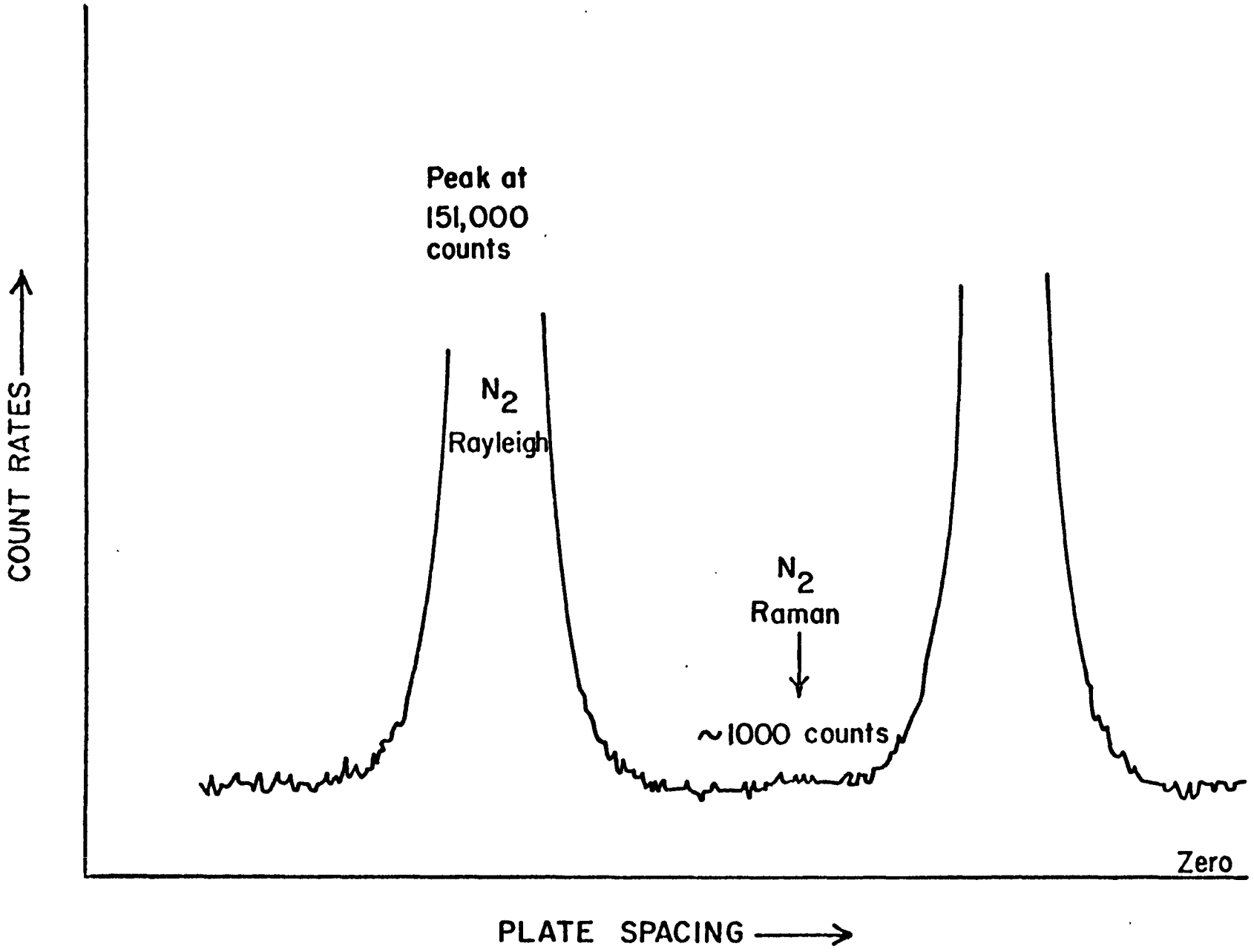

Figure 5.8. Rejection of N_2 Raman.

above measurement	ratio 135
spacing decreased by five orders	ratio 81
spacing further decreased by five orders	ratio 39

with similar results for increasing plate spacings. This rapid decrease in the rejection ratio is in agreement with the argument made in section 5.3 concerning the widths of rejection resonances. Because of the low finesse of the rejection FPI, a plate spacing determination was not possible and feeler guage measurements placed it as within the 4B resonance for N_2 by ± 1 thousandth of an inch. The optimum position was extremely difficult to locate initally as it had to be done by a trial and error method with no converging search algorithm.

5.4.3 Detection of Impurities in a N_2 Background

When used in the multiplexed mode, it is convenient to assign both a Rayleigh and Raman contrast to the Fabry-Perot. The Rayleigh contrast reflects the effectiveness of the interferometer in rejecting the light from a single line and goes as $C_{Ray} \sim \left(\frac{1+R}{1-R}\right)^2$ while the Raman contrast reflects the effectiveness of rotational Raman spectrum rejection. Since the Raman spectrum periodicities, it is approximated by $C_{Ram} \sim \frac{1+R}{1-R}$ (see Section 5.3). An expression for the expected level of pollutant detection possible using the RFPI and AFPI system can be written as follows:

$$\frac{\text{Background Intensity}}{\text{Signal Intensity}} = \frac{\left[\frac{I_{Ray}(N_2)}{R_{Ray}C_{Ray}}\right] + \left[\frac{I_{Ram}(N_2)}{R_{Ram}C_{Ram}}\right]}{S_R S_A I_{Ram}\,(\text{pollutant})} \qquad (5.5)$$

where

$I_{Ram}(N_2)$, $I_{Ray}(N_2)$, $I_{Ram}(\text{pollutant})$	are the intensities for N_2 and pollutant scattering at the 90^0 geometry calculated using equation 4.5
C_{Ram}	AFPI Raman contrast
C_{Ray}	AFPI Rayleigh contrast
R_{Ram}	RFPI Raman rejection ratio
R_{Ray}	RFPI Rayleigh rejection ratio
S_A	Signal transmission through the AFPI
$1-S_R$	Signal loss at the RFPI

An estimate of the parameter S_A using equation 2.7 for any particular fsr and incident line width will be too large because it is a singal line transmission efficiency and consequently neglects distortion effects tending to pull the lines off the transmission fringes of the AFPI comb. This added effect due to distortion can be found from the data in figures 5.6a,b,c by comparing the Raman intensity in the central peak to the total Raman intensity. The data is given below in arbitrary units.

Total Rayleigh intensity	860
Total Ram intensity	720
∿Peak Raman intensity	∿600

If the distortion constant were zero, all the Raman light would be concentrated into the central peak. Since it is not, the transmission of the signal through the AFPI as calculated using equation 2.7 must be decreased by $\sim$ (120/720) or $\sim$ 16% to account for Raman signal losses into the baseline. (S_A = 0.84 times S_A calculated from equation 2.7).

Using equation 4.5 to calculate the scattering intensity gives a Raman to Rayleigh intensity ratio of $\sim$ 0.96 when corrected for losses at the RFPI. The measured value from the above data is 0.84. Since the $\left(\frac{1-R}{1+R}\right)$ rule for light loss at the RFPI is only approximate, it is most likely that the discrepancy is caused by a small resonance between the RFPI comb and the CO_2 spectrum.

The Rayleigh contrast was measured using a laser line directly incident upon the RFPI (fsr set to CO_2 4B resonance) and found to be $\sim$ 300. This is consistent with the broad laser line width and small fsr.

Application of equation 5.5 using the measured values of R_{Ray} and R_{Ram} at a fsr corresponding to the N_2 4B resonance, an incident line width of 0.25 cm^{-1}, the above measurement of C_{Ray}, S_R from table 5.2 with R = 0.4 (and confirmed by experiment), the intensities calculated using equation 4.5, and the AFPI having etalons with R = 0.94, yields the following estimates for the fractional level of impurity detectable when the background intensity equals the signal intensity.

Gas Mixture	N_o N_2 Rayleigh Rejection N_2 Raman Rejection	Both Rayleigh and Raman Rejection
CO_2 in N_2	~1.3%	390 ppm
O_2 in N_2	~1.5%	450 ppm
O_2 in X_e		200 ppm

If the background intensity across the pollutant Raman peak to be detected has fluxuations due to $\sqrt{N}$ noise alone, rather than due both to $\sqrt{N}$ noise and fluxuations generated by the relative motion of the AFPI comb across the pollutant spectrum, then lower limits of detectability than those calculated above can be expected. This will be verified in the data presented. It is also clear that a laser line width narrower than the 0.25 cm^{-1} line width narrower than the 0.25 cm^{-1} line available here will lower the limits of detectability through two mechanisms. Firstly, the rejection FPI will achieve better rejection ratios (until the limit set by etalon defects is reached at a ratio of ~300-400), and secondly, the transmission S_A of the pollutant signal through the AFPI will be enhanced. Narrowing the line width from 0.25 cm^{-1} to 0.1 cm^{-1} should give an improvement of ~5-6 in detectability.

Because the parameters C_{Ray}, C_{Ram}, and S_A are all functions of the AFPI reflectivity, this reflectivity can be chosen to optimize the detectability limit calculated using equation 5.5 for the particular pollutant molecule to be detected and laser line width available.

Measurements were made on mixtures of CO_2 in N_2 and O_2 in N_2 with the N_2 Raman scattering being rejected by the RFPI. Since only one rejection interferometer was available, it was not possible to simultaneously remove both the Rayleigh and Raman background and consequently one additional

measurement was made using O_2 in Xe. With Xe having no Raman scattering and its effective cross-section (cross-section calculated for the experimental geometry used here taking depolarization ratios into account) approximately twice that of N_2, any impurity seen against Xe scattering could be seen against N_2 if the N_2 Raman were simultaneously removed.

In the following data, the quantity I_{Ram} (pollutant) in equation 5.5 was taken to be the area of the Raman peak resting on the baseline defined by background scattering. The quantity $I_{background}$ was taken to be the area of a section of background below the Raman peak whose width was equal to the width of the laser Rayleigh line. The Rayleigh rather than the Raman interferogram width was used because the latter has been broadened by distortion effects.

Figures 5.9a and 5.9b show scans taken with 10. ± 0.5 Torr of CO_2 and then with sufficient N_2 added to give 1.5% CO_2 in N_2. In each case, the interferogram was recorded with the rejection FPI in position so that corrections should not have had to have been made for signal losses at the rejection interferometer. The intensities of the two Raman peaks, did, however, differ by $\sim$ 25% (assuming the base line is predominatly background scattering) and this is a reflection upon the fact that the rejection interferometer fsr is close to an integer times that of the CO_2 fsr and as a consequence resonance effects can be expected. These effects were not as noticable for the CO_2 scans in figures 5.6a,b,c, where the two periodicities did not divide, and are not seen when N_2 is rejected and O_2 sought (again the periods do not divide).

The predicted CO_2 Raman to base intensity should be unity for $\sim$ 1.3% CO_2 in N_2 with only the N_2 Raman rejected. The measured value (corrected for the 25% loss due to resonance effects not considered in the calculation) is 0.71.

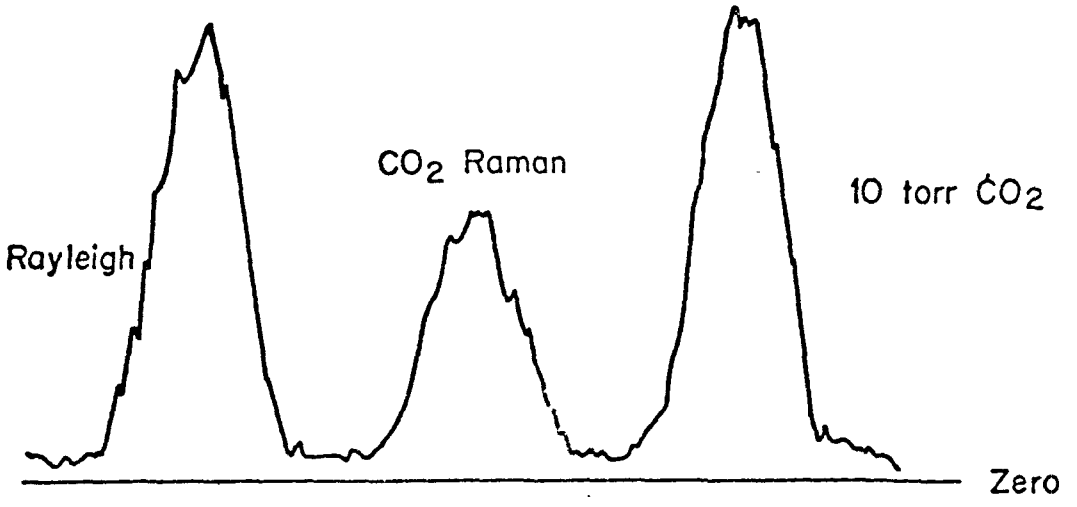

Figure 5.9a. CO_2 calibration.

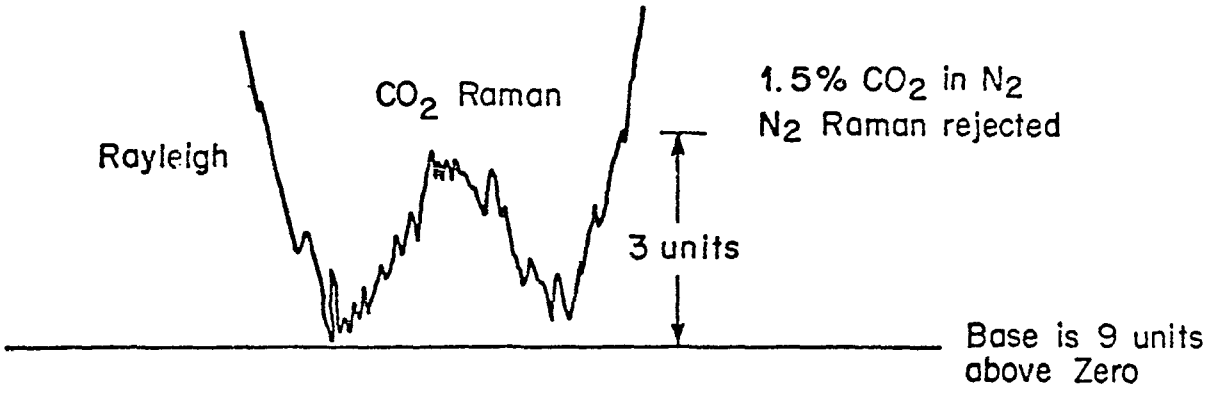

Figure 5.9b. N_2 Raman with and without rejection.

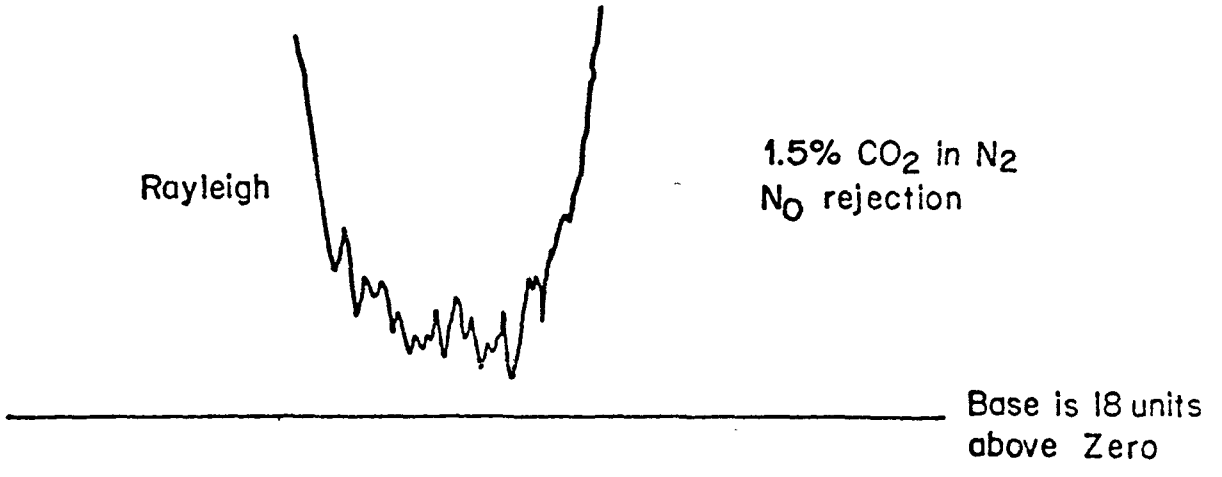

Figure 5.9c. 1.5% O_2 in N_2 with N_2 Raman rejection.

Base line fluctuations are ∿ 1/4 the Raman peak height and so signal to noise ratios of unity can be expected at the 0.4% level of CO_2 in N_2. With better statistics so that the Rayleigh background could be removed, it should be possible to see CO_2 in air at its normal concentrations.

O_2 in N_2

Figures 5.10a and 5.10b show scans taken with 10. ± .5 Torr of O_2 and then with sufficient N_2 added to give 1.5% O_2 in N_2, and as in the previous measurement, both interferograms were recorded with the RFPI in position. The intensity of the O_2 Raman peaks in each scan agrees to within 10% as is expected (assuming base line follows the curved slope of the Lorentzian wings). The predicted O_2 Raman to base intensity is unity for ∿ 1.5% O_2 in N_2 while the measured value is ∿ 1.3. Considering the number of variables involved, the agreement is probably fortuitous. Figure 5.10c shows 760 mm of N_2 with no Raman rejection at the O_2 resonance (scale is 1/5 that of figure 5.10a,b). Clearly without Raman rejection, the O_2 peak would be not at all visible. The base line fluctuations in figure 5.10b are ∿ 1/5 of the O_2 intensity, and so concentrations of ∿.3% O_2 in N_2 will give signal to noise ratios unity.

Because the O_2 4B fsr is ∿3.5 times as large as that for CO_2, the effects of laser line width are diminished. This is seen both in the sharpness of the O_2 as compared with the CO_2 Raman peak, as well as the more rapid attenuation of the Rayleigh fringe away from its peak position.

5.5.5 O_2 i Xe

Figures 5.11a and 5.11b show .7% in Xe without and with Raman rejection. The intensity in the Raman peak divided by the background intensity

---

†Rayleigh

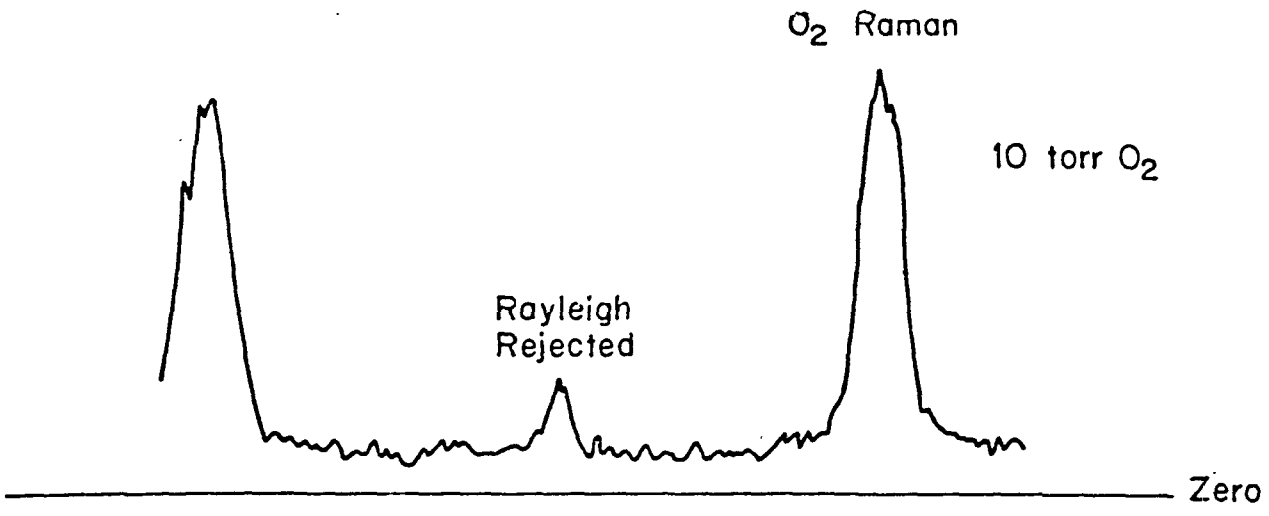

Figure 5.10a. O_2 Calibration.

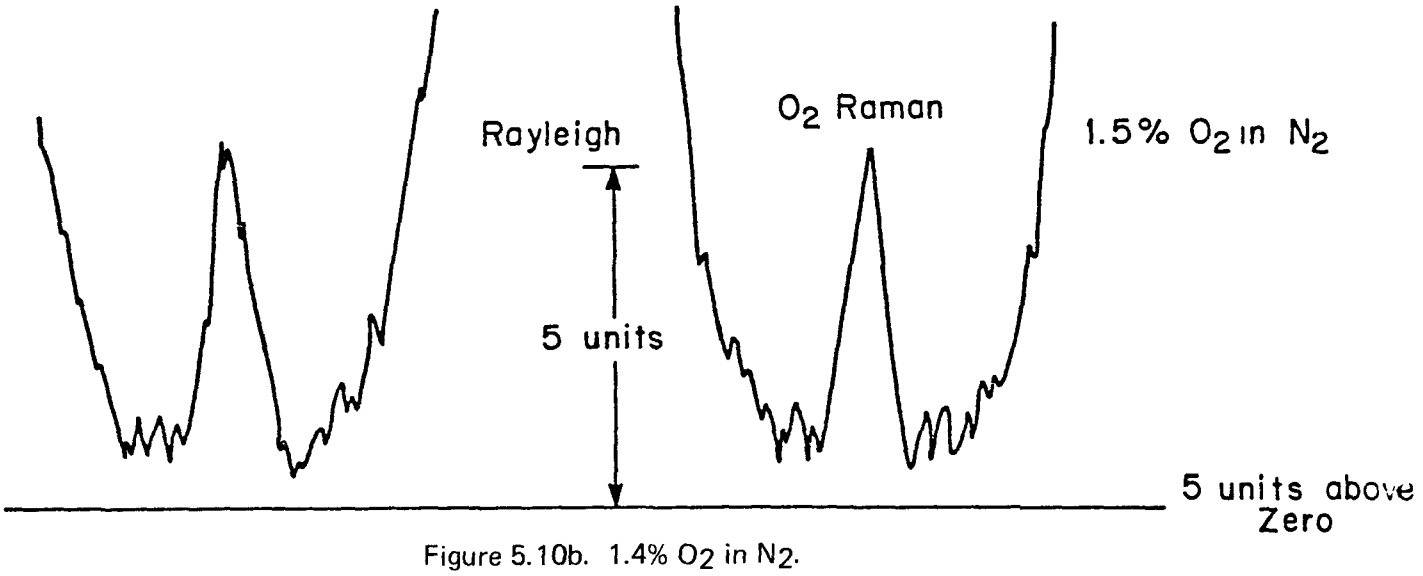

Figure 5.10b. 1.4% O_2 in N_2.

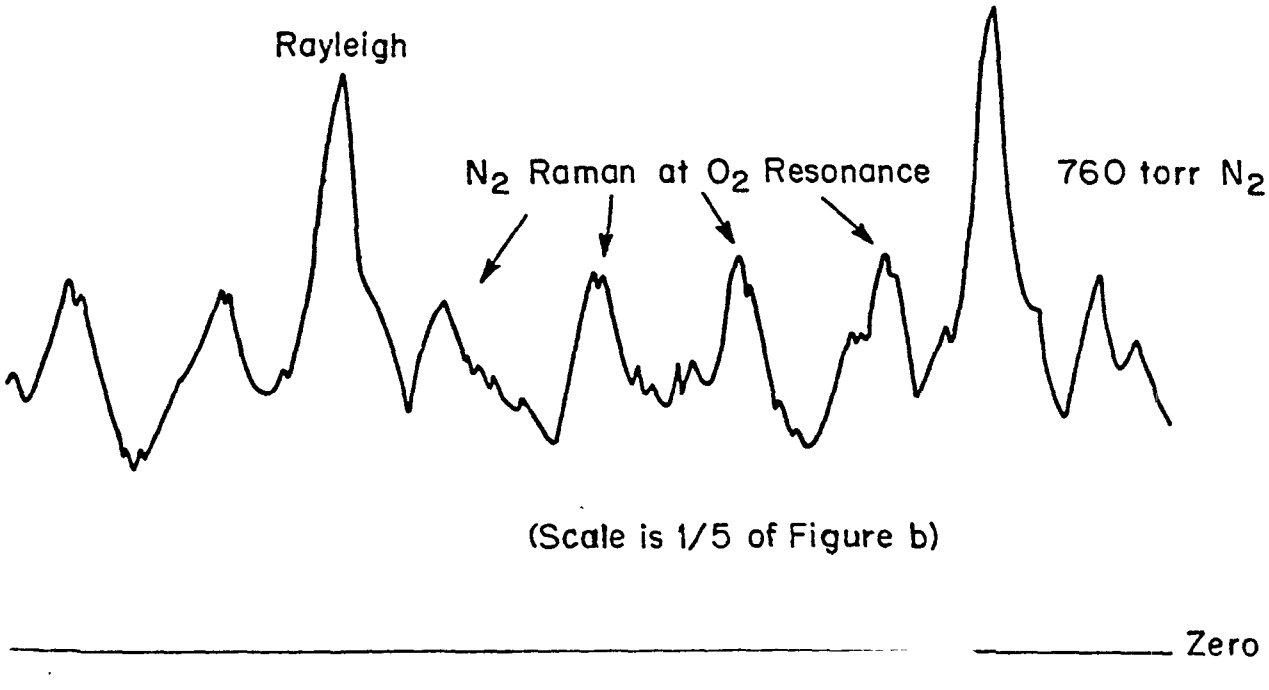

Figure 5.10c. 760 Torr N_2.

integrated over a wavelength range comparable to the laser line width is $\sim$ 5/3 which is in contradiction to the prediction of a ratio near unity for concentrations of $\sim$.02%.

When the rejection ratio[+] for Xe was measured by integration over the area of a Rayleigh fringe with and without rejection, the value was found to be in excess of 100 and should have been quite sufficient to give the expected level of detection. However, when the same ratio was measured using areas near the center of an order the ratio was found to be only $\sim$8. The background light here could not have been normal incident Rayleigh (and the collimation was sufficiently good as to exclude oblique Rayleigh also), was not dark counts or light leaking into the PMT, and was not O_2 Raman spread into the baseline. The likely explanation is impurity Raman scattering because of a bad sample of Xe. If this value 8 is used for the rejection ratio, then the predicted level rises to 0.3% with the measured value being 3/5x.7 $\sim$ 0.42%.

In spite of the higher background, the O_2 peak is still clearly visible with a S/N ratio of $\sim$10 and concentrations of 700 ppm should give a S/N of unity for these integration times.

Although the discrepancy between the predicted and measured O_2 in Xe levels at which the Raman O_2 intensity-to-base intensity will be unity is large when impurity scattering is not accounted for, this is not quite as serious as might be expected. The relevant number is the ratio of the Raman O_2 intensity to the base line fluctuations, not the base line intensity, and this will not change appreciably with trace impurity scattering as this scattering will tend to be averaged out to a smooth level by the multiplexing of several impurity molecular spectra through the AFPI. With the exception of O_2 in Xe, the agreement

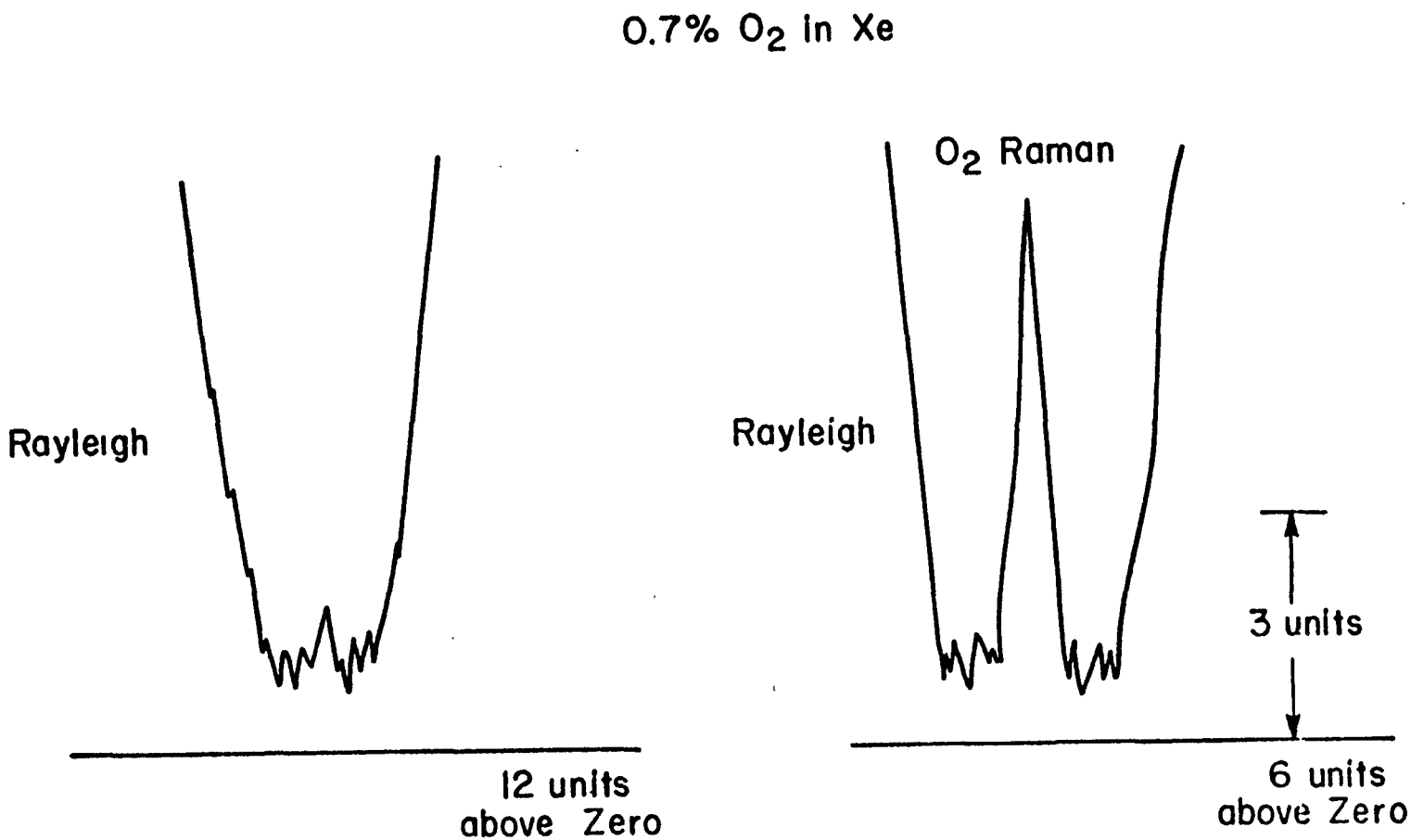

a. 1.4% O_2 in Xenon, no Rayleigh rejection.

b. 1.4% O_2 in Xenon, Rayleigh rejected.

Figure 5.11. O_2 calibration.

Table 5.3. SUMMARY OF THE REJECTION MEASUREMENTS

	Calculated	Measured
a) Surface figure limit of Rayleigh rejection ratio	~300-400	~290
b) Raman rejection ratio at 4B N_2 resonance with .25 cm^{-1} line incident	~140	~135-125
c) Multiplexing efficiency of the AFPI	—	0.84
d) Optimum NO resonance to maximize intensity	Rotational Raman cross sections not available	2B fsr, $\frac{I_{Ram}}{I_{Ray}} \sim 1/28$ 8B/3 fsr, $\frac{I_{Ram}}{I_{Ray}} \sim 1/6$
e) Concentration at which pollutant intensity equals base intensity	CO_2 in N_2 ~ 1.3% O_2 in N_2 ~ 1.5%	~1.6% ~1.3%
f) Concentration at which pollutant intensity equals base intensity	O_2 in X_e 0.02%	0.42% because of background contamination

between expected and measured rejection ratios and levels of detection is good, giving confidence to the projected levels when both the Raman and Rayleigh scattering can be rejected. Measured signal to noise ratios were on the order of 5-8 with an expected improvement of 5-6 when the laser width is narrowed from 0.25 cm^{-1} to 0.1 cm^{-1}, and assuming background sources to have concentrations on the order of the pollutant to be detected (with the obvious exception of O_2 and N_2), levels of detection of 350-400 ppm at signal to noise ratios of 8-16 for mixtures of CO_2 in N_2 and O_2 can be expected. The laboratory integration times using an f/3 collecting lens were on the order of 1-2 minutes across the Raman feature fo this signal-to-noise.

The work on the 4B and 8B resonances of CO_2 demonstrates that the correct setting for the FPI can be found to within 3-4 orders of the optimum position if the rotational constants of the molecule under study are known, with the generalized $B^{-1/2}$ rule for interferograms giving the expected width of the resonance. The use of the 8B/3 pattern for NO suggests that optimum resonances exist for maximizing the pollutant intensity and that these resonances may not be the naively expected 4B or 2B ones.

Although not appreciated during the course of the work, both Raman and Rayleigh scattering can be simultaneously removed with the use of a 2B pattern (for $\Delta J = \pm 2$ scattering) but the rejection ratios will decrease somewhat from those measured here, because of the decrease by a factor 2 of the fsr of the rejection Fabry-Perot interferometer.

References

1. H. Kildal and R.L. Byer, Proc. IEEE 59, 1944 (1971).

2. Private communication, W.H. Smith.

3. W.H. Smith, Opto-electronics 4, 161 (1972).

4. J. DelPlano, J.O.S.A. 59, 724 (1970).

SECTION 6

POLARIZATION REJECTION FILTER

The previous chapter noted the rejection of unwanted rotational Raman light possible with a Fabry-Peort interferometer used in the rejection mode. This method is limited by the requirements of high surface quality for the etalons and by backscattering due to poor anti-reflection coatings and alignment. These defects could be partially overcome in the filter operated in transmission using a low index of refraction material. The polarization rejection filter is discussed here as one possible solution.

6.1 Filter Theory

The relative orientations of the filter's optical components are illustrated in figure 6.1. The light to be filtered is polarized and allowed to fall on a crystal of birefringent material cut so as to fashion as a retardation plate having a phase angle shift of

$$\Phi = 2\pi k \ell n \tag{6.1}$$

k = the wavenumber of the incident light

ℓ = the thickness of the crystal

$n = n_{fast} - n_{slow}$ = the degree of birefringence

If the electric field after the first polarizer is of strength $\sqrt{2}$, then the field on the crystal axis will be

$$(E_{fast}, E_{slow}) = (1.1). \tag{6.2}$$

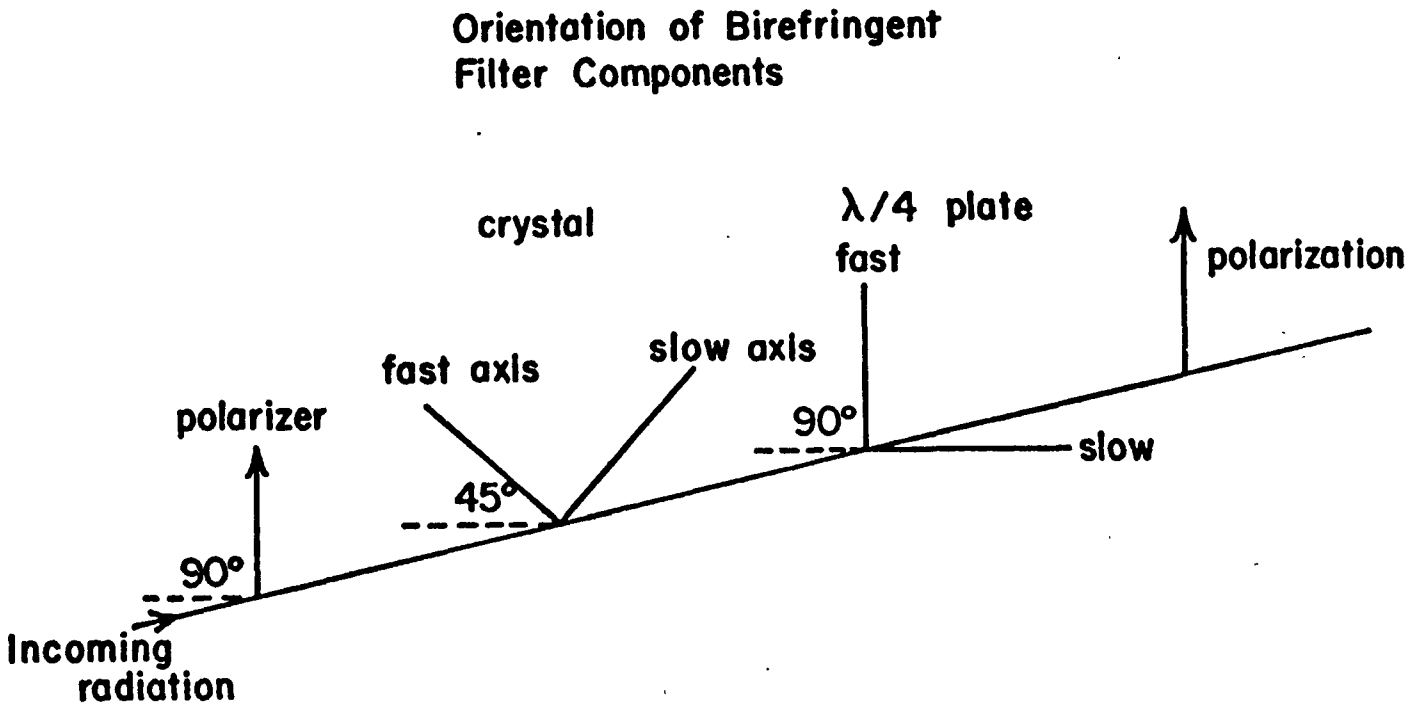

Figure 6.1. Elements of the polarization rejection filter.

After passing through the crystal, the fast axis will have a phase advanced by Φ over that of the slow, and the fields will be

$$(e^{i\Phi}, 1). \tag{6.3}$$

Now rotate the coordinate system to the $\lambda/4$ plate axis

$$1/\sqrt{2}\ (e^{i\Phi}+ 1, e^{i\Phi}-1) \tag{6.4}$$

and add a phase shift $\pi/2$ to the fast axis

$$\frac{1}{\sqrt{2}}\ (e^{i\Phi+\pi/2} + e^{i\pi/2}, e^{i\Phi}-1).$$

The difference in phase between the two components is now 0 or π for all Φ and the light is linearly polarized with its magnitude on the two axes of the polarizer being

$$1 \pm \cos\ \Phi\ .$$

Its angle to the x-axis of the polarizer is consequently

$$\tan^2\beta = \frac{1-\cos\ \Phi}{1+\cos\ \Phi} = \frac{\sin^2\Phi/2}{\cos^2\Phi/2}$$

$$\beta = \Phi/2$$

The $\lambda/4$ plate therefore changes a distribution of phase angle Φ into an angular distribution β with linear polarization.

Rotational Raman light has a spectrum of the form

$$K_J = K_0 \pm 4B(J+3/2) \mp 8D(J+3/2)^3 \tag{6.5}$$

k_0 = wavenumber of the exciting laser line

$B = B' - 3/2D$

B', D = the rotational constants of the molecule

and to first order, the birefringence n of the material can be assumed to have a linear dependence with k_j.

$$n_J = n_o + \alpha(J+3/2) \tag{6.6}$$

n_o = the birefringence at wavenumber k_o

For quartz,

$$n_o \sim 0.009$$
$$\alpha \sim 10^{-7} .$$

The phase shifts Φ_J for a Raman line passing through the filter will be

$$\Phi_J = 2\pi\ell\left[k_o \pm 4B(J+3/2) \mp 8D(J+3/2)^3\right]\left[n_o \pm \alpha(J+3/2)\right]$$

$$= 2\pi\ell\Big[k_o n_o \pm (J+3/2)(\underbrace{k_o\alpha}_{\sim .1}+\underbrace{4Bn_o}) + \underbrace{4B\alpha}_{\sim 8\times10^{-7}}(J+3/2)^2 \mp \underbrace{8Dn_o}_{\sim 6\times10^{-8}}(J+3/2)^3$$

$$- \underbrace{8D\alpha}_{\sim 6\times10^{-13}}(J+3/2)^4\Big]$$

where the estimates are for N_2 Raman into a quartz filter.

Neglecting for the moment the terms greater than linear in J gives

$$\Phi_J = 2\pi\ell\left[k_o n_o \pm (J+3/2)(k_o\alpha+4Bn_o)\right] \tag{6.7}$$

The phase will be independent of J to within multiples of 2π if

$$2\pi\ell\left[k_o\alpha + 4Bn_o\right] = 2\pi \tag{6.8}$$

$$\ell = \frac{1}{4Bn_o+\alpha k_o}$$

This is quite similar to formula 4.9 for the multiplexing of a periodic spectrum through a Fabry-Perot. The result then, is that all the Raman light will leave the $\lambda/4$ plate with the same angle β of linear polarization, where

$$\beta = \pi\ell n_o k_o + 3\pi/2 . \tag{6.9}$$

A polarizer placed after the $\lambda/4$ plate and having its axis properly oriented will attenuate this Raman light by its extinction factor, typically 10^4 or 10^5.

Other Raman light from different molecular species with different periodicities to their spectra will not experience such attenuation because, the phase angles that these generate will fall at random values from 0 to 2π, (assuming the periodicity of the light and that of the filter do not fall in the ration m/n where n and m are small integers).

The attenuation of this non-resonant species can be expected to be on the order 0.5 as the power factor for a polarizer goes as $\langle \sin^2 \rangle \sim 1/2$ pseudo-random Φ, and we thus have a filter capable of selectively attenuating a spectrum of given periodicity.

6.2 Fundamental Limitations

In practice the attenuation of the resonant spectrum is limited by finite line widths and by the neglected higher order terms in (J+3/2). The first effect is on the order of

$$1/3(\Delta\Phi)^2$$

where $\Delta\Phi$ is the 1/2 width of the phase shift caused by line width, but

$$\Delta\Phi = 2\pi \ell n \Delta k$$

and using

$$2\pi \ell n 4B \sim 2\pi$$

we find that

$$\Delta\Phi \sim \frac{2\pi}{4B} \Delta k \ . \qquad (6.10)$$

For N_2 with $B \sim 2$ and using a full width $2\Delta k \sim 0.2\ cm^{-1}$,

$$\frac{1}{3} (\Delta\Phi)^2 \sim 2.5 \times 10^{-3} \ .$$

That is, 2.5×10^{-3} of the light that should have been attenuated will pass the easy axis of the polarizer. This implies that the effective extinction is only 400 and since this assumed a uniform distribution of light over the phase shift $\Delta\Phi$, the extinction of the light in practice may be somewhat better, because of the concentration at small $\Delta\Phi$ in the core of the line.

The second effect may also be approximately found by the following argument.

Require that the phase error on the J^{th} line be no greater than its line half width (say 0.1 cm^{-1}). From the previous paragraph this should give an extinction of 400 or greater.

For the quadratic term

$$2\pi l a 4B(J+3/2)^2 \sim \frac{2\pi}{4B}\ (0.1)$$

find

$$J \sim 35$$

for the $(J+3/2)^3$ term

$$+2\pi l 6 D n_o (J+3/2)^3 \sim \frac{2\pi}{4B}\ (0.1)$$

find

$$J \sim 25$$

for the $(J+3/2)^4$ term

$$2\pi l 6 D a (J+3/2)^4 \sim \frac{2\pi}{4B}\ (0.1)$$

find

$$J \sim 200\ .$$

So for Raman lines with $J > 25$, one should expect extinctions on the order of 400 or better. For N_2, the Raman intensity for $J = 25$ is already down 1000 from the peak of the Boltzman distribution and consequently higher J values will not be troublesome.

This second effect was also estimated by direct calculation of the line positions and phases using known rotational constants. The results are given in tables 6.1 and 6.2 where the terminology filtered and unfiltered refers to individual line strengths before and after passage through the birefringent filter. The mathematical filter was tuned to attenuate N_2 and pass O_2 as a consequence.

N_2 total attenuation	562.6
O_2 total attenuation	2.03
S/N gain	277.

As was the case with the rejection Fabry-Perot filter, the system was tuned slightly off the expected resonance to compensate for the shift of the maximum of the Raman light due to temperature and distortion effects. The B value of N_2 is 1.9895 cm^{-1} while the system was set to attenuate the B value 1.9876 cm^{-1}. If the signal to noise to be achieved were to remain above 250, the B value could not deviate from optimum by more than$\sim$0.0005 cm^{-1}. This corresponds to a change in the crystal length of$\sim$60 microns, a tolerance that is easily achieved.

6.3 Comparision of FPI and Polarization Filters

In critical aspects, the birefringent filter and the Fabry-Perot interferometer scale as the ratio of the index of refraction of air to the birefringence of the quartz with a summary of the two methods presented in the table below. Other birefringent materials such as magnesium flouride, calcite, and ADP are possible, but will not be listed in the table as their properties will scale as the ratio of their birefringence to the birefringence of quartz.

Table 6.1 POLARIZATION REJECTION FILTER ATTENUATION OF N_2 RAMAN

	Stokes × 10^{-1} Intensity	Stokes Filtered × 10^{2} † Intensity
J = 0	0.6	0.6
	1.1	1.1
	1.6	1.6
	1.9	2.0
	2.2	2.3
	2.4	2.5
	2.4	2.6
	2.4	2.5
	2.3	2.3
	2.1	2.1
	1.9	1.9
	1.7	1.7
	1.4	1.6
	1.2	1.7
	1.0	1.8
	0.8	2.0
	0.6	2.3
	0.4	2.6
	0.3	2.8
	0.2	2.9
	0.1	2.9
	0.1	2.8
	0.0	2.6
	0.0	2.3
	0.0	2.0
	0.0	1.6

Increasing J Value

† anti-Stokes is similar

Table 6.2 POLARIZATION FILTER PASSING OXYGEN RAMAN

	Stokes × 10^{-1} Intensity	Stokes Filtered × 10^{-1} † Intensity
J = 0	0.6	0.6
	1.1	0.7
	1.6	0.0
	2.0	0.9
	2.3	2.3
	2.6	0.8
	2.7	0.1
	2.8	2.2
	2.8	2.3
	2.7	0.2
	2.6	0.8
	2.4	2.4
	2.2	1.1
	2.0	0.0
	1.7	1.1
	1.5	1.4
	1.3	0.2
	1.0	0.2
	0.9	0.8
	0.7	0.4
	0.5	0.0
	0.4	0.2
	0.3	0.3
	0.2	0.0
	0.1	0.0
	0.1	0.1
	0.1	0.0
	0.0	0.0
	0.0	0.0
	0.0	0.0

Increasing J Value

† anti-Stokes is similar

Table 6.3
COMPARISON OF FABRY-PEROT AND POLARIZATION REJECTION MECHANISMS

	Quartz	Fabry-Perot
length or plate separation*	12 cm	0.06 cm
birefringence or index of refraction*	.009	1.000
resonance width expressed as tolerance on length*	$\sim 60\mu$	$\sim 1\mu$
tolerance on collimation	error $\alpha\ \theta^2$	error $\alpha\ \theta^2$
tolerance on flatness of surfaces*	$\sim\lambda/10$	$\gtrsim\lambda/250$†
temperature stability required	$\sim 1°C$	$\sim 1°C$
parellelness of faces or etalons*	$\lambda/10$ across aperture	$\lambda/250$ across aperture†

* these quantities scale approximately as the ratio of the index of refraction and the birefringence.

† $\lambda/250$ is the technological limit.

The temperature dependence of the Fabry-Perot arises mainly from the expansion and contraction of the materials supporting the Fabry-Perot etalons as the temperature varies. The temperature sensitivity of the crystal filter however, comes about as a result both the expansion and contraction of the crystal as well as the dependence of the fast and slow indices of refraction on temperature. This temperature sensitivity of both filters can be utilized to tune the optimum resonance.

6.4 System Configurations

Two possible configurations for the device are shown below. The first case shows the rejection of both O_2 and N_2 using a linear arrangement of components. The second (if back-scattering can be minimized) an arrangement that uses a double pass of each crystal to reduce its required length by 1/2. In the case of figure 6.2b, the $\lambda/4$ plate has been eliminated by tuning the crystals using temperature. That is, the residual phase $\beta = \pi \ell n_o k_o + 3\pi/2$ has been tuned to 2π using the temperature dependence of n and ℓ. Since the maximum change required β is $\pm\pi$ or 1/2 an order while the resonance is ~ 5 orders wide, this adjustment is possible.

The conclusion then is that the birefringent filter should have filtering properties equal to or greater than those of the Fabry-Perot used in reflection because of the less severe restrictions on surface figure and parallelness and because of its use in the transmission mode. There is no gain in terms of ease of collimation or independence from temperature variations and as with the rejection Fabry-Perot, the optical path length can be doubled to provide simultaneous rejection of both the Raman and Rayleigh scattered radiation. The major difficulty will be to obtain a sample of quartz or magnesium flouride of sufficient optical quality that its characteristics do not change appreciably across the aperture to be used. This may be possible with some of the synthetic birefringent crystals that are now grown.

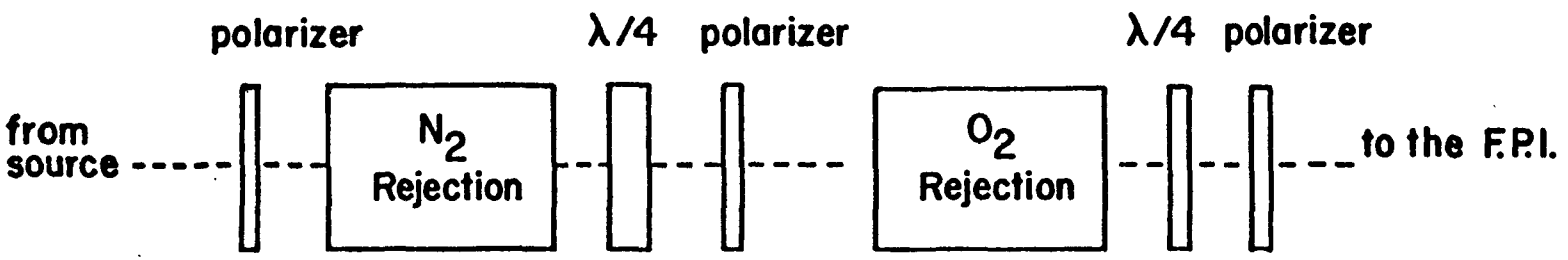

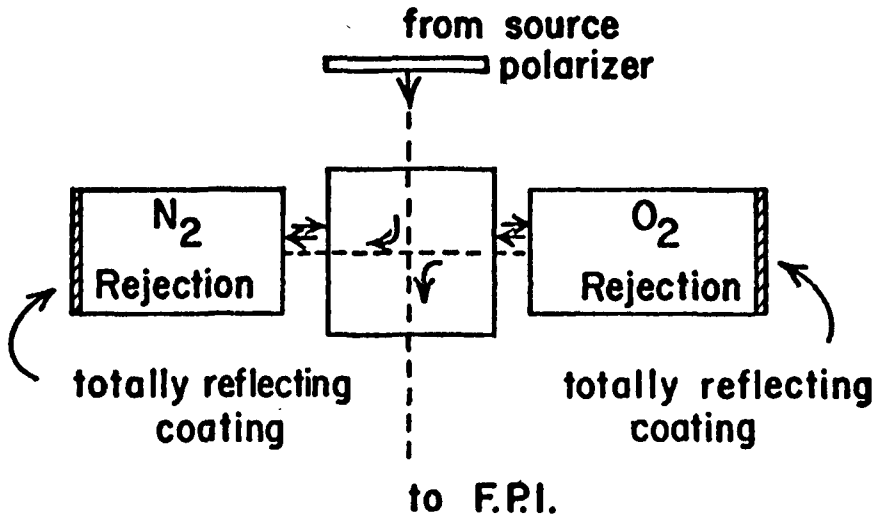

Figure 6.2. Configurations of the birefringent filter.

APPENDIX A

Basic Equations

A1. The Fabry-Perot Interferometer

Concepts derived from the Airy equation that are useful in describing the modes of operation of the Fabry-Perot interferometer are discussed briefly below.

The Free Spectral Range (fsr)

$$\text{fsr} = \frac{1}{2\mu t \cos\theta}$$

$$= \frac{1}{2t} \quad \text{for normal incidence and index of refraction of air assumed to be unity} \qquad \text{(A.1)}$$

gives the separation in wavenumbers between successive orders of the interferometer, and sets an upper limit to the bandwidth of the incident radiation that may be unambiguously resolved.

The Airy Finesse (f_A)

$$f_A = \frac{\text{fsr}}{\text{FWHM}} = \frac{\pi\sqrt{R}}{1-R} \qquad \text{(A.2)}$$

gives the number of full widths of a Fabry-Perot fringe within one fsr and is thus a measure of the resolution of the instrument. It is useful in being a function of the reflectivity alone.

The concept of finesse may be generalized to include other effects that limit the resolution, for just as f_A gives the maximum finesse for a given reflectivity of the etalons with all other defects negligible, so f_P the pinhole finesse sets a limit due to the finite size of the limiting aperture of the system, and f_d the defects finesse, a limit due to imperfect surface figure on the etalons. The practical finesse is therefore given approximately by

$$f = \left[f_A^{-2} + f_D^{-2} + f_P^{-2}\right]^{-1/2} \qquad (A.3)$$

with

$$f_D \sim n/2 \text{ or } n/3$$

where n is the n of λ/n for the specification of the surface figure and

$$f_P = \frac{fsr}{1/2\ k\alpha^2}$$

$k = 1/\lambda$

α = the half angle subtended by the pinhole.

The resolution of the Fabry-Perot interferometer is the FWHM of a fringe divided into the incident wavenumber.

$$\text{resolution} = \frac{k}{FWHM} = pf \qquad (A.4)$$

where $p = 2kt\mu$ is the order of the interferometer. A valid measure of resolution is more difficult to define when multiplexing a spectrum, because of ambiguities introduced by the transmission of the spectrum through several orders simultaneously.

The throughput (Q)

$$Q = \int J(\lambda) ds \; d\Omega \; d\lambda \qquad (A.5)$$

$J(\lambda)$ = incident energy/cm^2/sterrad/Å

has been calculated by Jaquinot[1] for a grating spectrometer and a Fabry-Perot interferometer where E is the aperture stop of the system, τ is the efficiency of the optical train, and β the solid angle of light accepted by the system. He found

$$Q_{grating} = \beta E\tau \sim 3.8$$

$$Q_{Fabry\text{-}Perot} = 2\pi E\tau \sim 235$$

where Hirschberg and Wilson[2] have supplied typical values for modern instruments. The Fabry-Perot interferometer is clearly superior to the grating spectrometer in th in this aspect.

The Contrast (C) of the interferometer is the ratio of the maximum to minimum intensity transmitted for a single wavelength. Neglecting absorption losses which only become important at high reflectivities, and the effects due to bulk and surface scattering yields

$$C = \left(\frac{1+R}{1-R}\right)^2 \qquad (A.6)$$

where R = the reflectivity of the etalons.

A2. Rotational Energy levels and Raman Intensities

(a) Nitric Oxide

The energy levels are E_j where

$$E_J = B_{J_{min}}(J+J_{min})(J+J_{min}+1) - D_{J_{min}}(J+J_{min})^2(J+J_{min}+1)^2 \quad (A.7)$$

and $B_{J_{min}}$ and $D_{J_{min}}$ are the rotational constants for NO and

$J_{min} = 1/2$ for the $\pi 1/2$ ground state

$J_{min} = 3/2$ for the $\pi 3/2$ ground state.

The $\pi 3/2$ state is 121.1 cm^{-1} above the $\pi 1/2$ state.

The Raman selection rules are $\Delta J = \pm 1, \pm 2, 0$ leading to displacements from the Rayleigh line of

$$|\Delta E_J| = 2B(J+J_{min}+1) - 4D(J+J_{min}+1)^3$$

for

$$|\Delta J| = 1$$

$$|\Delta E_J| = (4B-6D)(J+J_{min}+3/2) - 8D(J+J_{min}+3/2)^3 \quad (A.8)$$

for

$$|\Delta J| = 2 .$$

The relative intensities of these Raman lines are given by

$$I_{\Delta J = 1} = \frac{C\omega^4 2(J_{min})^2[(J+1)^2 - J_{min}^2]g_i e^{-E_i/kT}}{J(J+1)(J+2)(2J+1)} \quad (A.9)$$

where C = a constant.

$$I_{\Delta J = 2} = \frac{C\omega^4[(J+1)^2 - J_{min}^2][(J+2)^2 - J_{min}^2]g_i e^{-E_i/kT}}{(J+1)(J+2)(2J+1)(2J+3)} \qquad (A.10)$$

where g_i and E_i are the statistical weight and energy respectively, of the initial state of the transition. An additional factor $e^{-121.1\ cm^{-1}/kT}$ seperates the π 1/2 and π 3/2 states.

(b) Energy Levels and Raman Intensities for O_2, CO_2, N_2

The selection rules are now $\Delta J = 0, \pm 2$ with the energy levels, line displacements, and intensities given by the above formulae for NO with J_{min} set equal to zero.

Additionally, CO_2, and O_2 have the odd rotational levels absent, because of nuclear spin statistics, while N_2 has the odd and even levels falling in the ratio 1/2.

APPENDIX B

Component Specifications

1) Multilayer Dielectric Coatings (Karl Feuer, Burleigh Instruments)

a) R = 0.94 from 5500 Å to 4500 Å

b) R = 0.40 from 5500 Å to 4700 Å

c) R = 0.86 from 5500 Å to 4500 Å

2) Fabry-Perot Interferometer (Burleigh Instruments)

Model numbers RC50, RC40

High Voltage Power Supply number RC42

3) Filters (Millipore Corporation)

Lot #03225, type #AP 2501800 25 microns

4) Gas Samples (Matheson Gas)

Gas	Purity (minimum)
X_e	99.995%
O_2	99.6%
N_2	99.99%
NO	99.0%
CO_2	99.8%
CH_4	99.97% analyzed

5) Laser (Control Laser Corporation)

-2 watt Argon Ion

6) Photomultiplier Tube (Bailey Instruments: Centronic)

Model number 4249BA, blue sensitive with quantum efficiency of approximately 10-12% and dark current of 6 Hz uncooled.

7) Polarization Beam Splitter Cube (Perkin Elmer)

-2" aperture

-extinction ratio of 10^4 at wavelengths of 4880 Å and 5145 Å

-antireflection coated.

TECHNICAL REPORT DATA
(Please read Instructions on the reverse before completing)

1. REPORT NO.	2.	3. RECIPIENT'S ACCESSION NO.
EPA-600/2-77-154		

4. TITLE AND SUBTITLE	5. REPORT DATE
APPLICATION OF FABRY-PEROT INTERFEROMETRY TO REMOTE SENSING OF GASEOUS POLLUTANTS	August 1977
	6. PERFORMING ORGANIZATION CODE
7. AUTHOR(S)	8. PERFORMING ORGANIZATION REPORT NO.
W. Hayden Smith and Robert A. King	
9. PERFORMING ORGANIZATION NAME AND ADDRESS	10. PROGRAM ELEMENT NO.
Princeton University Observatory Princeton University Princeton, NJ 08540	1AD712
	11. CONTRACT/GRANT NO.
	Contract No. 68-02-0327 Grant No. 800805
12. SPONSORING AGENCY NAME AND ADDRESS	13. TYPE OF REPORT AND PERIOD COVERED
Environmental Sciences Research Laboratory - RTP, NC Office of Research and Development U.S. Environmental Protection Agency Research Triangle Park, NC 27711	Final 8/71 - 3/75
	14. SPONSORING AGENCY CODE
	EPA/600/09
15. SUPPLEMENTARY NOTES	

16. ABSTRACT

A method for the remote sensing of molecular species via the rotational Raman effect was developed. The method uses the properties of a scanning Fabry-Perot interferometer to multiplex the spectra in a manner specific for a given species. Furthermore, the method allows the "in principle" sensitivity of remote pollutants to be increased by as much as 10^4 over the vibrational Raman effect. To achieve this goal, a scheme was developed for the rejection of the Raman spectra of the abundant background gases, N_2 and O_2. This was accomplished efficiently and with little loss of the Raman scattered light from the pollutant species. Laboratory measurements were conducted to demonstrate the method for a few specific cases; results were encouraging. In addition to the light rejection scheme actually used, a radically new technique utilizing the polarization properties of the Raman scattered light was also developed.

17. KEY WORDS AND DOCUMENT ANALYSIS

a. DESCRIPTORS	b. IDENTIFIERS/OPEN ENDED TERMS	c. COSATI Field/Group
* Air Pollution	Fabry-Perot interferometers	13B
Flue gases		21B
* Remote sensing		14B
* Optical scanners		17I
* Interferometers		20F
Raman spectra		

18. DISTRIBUTION STATEMENT	19. SECURITY CLASS *(This Report)*	21. NO. OF PAGES
RELEASE TO PUBLIC	UNCLASSIFIED	142
	20. SECURITY CLASS *(This page)*	22. PRICE
	UNCLASSIFIED	

EPA Form 2220-1 (9-73)